MTM

MACHINES
TECHNOLOGIES
MATERIALS

EDITORIAL BOARD

The current issue and the first issue of MTM journal and the conditions for publication can be find on www.mech-ing.com/journal

C O N T E N T S

A MULTINOMIAL APPROACH TO THE MACHINE INTERFERENCE PROBLEM

Prof. Gurevich G., Prof. Hadad Y., Dr. Keren B.

Department of Industrial Engineering and Management – SCE-Shamoon College of Engineering, Beer Sheva, Israel

gregoryg@sce.ac.il, yossi@sce.ac.il, baruchke@sce.ac.il

Abstract: This paper presents a multinomial model for a special case of the machine interference problem (MIP), where each of N identical machines randomly requests several different service types. The model allows the calculation of the expected interference time in the queue for each service type. The extended version of the model allows calculation of the exact distribution function of the steady state waiting time and total service time for each type of requested service. In addition, the model can be adjusted for the case where the service is provided by a group of K identical operators, each operator is capable to handle all types of service, but each service type has a different priority.

Keywords: MULTINOMIAL MODEL, QUEUING, MACHINE INTERFERENCE PROBLEM, MULTIPLE SERVICE TYPES, PRIORITY.

1. Introduction

The presented multinomial approach to the machine interference problem was recently developed by Hadad et al. [1], Gurevich et al. [2]-[3] and Keren et al. [4]. The proposed models are applicable for a production system with N identical machines that produce the same product in parallel and independently of each other. Each of N identical machines randomly requests several different service types. Each request for a service type is fulfilled by an operator who can provide only one service type. Firstly, we shortly outline the basic model proposed by Hadad et al. [1] that allows the calculation of the expected interference time in the queue for each service type. The advantages of this model are that it is much easier to apply compared to the Markovian models and it does not need any restrictive assumptions about failure rate and service distribution, as those of the Markovian models. Afterward, we present the extended version of the model that allows calculation of the exact distribution function of the steady state waiting time and total service time (waiting time + service time) for each type of requested service. These distributions functions are useful for the case in which there is a time limit for one service (or more), such that it must be accomplished within a certain time from the moment of the request. A delay in the service above a given time spoils the product and makes it useless for its intended purpose. Finally, we adjust the basic model for the case where the service is provided by a group of K identical operators, each operator is capable to handle all types of service, but each service type has a different priority. The presented models enable practitioners to determine the optimal number of operators in order to minimize the cost per unit of product or maximize the total profit, or to set other performance measures.

2. The basic model

The model is suitable for MIP with multiple service type requests. Each request can be handled by a qualified operator that assigned to only one service type. At least one operator is assigned for each service type, but the number of operators may not exceed the number of machines, *N*.

2.1. The model assumptions

The following list sets forth the assumptions used in creating the model:

1)   There are *N* identical machines.

2)   Each machine can be in one of the following positions, where the probabilities for each position are constant in a steady state situation and identical for all machines:

   a.   running (producing items),

   b.   having a type j service, $j = 1, ..., J$,

   c.   waiting for type j service (interference).

3)   Machine failures are independent.

4)   Service time is random.

5)   Each service request transfers immediately to the operators assigned to handle that specific service request type.

6)   An available operator handles a service request immediately.

7)   Each service request is handled by only one operator.

8)   Walking time from one machine to another is negligible.

9)   A machine is idle while waiting for a service or while getting a service.

2.2. Notations

This section presents the notations that are used for the model definition.

T - Runtime. The length of time needed for a machine to process one unit of a product.

t_j - Average time of a type j service, $j = 1, ..., J$. The average length of time that a type j operator invests in one unit of a product during a cycle time.

H_1 - Cycle time. The length of time needed for one machine and one operator for each service type to produce one unit of the product. This cycle time is calculated as follows:

$$H_1 = T + \sum_{j=1}^{J} t_j \; . \tag{1}$$

The parameters T, t_j and H_1 are not dependent upon the number of machines (N).

N - Number of machines. The number of identical machines in the production line.

H_N - Adjusted cycle time. The expected length of time needed for a production line with N identical machines that are operated by a given number of operators for each service type to

produce N units of the product. (During H_N each machine produces an average of one unit.)

t_{I_j} - Interference time. The average time during a production cycle (H_N) during which a machine is idle because it is waiting for a type j operator, $j = 1,...,J$.

i_j - Interference rate. The ratio between the interference time t_{I_j} and the adjusted cycle time H_N, that is, $i_j = {t_{I_j}}/{H_N}$.

S_j - Service rate. The ratio between the average time of a type j service t_j and the adjusted cycle time H_N, that is, $S_j = {t_j}/{H_N}$.

K_j - Number of operators assigned to type j service, $1 \le K_j \le N$.

The adjusted cycle time H_N is calculated as follows:

$$H_N = T + \sum_{j=1}^{J} t_j + \sum_{j=1}^{J} t_{I_j} \qquad (2)$$

$$= H_1 + \sum_{j=1}^{J} t_{I_j} = H_1 + \sum_{j=1}^{J} i_j \times H_N$$

$$= \frac{H_1}{\left(1 - \sum_{j=1}^{J} i_j\right)}.$$

p_0 - Probability that a machine is running. This probability is calculated as follows:

$$p_0 = \frac{T}{H_N} = \frac{T\left(1 - \sum_{j=1}^{J} i_j\right)}{H_1}.$$

p_j - Probability that a machine is getting or requiring a type j service, $j = 1,...,J$. This probability is calculated as follows: $p_j = S_j + i_j, \; j = 1,...,J$.

Each machine can be in one of two states-running or idle. The idle state has J sub-states for each service type request. A machine in sub-state j can be in one of two positions-getting a service j or waiting for this service. Because all these states are mutually exclusive, it is clear that $p_0 + \sum_{j=1}^{J} p_j = 1$.

X_0 - Number of running machines (a random variable).

X_j - Number of machines that are getting or requiring a type j service (a random variable), $j = 1,...,J$. It is clear that $X_0 + \sum_{j=1}^{J} X_j = N$, where the number of running machines and the number of idle machines is equal to the number of machines in production line N.

A group with N machines and J types of service has $\binom{N+J}{J}$ states. A state is a vector $\left(X_0 = x_0, X_1 = x_1,..., X_J = x_J\right)$, where X_0 is the number of running machines and X_j, $j = 1,2,...,J$, is the number of idle machines that are getting or requiring a type j service. The probability of each state can be calculated using the multinomial distribution as shown in equation (3):

$$P\left(X_0 = x_0, X_1 = x_1,..., X_J = x_J\right)$$

$$= \begin{cases} \dfrac{N!}{\prod\limits_{j=0}^{J} x_j!} \prod\limits_{j=0}^{J} \left(p_j\right)^{x_j} & \text{where } \sum\limits_{j=0}^{J} x_j = N \\ 0 & \text{otherwise} \end{cases} \qquad (3)$$

2.3. An interference calculation

This section presents the interference rate calculation derived directly from the multinomial distribution properties.

Step 1- Perform time study/work measurement to measure and to determine the running time T and the time for each service type $t_j \; (j = 1,2,...,J)$. Use the measured data and equation (1) to calculate H_1.

Step 2 – Calculate $E\left(L_j\right)$, the expected number of machines waiting for type j service, $j = 1,...,J$. According to the model assumptions, the number of machines requiring a type j service has a binomial distribution with expected value computed by:

$$E(X_j) = \sum_{m=0}^{N} P\left(X_j = m\right) \times m = N \times p_j.$$

Then, $E\left(L_j\right)$ has the form

$$E\left(L_j\right) = \sum_{m=K_j+1}^{N} P\left(X_j = m\right) \times \left(m - K_j\right) \qquad (4)$$

$$= N \times p_j - K_j$$

$$+ \sum_{m=0}^{K_j} \binom{N}{m} \left(p_j\right)^m \left(1 - p_j\right)^{N-m} \times \left(K_j - m\right).$$

(see [1]).

Step 3 – Calculate i_j, the interference rate, as follows:

$$i_j = \frac{E(L_j)}{N}.$$

Since $p_j = i_j + S_j = i_j + t_j\left(1 - \sum_{j=1}^{J} i_j\right) / H_1$, by (4), the previous equation has the following form:

$$i_j = \left(i_j + \frac{t_j}{H_1}\left(1 - \sum_{j=1}^{J} i_j\right)\right) - \frac{K_j}{N}$$

$$+ \frac{\sum_{m=0}^{K_j} \binom{N}{m}\left(\left(i_j + \frac{t_j}{H_1}\left(1 - \sum_{j=1}^{J} i_j\right)\right)\right)^m}{}$$

$$\frac{\times \left(1 - \left(i_j + \frac{t_j}{H_1}\left(1 - \sum_{j=1}^{J} i_j\right)\right)\right)^{N-m} \times (K_j - m)}{N}. \quad (5)$$

Equation (5) produces a system of J equations, one for each service type. The solution of these J equations is the interference rate. This system of J equations has a uniquely feasible solution as derived from the multinomial distribution properties (see [1]). The solution can be obtained by "trial and error" or by software tools such as Excel-Solver.

3 Distribution of the steady state waiting time and total service time

This section considers a production line with N identical machines, as was presented in Section 2. An additional assumption here is that the service time of a specific service type j has an exponential distribution with the parameter λ_j. For all service types other than j, the additional assumption related to the exact service time distribution is not needed. The section presents exact CDFs for the steady state waiting time and total service time for service type j, $j = 1,...,J$, in the context of FCFS queue discipline.

The first step in deriving these distributions is evaluation of the inputs of the model described in section 2 (the machine runtime and the average time of each service type) by work study (Hadad et al. [5]). The second step is to use the model described in section 2 to calculate the probability that a machine is getting or requiring a type j service, p_j. Let us define the following random variables:

W_j - the steady state waiting time of a machine for a type j service, $j = 1,...,J$, (the waiting time from the moment of the request for this service until the moment the requested service is commenced.)

TS_j - the steady state total service time (waiting time + service time) of a machine for a type j service, $j = 1,...,J$, from the moment of the request for this service until completion of the requested service.

The following Proposition 1 provides the CDF of the steady state waiting time W_j and total service time TS_j of a machine

for service type j, $j = 1,...,J$, in the context of the FCFS queue discipline.

Proposition 1. Given that the queue discipline is FCFS, for any value of time $y > 0$, the probability that the steady state waiting time W_j is longer than y is:

$$P(W_j > y)$$
$$= \sum_{r=1}^{N-K_j} \left(\binom{N}{r+K_j} \times (p_j)^{r+K_j} \times (1-p_j)^{N-r-K_j} \times \left(\sum_{n=0}^{r-1} e^{-\lambda_j \times K_j \times y} \times \frac{(\lambda_j \times K_j \times y)^n}{n!} \right) \right). \quad (6)$$

The probability that the steady state total service time TS_j is longer than y is:

$$P(TS_j > y) = e^{-\lambda_j \times y} \times \left(\sum_{m=0}^{K_j} \binom{N}{m} \times (p_j)^m \times (1-p_j)^{N-m} \right)$$

$$+ \sum_{r=1}^{N-K_j} \left(\binom{N}{r+K_j} \times (p_j)^{r+K_j} \times (1-p_j)^{N-r-K_j} \times \left(\int_0^y \left(\sum_{n=0}^{r-1} e^{-\lambda_j \times K_j \times (y-x)} \times \frac{(\lambda_j \times K_j \times (y-x))^n}{n!} \right) \times \lambda_j e^{-\lambda_j \times x} dx \right) + e^{-\lambda_j \times y} \right). \quad (7)$$

Note that the integral in Equation (7) can be easily calculated numerically.

4. Different priorities of service types

This Section presents an adjusted model for the case where the service is provided by a group of K identical operators, each operator is capable to handle all types of service, but each service type has a different priority. The service types are ranked according to their priorities. The operators serve the machines (handling the requests) according to these priorities. For example, if two machines are waiting for different service types and only one operator is available, the operator will serve the machine that requests the service type with the higher priority. The machines are served according to the absolute priority policy (a preemptive priority). When all the operators are busy and an additional machine requests a service with a higher priority than one of the machines currently being served, the lowest priority service type that is provided ceases immediately and the operator serves the machine with the higher priority service type. When a ceased service is resumed, this service is accomplished from the point where it was preempted without loss of the prior work. If there are several machines with the same priority, and there are not enough operators available to service all of them, machines are randomly selected to be served. The probability of each state of the production system $(X_0 = x_0, X_1 = x_1,..., X_J = x_J)$ can be calculated using the multinomial distribution as shown in equation (3). According to the model assumptions, the expected number of machines that are getting or requiring a type 1 service (with the highest priority) has a binomial distribution with an expected value computed by:

$$E(X_1) = \sum_{m=0}^{N} P(X_1 = m) \times m = N \times p_1.$$

Hence, for $K = 1,...,N-1$, $E(L_1)$ (the expected number of

machines that are waiting for a type 1 service) is calculated as:

$$E(L_1) = \sum_{m=K+1}^{N} P(X_1 = m) \times (m - K)$$ (8)

$$= \sum_{m=K+1}^{N} \binom{N}{m} (p_1)^m (1-p_1)^{N-m} \times (m-K) .$$

It is obvious that for $K = N$, $E(L_1) = 0$. The ratio between the expected number of machines that are waiting for a type 1 service and the total number of the machine is the interference rate for type 1 service, $i_1 = E(L_1) / N$ (see [6]).

Under the model assumptions, the machines are served according to the absolute priority policy. Therefore, the number of machines waiting for the type 1 service does not depend on the number of machines requiring or getting service types with lower priority. The number of machines that are waiting for type j, $2 \leq j \leq J$, service depends on the number of machines requiring or getting service types with higher priority. The expected number of machines that are waiting for type j service is calculated as follows for any $2 \leq j \leq J$:

$$E(L_j) = \sum_{n=0}^{N} E\left(L_j \,\middle|\, \sum_{i=1}^{j-1} X_i = n \right) \times P\left(\sum_{i=1}^{j-1} X_i = n \right),$$ (9)

where

$$P\left(\sum_{i=1}^{j-1} X_i = n \right) = \binom{N}{n} \left(\sum_{i=1}^{j-1} p_i \right)^n \left(1 - \sum_{i=1}^{j-1} p_i \right)^{N-n}$$ (10)

$n = 0, 1, ..., N,$

because according to the model assumptions $\sum_{i=1}^{j-1} X_i \sim Bin\left(N, \sum_{i=1}^{j-1} p_i \right)$. Thus, straightforwardly we have for any $1 \leq K \leq N-1, 2 \leq j \leq J$, the expected number of machines that are waiting for type j service is presented by the following equation:

$E(L_j)$

$$= \sum_{n=0}^{N} \left(\left(\sum_{m=max(0,K-n+1)}^{N-n} \left(\binom{N-n}{m} \left(\frac{p_j}{1-\sum_{i=1}^{j-1} p_i} \right)^m \left(1 - \frac{p_j}{1-\sum_{i=1}^{j-1} p_i} \right)^{N-n-m} \right) \right. \right.$$
$$\left. \left. \times (m - max(0, K-n)) \right) \right)$$
$$\times \binom{N}{n} \left(\sum_{i=1}^{j-1} p_i \right)^n \left(1 - \sum_{i=1}^{j-1} p_i \right)^{N-n} .$$ (11)

The interference rates i_j are calculated as follows:

$$i_j = \frac{E(L_j)}{N}, \quad j = 1, ..., J.$$ (12)

By substitution of $p_j = i_j + S_j = i_j + t_j \left(1 - \sum_{j=1}^{J} i_j \right) / H_1$, and by calculating $E(L_j)$ as defined by equation (8) and equation (11), equation (12) produces a system of J equations, one for each service type. This system of J equations has a unique feasible solution (see [4]). The solution of these J equations is the interference rate. The solution can be obtained by "trial and error" or by software tools such as Excel-Solver.

5. Conclusions

This paper outlines the multinomial approach to a special case of the machine interference problem where each of N identical machines randomly requests several different service types. The presented models derived by this approach allow the calculation of the expected interference time in the queue for each service type and the exact distribution function of the steady state waiting time and total service time for each type of requested service. The interference times enable practitioners to calculate the adjusted cycle time, the expected number of machines that are waiting for each service type, the workload, the utilization of the machines, and the outputs for any given number of operators and priority.

6. References

1. Hadad Y., Keren, B. and Gurevich, G. (2013). A multinomial model for the machine interference problem with different service types and multiple operators. *Computers & Industrial Engineering*, 66(2), pp: 264-273.

2. Gurevich, G., Hadad, Y. and Keren, B. (2015a). Calculation of the steady state waiting time distribution in the context of the machine interference problem. *International Journal of Operational Research*, in press.

3. Gurevich, G., Keren, B. & Hadad, Y. (2015b). The economic number of operators for the machine interference problem with heterogeneous machines and preemptive priority. *International Journal of Logistics Systems and Management*, in press.

4. Keren, B., Gurevich, G. and Hadad, Y. (2015). Machines interference problem with several operators and several service types that have different priority. *International Journal of Operational Research*, in press.

5. Hadad, Y., Keren, B. and Hanani, Z.M. (2014). The number of measurements to be performed for time study analysis. *European Journal of Industrial Engineering*, 8(2): 222-243.

6. Jones, D.W. (1971) Work measurement of multi machine assignments, 3.92-3.112 of Maynard HB., *Industrial Engineering Handbook*, McGraw-Hill: New-York.

Three-dimensional S-N curve method to estimate fatigue life of EN AW 6063.T66 aluminium alloy during combined loading under in-and-out of phase shift 0° and 90° and comparing with fatigue criteria

Ing. Uhríčik M., PhD.[1]; Ing. Kopas P., PhD.[1]; Prof. Ing. Palček P., PhD.[1]; Ing. Hurtalová L., PhD.[1]

[1]Faculty of Mechanical Engineering, University of Žilina, Slovak Republic
E-mail: milan.uhricik@fstroj.uniza.sk, peter.kopas@fstroj.uniza.sk, peter.palcek@fstroj.uniza.sk, lenka.hurtalova@fstroj.uniza.sk

Abstract: The article deals with determining of fatigue lifetime of structural materials during by multiaxial cyclic loading. The theoretical part deals with the fatigue and with criteria for evaluation of multiaxial fatigue lifetime, especially Fatemi-Socie, Smith-Watson-Topper, Brown-Miller and Liu. The experimental part deals with testing of specimens for identification of the strain-life behaviour of material and determining the number of cycles to fracture of aluminium alloy for phase shift 0° and 90°. Extensive fatigue experiments were conducted using 6063.T66 aluminium alloy under multiaxial bending-torsion loading.

KEYWORDS: ALUMINIUM ALLOY, MULTIAXIAL FATIGUE, FATIGUE LIFETIME, CRITERIA, CYCLIC LOADING

1. Introduction

Aluminium is the world's most abundant metal and is the third most common element, comprising 8% of the earth's crust. The versatility of aluminium makes it the most widely used metal after steel. Pure aluminium is soft, ductile, corrosion resistant and has a high electrical conductivity. It is widely used for foil and conductor cables, but alloying with other elements is necessary to provide the higher strengths needed for other applications. Aluminium is one of the lightest engineering metals, having strength to weight ratio superior to steel. By utilising various combinations of its advantageous properties such as strength, lightness, corrosion resistance, recyclability and formability, aluminium is being employed in an ever-increasing number of applications. This array of products ranges from structural materials through to thin packaging foils [1, 2, 3].

Fatigue failures in metallic structures are a well-known technical problem. In a specimen subjected to a cyclic load, a fatigue crack nucleus can be initiated on a microscopically small scale, followed by crack grows to a macroscopic size, and finally to specimen failure in the last cycle of the fatigue life. Understanding of the fatigue mechanism is essential for considering various technical conditions which affect fatigue life and fatigue crack growth, such as the material surface quality, residual stress, and environmental influence. This knowledge is essential for the analysis of fatigue properties of an engineering structure [4, 5].

Fatigue under combined loading is a complex problem. A rational approach might be considered again for fatigue crack nucleation at the material surface. The state of stress at the surface is two-dimensional because the third principal stress perpendicular to the material surface is zero [6]. Another relatively simple combination of different loads is offered by an axle loaded under combined bending and torsion. This loading combination was tested in our and also in many others experiments [7, 8]. In spite of this fact, fatigue mechanisms are still not fully understood. This is partly due to the complex geometrical shapes and also complex loadings of engineering components and structures which result in multiaxial cyclic stress-strain states rather than uniaxial.

2. Fatigue criteria

There are plenty of hypotheses used for evaluating a degree of damage caused by variable load [9, 10]. Life prediction methods which presume homogeneous material (free from cracks, inclusions or defects) at the outset of the investigation can be divided into strain-based (low-cycle fatigue) and stress-based (high-cycle fatigue) methods. Low-cycle fatigue is characterized by repeated plastic strains during cyclic loading conditions where fatigue failure occurs after relative low number of load cycles (in the order of 10^4 cycles). This design approach is normally used in fatigue assessment of local areas where high stress concentrations exist and the material response locally is repeated plastic deformation. In addition, stress-based approaches use the elastic stress range (or amplitude) as the governing load parameter. There were chosen four fatigue criteria: Fatemi-Socie, SWT, Brown-Miller and Liu fatigue criterion.

Fatemi and Socie [11] observed that the Brown and Miller's idea could be successfully employed even by using the maximum stress normal to the critical plane, because the growth rate mainly depends on the stress component normal to the fatigue crack. Starting from this assumption, he proposed two different formulations according to the crack growth mechanism: when the crack propagation is mainly MODE I dominated, then the critical plane is the one that experiences the maximum normal stress amplitude and the fatigue lifetime can be calculated by means of the uniaxial Manson-Coffin curve; on the other hand, when the growth is mainly MODE II governed, the critical plane is that of maximum shear stress amplitude and the fatigue life can be estimated by using the torsion Manson-Coffin curve [9]. Criterion has the following form:

$$\frac{\Delta\gamma}{2} \times \left(1 + k \times \frac{\sigma_{n,max}}{\sigma_y}\right) = \frac{\tau_f'}{G} \times (2 \times N_f)^{b_\gamma} + \gamma_f' \times (2 \times N_f)^{c_\gamma} \qquad (1)$$

Smith, Watson and Topper (SWT) created a parameter for multiaxial load, which is based on the main deformation range $\Delta\varepsilon_1$ and maximum stress $\sigma_{n,max}$ to the main plane. Criterion has the following form:

$$\sigma_{n,max} \times \frac{\Delta\varepsilon_1}{2} = \frac{\sigma_f'^2}{E} \times (2 \times N_f)^{2b} + \sigma_f' \times \varepsilon_f' \times (2 \times N_f)^{b+c} \qquad (2)$$

Brown and Miller [12] observed that the fatigue life prediction could be performed by considering the strain components normal and tangential to the crack initiation plane. Moreover, the multiaxial fatigue damage depends on the crack growth direction. Different criteria are required if the crack grows on the component surface or inside the material. In the first case they proposed a relationship based on a combined use of a critical plane approach and a modified Manson-Coffin equation, where the critical plane is the one of maximum shear strain amplitude. Criterion, which was created, has the following form:

$$\frac{\Delta\gamma_{max}}{2} + S \times \Delta\varepsilon_n = A \times \frac{\sigma_f - 2 \times \sigma_{n,mean}}{E} \times (2 \times N_f)^b + B \times \varepsilon_f^{'} \times (2 \times N_f)^c \quad (3)$$

Liu created a virtual model of the deformation energy, which is a generalization of the axial energy on the basis of prediction of fatigue life. Criterion has the following form:

$$\Delta W = 4 \times \sigma_f^{'} \times \varepsilon_f^{'} \times (2 \times N_f)^{b+c} + \frac{4 \times \sigma_f^{'2}}{E} \times (2 \times N_f)^{2b} \quad (4)$$

Where: $\gamma_f^{'}$ is the fatigue ductility coefficient in torsion; $\varepsilon_f^{'}$ is the fatigue ductility coefficient; $\sigma_f^{'}$ is the fatigue strength coefficient; $\sigma_{n,max}$ is the maximum stress; $\sigma_{n,mean}$ is the mean stress; σ_y is the stress in the direction of the axis y; $\tau_f^{'}$ is the fatigue strength coefficient in torsion; $\Delta\gamma_{max}$ is the maximum shear strain range; $\Delta\varepsilon_n$ is the normal strain range; ΔW is the virtual strain energy; b is the fatigue strength exponent; b_γ is the fatigue strength exponent in torsion; c is the fatigue ductility exponent; c_γ is the fatigue ductility exponent in torsion; N_f is the number of cycles to fracture; A, B, S, k, α are material parameters; E is the elasticity modulus in tension; G is the elasticity modulus in torsion.

3. Test material

The research was conducted on an AlMgSi07.F25 aluminium alloy: the EN AW 6063.T66 aluminium alloy. The EN AW 6063.T66 is a medium strength alloy, suitable for applications where no special strength properties are required. The T66 treatment corresponds to solution heat-treated and then artificially aged (precipitation hardened) to a higher level of mechanical properties through special control of a manufacturing process. The material used in this research was delivered in the form of a cylindrical shape with a diameter 10 mm. The length of cylindrical bars was 150 mm. The material was in a rolled state. The shape of test bar is shown in Fig.1. This test bar had a defined section, in which was expected an increased concentration of stress and creation a fatigue fracture.

Fig.1 The shape of a test bar

4. Experimental strain-life data results

One hundred and ninety-five smooth specimens for phase shift 0° and one hundred and ninety-five smooth specimens for phase shift 90°, were tested under strain controlled conditions in order to identify the strain-life behaviour of the experimental material. After machining, the specimen surfaces were mechanically polished. The experiments were carried out in an electro mechanic fatigue test machine developed on University of Žilina (Fig.2 and Fig. 3).
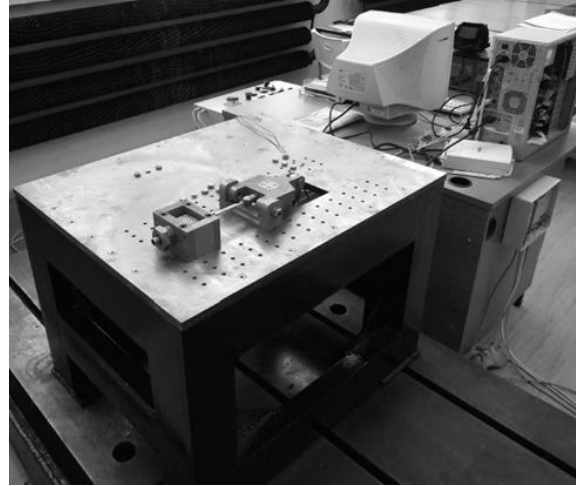
Fig.2 Electro mechanic fatigue test machine
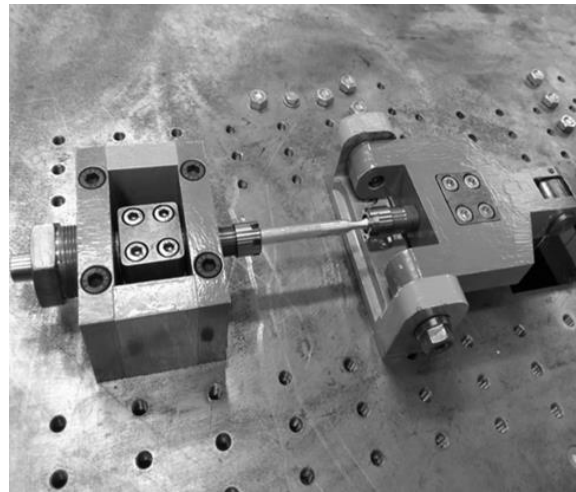
Fig.3 A gripping attachment of test machine

For evaluation of fatigue curves it needs to know stress and strain conditions on individual loading levels. A sinusoidal waveform was used as command signal. The fatigue tests were conducted with constant strain amplitudes, at room temperature, in air. The specimens were cyclic loaded under strain control with symmetrical proportional bending- torsion loading, with a nominal strain ratio, $R_\varepsilon = -1$.

The computational fatigue tests were performed under in-phase cyclic loading with the zero mean value. All tests were performed under controlled bending and torsion moments. Frequency of each analysis was equal to 30 Hz.

This research was conducted on an EN AW 6063.T66 aluminium alloy. This material is a medium strength alloy, suitable for applications where no special strength properties are required.

From experimentally measured values of number of cycles to failure was created three-dimensional fatigue curve $\varepsilon_{xx} - \gamma_{xy} - N_f$ for phase shift 0°, which is shown in Fig. 4.
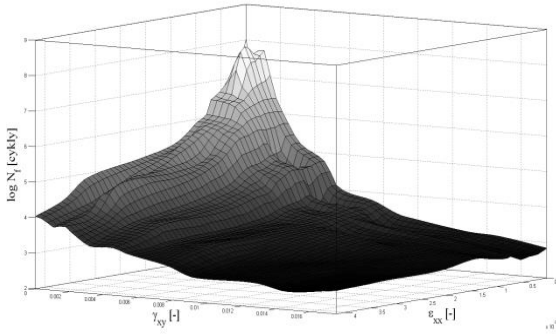
Fig.4 *Three-dimensional fatigue curve ε_{xx} - γ_{xy} - N_f for multiaxial fatigue with phase shift 0°*

For another analysis was used a Fatigue Calculator software [13]. This program can quickly calculate fatigue lifetime of selected material. In our calculation we considered with four multiaxial criteria described above.

From those calculated values of number of cycles to failure were created three-dimensional fatigue curves for phase shift 0°. In Fig. 5 is shown a three- dimensional fatigue curve for Fatemi-Socie criterion, in Fig. 6 is for SWT criterion, in Fig. 7 is for Brown-Miller criterion and in Fig. 8 is for Liu criterion.
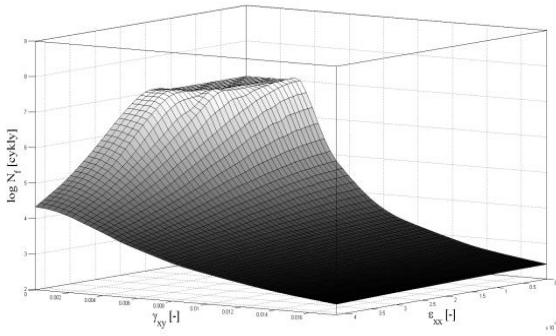
Fig.5 *Three-dimensional fatigue curve ε_{xx} - γ_{xy} - N_f for multiaxial Fatemi-Socie criterion with phase shift 0°*
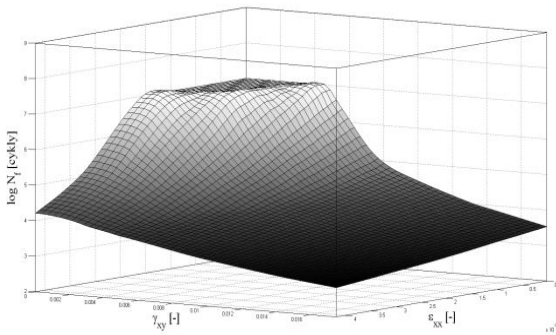
Fig.6 *Three-dimensional fatigue curve ε_{xx} - γ_{xy} - N_f for multiaxial SWT criterion with phase shift 0°*
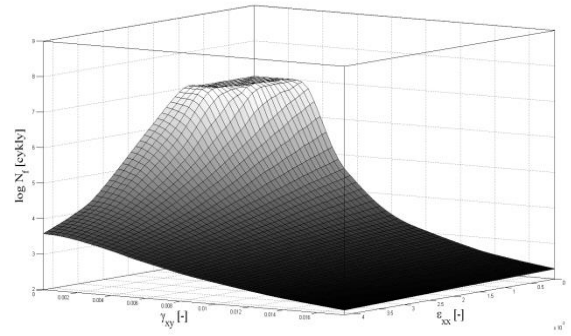
Fig.7 *Three-dimensional fatigue curve ε_{xx} - γ_{xy} - N_f for multiaxial Brown-Miller criterion with phase shift 0°*
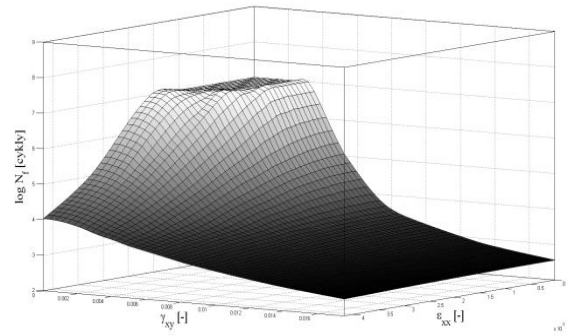
Fig.8 *Three-dimensional fatigue curve ε_{xx} - γ_{xy} - N_f for multiaxial Liu criterion with phase shift 0°*

From the experimentally measured fatigue values there was created three-dimensional fatigue curve $\varepsilon_{xx} - \gamma_{xy} - N_f$ for phase shift 90°, which is shown in Fig. 9.
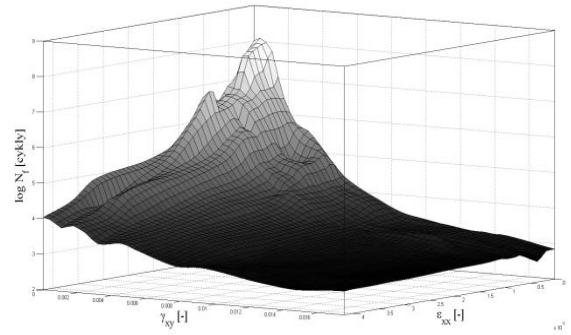
Fig.9 *Three-dimensional fatigue curve ε_{xx} - γ_{xy} - N_f for multiaxial fatigue with phase shift 90°*

Using by Fatigue Calculator software there were calculated values of number of cycles to failure of three-dimensional fatigue curves for phase shift 90°. From the Fig. 10 it can be seen a three-dimensional fatigue curve for Fatemi-Socie criterion, in Fig. 11 can be seen fatigue results for SWT criterion, in Fig. 12 can be seen fatigue results for Brown-Miller criterion and in Fig. 13 can be seen fatigue results for Liu criterion.
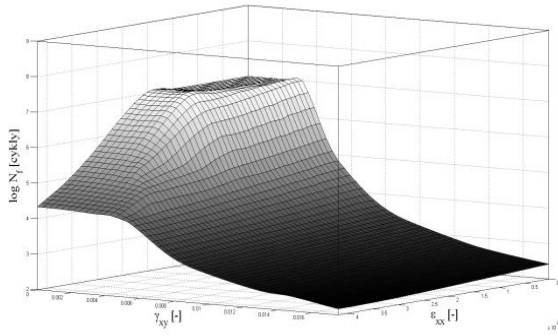
Fig.10 *Three-dimensional fatigue curve ε_{xx} - γ_{xy} - N_f for multiaxial Fatemi-Socie criterion with phase shift 90°*
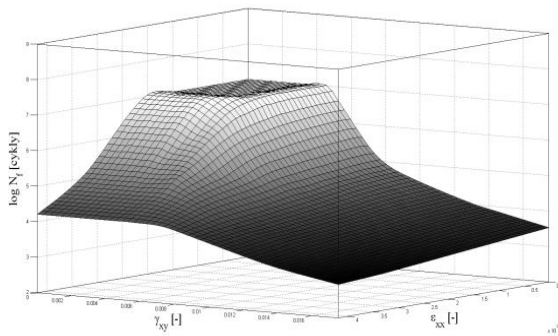
Fig.11 *Three-dimensional fatigue curve ε_{xx} - γ_{xy} - N_f for multiaxial SWT criterion with phase shift 90°*
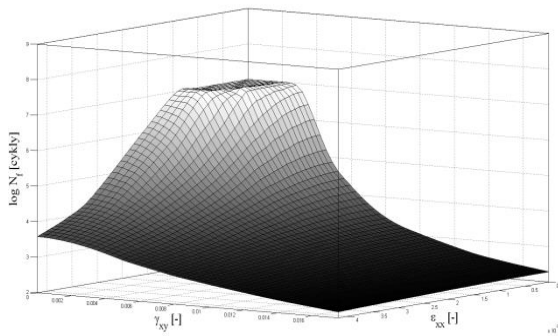
Fig.12 *Three-dimensional fatigue curve ε_{xx} - γ_{xy} - N_f for multiaxial Brown-Miller criterion with phase shift 90°*
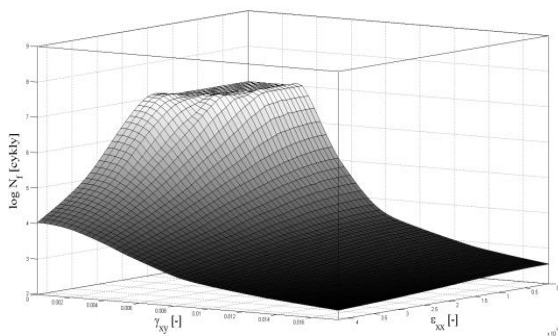
Fig.13 *Three-dimensional fatigue curve ε_{xx} - γ_{xy} - N_f for multiaxial Liu criterion with phase shift 90°*

5. Conclusion

Every multiaxial criteria applied to fatigue lifetime calculation and also values of number of cycles to failure from experiment for specimens of aluminium alloy EN AW 6063.T66 increases with decreasing strain amplitude continuously in the cycles of number region. Comparing three-dimensional curves is evident that criteria from Fatigue Calculator give higher lifetime than experiment in the whole area of the number of cycles at the same load amplitudes. This may be caused by different material parameters, which were used for each models of damage. They probably do not include all real parameters and properties of the comparison of the experimental material that probably affected the sensitivity of the numerical calculation.

6. Acknowledgements

7. References

[1]   www.aalco.co.uk

[2]   HURTALOVÁ, L., TILLOVÁ, E. (2013). *Elimination of the negative effect of FE-rich intermetallic phases in secondary (recycled) aluminium cast alloy*, pp.44-50. Manufacturing Technology, Vol.13, Num.1, ISSN 1213-2489.

[3]   UHRÍČIK, M., PALČEK, P., SOVIAROVÁ, A., SNOPIŃSKI, P., (2014). *Change of internal friction on aluminium alloy with 10,1% Mg dependence on the temperature*, pp.467-470. Manufacturing Technology, Vol.14, Num.3, ISSN 1213-2489.

[4]   BOKŮVKA, O., NICOLETTO, G., KUNZ, L., PALČEK, P., CHALUPOVÁ, M. (2002). *Low & high frequency fatigue testing.* CETRA and University of Žilina, Žilina.

[5]   BATHIAS, C. (2001) *Fatigue in the very high cycle regime*. Vienna, Austria.

[6]   BANNANTINE, J. A., SOCIE, D. F. (1992). *A multiaxial fatigue life estimation technique.* In: Advances in Fatigue Lifetime Predictive Techniques, ASTM STP 1122. Eds: M. R. Mitchell a R. W. Landgraf. Philadelphia, American Society for Testing and Materials, pp. 249-275.

[7]   GOUGH, H.J. AND POLLARD, H.V., (1951). *Some experiments of the resistance of metals to fatigue under combined stresses.* Min. of Supply, Aero Res. Council, RSM 2522, Part I.

[8]   LEGER, J. (1989) *Fatigue life testing of crane drive shafts under crane-typical torsional and rotary bending loads*. Schenck Hydropuls Mag., Issue 1/89, pp.8–11.

[9]   BALDA, M., SVOBODA, J., FRÖHLICH, V., (2003). *Using hypotheses for calculating fatigue lives of parts exposed to combined random loads*, Engineering Mechanics, Vol. 10, Issues 5, pp. 12-15.

[10] CHUNG, Y. S., ABEL, A.. *Low cycle fatigue of some aluminium alloys*. In: Low Cycle Fatigue, ASTM STP 942, H., American Society for Testing and Materials, Philadelphia, PA, pp. 94-106

[11] FATEMI, A. , SOCIE, D. F. (1988). *A critical plane approach to multiaxial fatigue damage including out-of-phase loading.* Fatigue Fract. Engng. Mater. Struct, pp.149-166.

[12] BROWN, M. W., MILLER, K. J. (1973). *A theory for fatigue under multiaxial stress-strain conditions.* In: Proc. Inst. Mech. Engrs, Vol. 187, 1973, pp.745-755.

[13] www.efatigue.com

INVESTIGATION OF THE PARAMETERS OF THE QUALITY AT AN AXISYMETRIC DRAWING

ИССЛЕДОВАНИЕ ПАРАМЕТРОВ КАЧЕСТВА ПРИ ОСЕСИММЕТРИЧНОЙ ВЫТЯЖКЕ

Doctor of engineering, Prof. Nazaryan E. A., Candidate of physicist of mathematical sciences Arakelyan M. M.
PHD student Simonyan A.S. Facullty of Physics-Yerevan State University, Armenia

Abstract : Based on the analysis of the initial equations of the plastic state,established the distribution of strains in the initial and final stages of axisymmetric drawing. The dependencies to assess the accuracy of linear and diametrical sizes taking into account volumetric of strain state.

Keywords: stress, strain, deep drawing, hardening, sheet blank.

1. Introduction.

One poorly developed theoretical problems of the drawing process is to assess the impact of amount and distribution of stress and strain on parameters and strength of precision manufactured parts. The scientific-technical handbooks no calculated based, allowing to determine the maximum possible deviations of linear and diametrical dimensions and strength values at different degrees of deformation and technological characteristics of the materials used [1, 2].

This state is due to the fact that the existing theoretical approaches to the creation of science-based methods for the analysis of the stress-strain state built, as a rule, based on simplifying assumptions, the most important of which are the adoption of the plane scheme strain state, the analysis methods of deformation theory with the approximate conditions of plasticity adoption perfectly rigid-plastic model deformable material.

The decisions derived from such approaches are very approximate and provide a idea of the stress-strain state of the blank. Besides this, the theoretical analysis methods developed in many respects depend also on the interests of authors of scientific studies and carry to some extent subjective.

An essential feature of the drawing process is that initially the same material elements sheet blank, plastically deformed acquire certain identity, characterized by changing the thickness of the accumulated value of deformation due to hardening effects, the change indicator of resistance to deformation.

Obviously, the performance precision linear and diametrical sizes of cylindrical parts of an isotropic material, manufactured by drawing, without the influence of the he elastic aftereffect must be due to the value and distribution of finite deformation and strength parameters under the same conditions - the total and the distribution of the index of deformation resistance.

In the present paper the process of drawing cylindrical parts sets the following tasks:

- *Establishment of settlement dependences allowing to define the dimensions of workpieces with volume strain state;*
- *Determination of the distribution of finite quantities and component deformation and deformation resistance index.*

2.An analysis of the initial stage of the drawing process.

Numerous studies have established that the drawing process starts with plastic deformation of the uncompressed part annular portion of the blank located between the contact zones deforming tools[3,4].At this stage, as you move the deforming tool is increasing stress deformation and plastic deformation of the flange cover the entire piece. Set a balance between effort and drawing resistance to plastic deformation of the flange and the second stage of the process - the retraction flange blank into a die.

At the initial stage of the outer boundary of the plastic material and the field elements are moved radially in opposite directions, and the second stage - in the same direction. In both phases of the size of the plastic zone are continuously changing, so that the process of forming the blank is transient in nature. Therefore, scientifically based methods of analysis of drawing should be based on the theory of plastic flow with the hardening material and of volumestrain state.

Given the complexity of the analysis of the processes occurring in the initial stage of drawing, first consider an axially symmetric tension thin plate with a low-cut, limited radius circular contour r_0 along which the specified uniformly distributed normal stresses σ_ρ

.Existing solutions such tasks usually carried out either for a plate of constant thickness, or for perfectly rigid-plastic model deformable material with plasticity condition for the hypothesis of constant maximum shear stress, thus cannot be used for the task [5].

In [6,7] that the stress-strain state in the process of forming an axially symmetric parts from sheet metal appropriate and convenient to represent the deviatory plane Mises plasticity cylinder in oblique two-dimensional coordinate system. The possibility of such a representation should be the condition on which the incompressible materials for three linear strain are interdependent and have only two degrees of freedom, as well as the assumption that the deformation of the blank with the flange stretching occurs under conditions close to the plane stress[3].

In these studies found that the module current vector magnitude equivalent strain is numerically equal to the value of accumulated deformation (strains rate), the current value of the linear strains are the projections of the vector equivalent strain in the oblique coordinate axes, and the pattern of accumulation of strains in this material element describes the nature of the change in the vector equivalent strain in time.

Consequently, the problem of assessing the performance precision linear and diametrical sizes, as well as the final value of the index of deformation resistance is reduced to the analysis of time-dependent vector fields equivalent deformations.

The [6,7] initial equations of plastic flow under plane stress deformation and axial symmetry, namely the equilibrium equation for the changes in thickness of the material condition of plasticity Mises condition of constant volume equation relating voltage and increment (speed) of strains are shown in single structure and displayed in the deviatoric plane plasticity cylinder as the differential between the radial dependence of tensile stress and strain accumulate $d\sigma_\rho = \sigma_s d\varepsilon_i$.

Acceptance of the power law strain hardening $\sigma_s = A\varepsilon_i^n$ allowed to integrate said differential dependence and dependence to obtain and a component of accumulated strains on a parameter φ ωin the form of:

$$
\left.\begin{aligned}
&\left|\vec{\varepsilon}\right|_1 = \varepsilon_i = \left(\ln K + n\right)\frac{2}{\sqrt{3}}\cos\left(\varphi + \pi/6\right); \\
&\varepsilon_\rho = \frac{\ln K + n}{2}\left(1 + \cos 2\varphi - \frac{\sqrt{3}}{3}\sin 2\varphi\right); \\
&\varepsilon_\theta = -\frac{\ln K + n}{2}\left(\cos 2\varphi + \frac{\sqrt{3}}{3}\sin 2\varphi\right); \\
&\varepsilon_z = -\frac{\ln K + n}{2}\left(1 - \frac{2\sqrt{3}}{3}\sin 2\varphi\right).
\end{aligned}\right\} \qquad (1)
$$

where $\left|\vec{\varepsilon}\right|_1$ - the magnitude of equivalent strain in the initial stage of the drawing process, $n = \ln\left(1 + \delta\right)$ - in the received exponent law strain hardening , δ - relative uniform deformation of the material when tested in uniaxial tension, φ - the angle between the polar axis and the radial strain vector equivalent strain varying within $0 \le \varphi \le \pi/3$ (Fig. 1), $\varepsilon_\rho, \varepsilon_\theta, \varepsilon_z$ - linear deformations, respectively, in the radial and circumferential directions, as well as perpendicular to the workpiece surface, the coefficient of drawing $K = R_0/r_0$ (R_0 and r_0 - respectively outer radius of the workpiece and the radius of the point of the die).

Dependence $\varepsilon_i(\varphi)$ on deviatoric plane is a circle of radius $\left(\ln K + n\right)/\sqrt{3}$ $\left(\ln K + n\right)/\sqrt{3}$, centered on the line $\varepsilon_\theta = 0$ and passes through the origin [6].

The possibility of integrating the differential above depending based on the assumptions made about the same for the considered material element of the vector direction of the increment equivalent strain in the deviatoric plane, which is equivalent to the assumption of proportional relationships change over time component strains $\left(\varepsilon_\rho/\varepsilon_\theta = const\right)$.

Upon receipt of (1) the following dependence for the radial and circumferential stress

$$
\sigma_\rho = \sigma_s\frac{2}{\sqrt{3}}\cos\left(\varphi + \pi/6\right); \quad \sigma_\theta = -\sigma_s\frac{2}{\sqrt{3}}\sin\varphi , \qquad (2)
$$

satisfying Mises plasticity plane stress condition and set of joint solution of the equations of stress and communication increments (speeds) strains with the condition that the volume [7] .

From the analysis of (1) that the resulting solution can be represented as the sum of two deformed states. The first term describes the initial plastic state for ideal rigid-plastic model deformable material ($n = 0$) is the largest size of the plastic zone $\left(K = e\right)$ and characterizes the distribution of strains in the parameter φ. The second term linearly superimposed on the first, describes the increment of strains at a given index in the received power-law strain hardening.

Such an interpretation of the results based on the fact that the oblique axes in the deviatoric plane are logarithmic dimension, whereby it becomes possible additive sum strains.

Dependencies (1) and (2), describing the stress-strain state are closed parametric solution of axially symmetric stretching thin plate with a low-cut, limited circular contour, taking into account the interdependent changes in the thickness of the material and work hardening.

From (1) it also follows that as the indicator, the relative magnitude of the plastic region increases in the direction of the inner contour (reduced radius of the inner contour). This result follows from the condition, according to which the external contour of the workpiece is realized the stress state of the linear compression, regardless of the relative magnitude of the field of plastic and technological characteristics of the deformable material.

In between these kinds of deformed states is a smooth transition from one type to another strain state. The schedule of dependence (1) and (2) as well as the main characteristics of the distribution of stresses and strains in detail in [7,8].

(1) is determined by the highest relative value of the plastic region $R_0/r = \exp\left(1 + n\right)$ (R_0, r - respectively the radii of the outer and inner contours of the plate in a deformed state). Obviously, when $n = 0, r = r_0$, the relative value $K = R_0/r_0 = e\left(\approx 2,718\right)$ and coincides with the results of the prior art for a plate of constant thickness at an ideal rigid-plastic model deformable material [3,5].

3. An analysis of the second stage of the drawing process.

The main problem of analysis of the second step drawing process is obtained for mapping the initial stage parametric solutions (1) and (2) into the material of the deformable medium of the preform. To do this, first consider the process of being drawn into the die blank flange, excluding the effect of hardening $\left(n = 0\right)$ and bending effects on the stress-strain state.

With the reduction of the outer radius of the blank flange material elements moving radially coordinates $R_0 \le \rho \le r_0$, accumulate a certain deformation and radius reaching further move vertically without deforming. At the end of this process for forming cylindrical parts set a specific variable distribution of accumulated strain, the values of which can be determined by the well-known relationship between the parameter φ in the deviatoric plane and relative coordinates ρ/r_0 in a material medium deformable billet.

The previous section established that for a perfectly rigid-plastic model deformable material nature of the distribution of the accumulated deformation in (1) and radial stresses in relative units (2) are similar in the deviatoric plane and described the same functional dependence $F(\varphi) = \left(2/\sqrt{3}\right)\cos\left(\varphi + \pi/6\right)$. From (1) and (2) it also follows that the initial stage of drawing $\left(\sigma_s = \sigma_{0,2}; \varepsilon_i = 0,2\%; n = 0\right)$ blank thickness remains constant, the distribution of radial stresses in relative units of well-known solution has the form $\sigma_\rho/\sigma_s = \ln R/\rho$ [3] on the basis of which (2)

$$
\frac{\rho}{r_0} = K^{\left[1 - \frac{2}{\sqrt{3}}\cos\left(\varphi + \frac{\pi}{6}\right)\right]}. \qquad (3)
$$

For (1) and (3) it is possible to find the distribution of the accumulated strain in the deviatoric plane and forming the cylindrical member. Different range φ of fixed K and (3) defines the relationship ρ/r_0 $0 \le \varphi \le \pi/3$ and the value calculated by the formula $\varepsilon_\theta = \ln\left(r_0/\rho\right)$ district deformations. Among the relevant points of the negative direction of the axis ε_θ drop a perpendicular to the intersection with radial rays φ. Connect the start of oblique coordinate the points of intersection is set equivalent to the vector

field strains for all material elements.Based on the generality of the methodical approach and to simplify the numerical calculations, the outer radius of the plastic zone R_0 is adopted when changing K is the fixed and variable radius of the die is considered r_0.

From trigonometric representation strains in the deviatoric plane (Figure 1) shows $\varepsilon_\rho / |\varepsilon_\theta| = \cos\varphi / \cos(\pi/3 - \varphi)$ where the absolute value of the components of the district, according to (3) shall be determined from the equation $\varepsilon_\theta = \ln(\rho/r_0)$. On the basis of the established relationship between φ the parameter and the relative coordinate ρ/r_0 in a material medium deformable billet it becomes possible to install the distribution component of finite deformations and appropriate equivalent deformations of the vector field

$$\left. \begin{aligned} |\vec{\varepsilon}|_2 &= \frac{|\varepsilon_\theta|}{\cos(\pi/3 - \varphi)}; \\ \varepsilon_\rho &= \left[1 - F(\varphi)\right] \frac{\cos\varphi}{\cos(\pi/3 - \varphi)} \ln K; \\ \varepsilon_\theta &= -\left[1 - F(\varphi)\right] \ln K; \\ \varepsilon_z &= \left[1 - F(\varphi)\right] \left[1 - \frac{\cos\varphi}{\cos(\pi/3 - \varphi)}\right] \ln K \end{aligned} \right\}, \quad (4)$$

where $|\vec{\varepsilon}|_2$ - the magnitude of equivalent strain (cumulative strain) in the second stage of the drawing process.

Figure 1 shows a plot of the component deformation and deformation resistance index at the end of the second stage drawing at $K = 2$ assigned in accordance with (3), to the original plastic state. From the analysis of (4) and provided graphs implies that the radial component of the outer contour near the blank (at a certain distance from the end of the extended parts ($\rho/r_0 = 1.76$) reached the highest value (0.36), and the strain in the thickness achieves the lowest (-0.047) values near the points of the matrix (at some distance from the bottom of the elongated parts $\rho/r_0 = 1.13$). On the basis of (3) and (4) it is possible to define the size of blanks on the set sizes detail and thickness distribution of the generator with volume strain state.

The current value for a given height K and $h(\varphi)$ can be determined by comparing the width $d\rho$ of the ring members on the initial preparation and the increment dh in the cylindrical part, according to the expression $\varepsilon_\rho = \ln(dh/d\rho)$, which, after transformation, taking into account (3) and (4) leads to the following differential equation
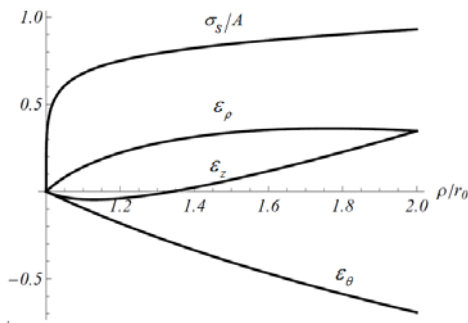
Figure 1. *The distribution of the components of deformation and deformation resistance index at the end of the second stage drawing*

$$d\left(\frac{h}{r_0}\right) = K^{\left[1 - F(\varphi)\right]\left[\frac{\cos\varphi}{\cos(\pi/3 - \varphi)} + 1\right]} \frac{2}{\sqrt{3}} \sin(\varphi + \pi/6) \ln K d\varphi. \quad (5)$$ Integrals

$\int_0^\varphi \Phi(\varphi; K) \ln K d\varphi$ allow us to determine the current value of the relative height of the cylindrical part $h/r_0(\varphi)$ of the annular portion of the blank $\rho - r_0$, as well as the distribution of thickness in a volume strain state.

The main difference between the stated and the actual drawing process is that when drawing deforming tool in a region close to the inner contour of the blank has the effect of limiting the radial movement of certain material elements. Material element initially located at a radius r_0 moves vertically in the absence of circumferential strain $(\varepsilon_\theta = 0)$ and, according to the equation $\varepsilon_\rho = |\varepsilon_z|$, it is deformed in a shear plane $(\rho; z)$.

The vector equivalent strain characterizing the deformation of the element, the deviatoric plane is shifted to the left and becomes perpendicular to the axis ε_θ, and the parameter φ has values in the range $-\pi/6 \le \varphi \le \pi/3$. Absence of circumferential deformation at constant unit vector equivalent strain offset by increased strain thinning.

4. Results and discussion. Let us compare the results of studies with similar results obtained by making assumptions about the constancy of the thickness of the material in the process of drawing cylindrical parts with a diameter $2r_0$ and height h, excluding the radius of curvature [2]:

$$\frac{h}{r_0} = \frac{1}{2}\left(K^2 - 1\right). \quad (6)$$

For the same K values h/r_0, taking into account the volume of strain state, is smaller than the corresponding values calculated by (6) $(2,72 \rightarrow h/r_0 = 2,66; 2 \rightarrow h/r_0 = 1,34; 1,5 \rightarrow h/r_0 = 0,59)$. In expressing this difference as a quadratic trinomial, after determining the relevant standing, we obtain the expression $\Delta(h/r_0) = 1/3\left[(2/3)K^2 - (5/3)K + 1\right]$, from which it follows that the relative height of the cylindrical part, with the of volume strain state $1,5 \le K \le e$ it can be written as:

$$\frac{h}{r_0} = \frac{1}{2}\left(K^2 - 1\right) - \frac{1}{3}\left(\frac{2}{3}K^2 - \frac{5}{3}K + 1\right). \quad (7)$$

From a comparison of (6) and (7) it follows that the relative error of the height of the cylindrical part, without changing the thickness reaches 20%.

Despite some arbitrariness of the analysis obtained calculated dependences allow to determine the relative error of linear and diametrical sizes, as well as indicators of resistance to deformation and to evaluate the quality of cylindrical parts.

5. Conclusion
1. Is given the theoretical accuracyestimateof linear and diametrical sizes and index of resistance to deformation of cylindrical parts in drawing.
2. Set vector fields equivalent deformations for the initial and final stages of the drawing process.
3. Based on the display of finite strains in deformed blank material environment identified characteristic features of the distribution of the radial deformation and deformation in thickness.

6. References

1. Metal *Forming Handbook/Shuler (c) Springer-Verlag, Heidelberg, 1998. 2013, N12,p.23-27*
2. *Forging and* Stamping, Handbook in 4 volumes, ed. E. I. Semenov Volume 4 (Stamping), M., Mechanical engineering, 2010, 544 p.
3. Technology and automation of sheet metal forming, Popov E.A.,Kovalev V.G.,Shubin I.N., , Ed. Bauman MSTU, 2000, 480 p.
4. Electronic handbook of cold forming. Omsk State University, Department of TMF 2006.
5. Hill R. The Mathematical Theory of Plasticity, Oxford Classic Texts in the Physical Sciences, 1998, p.362.
6. Nazaryan E.A., V.F.Konstantinov, Kinematics of deformation in the forming operations of sheet metal stamping // Bulletin engineering. 1999, N 2, S.35-41.
7. Nazaryan E.A., Arakelyan M.M. et al., Mechanics of forming thin ring plates, Izv. NAS RA, Mechanics, 2009, v.62, N4, S.80-88.
8. Nazaryan E.A., Arakelyan M.M., Analytic model of axisymmetric drawing // Blank production in mechanical engineering.

MAGNETIC PULSE COMPACTION AND SUBSEQUENT SPARK PLASMA SINTERING OF NANOSTRUCTURED ALUMINA

МАГНИТНО-ИМПУЛЬСНОЕ ПРЕССОВАНИЕ И ПОСЛЕДУЮЩЕЕ СПАРК-ПЛАЗМЕННОЕ СПЕКАНИЕ НАНОСТРУКТУРНОГО ОКСИДА АЛЮМИНИЯ

Kovaleva I.[1], Zholnin A.[2], Grigoryev E.[3], Olevsky E.[4, 5]
NRNU MEPhI, Russia [1,2,3,4], San Diego State University, USA[5]

Abstract: *The purpose of this paper was to study the regularities of formation of ultrafine structure in alumina by magnetic pulse compaction (MPC) and spark plasma sintering, and the producing of nanostructured compacts having high density and microhardness. The combined application of two technologies magnetic pulse compaction and spark plasma sintering in the practice of compacting powders is very rare and unique. We have studied the microstructures of consolidated alumina samples. The anomalous zones present in volume of magnetic pulse compacted and spark plasma sintered samples of both types α and δ phases of alumina. The microstructure of the fracture surface between anomalous zones depends on the phase state of the particles of the initial powder. MPC of δ-alumina leads to a more uniform distribution of anomalous zones along diameter compact after SPS. MPC of α-alumina leads to an increase of the microhardness on the surface of compacts.*
KEYWORDS: *MAGNETIC PULSE COMPACTION, SPARK PLASMA SINTERING, NANOSTRUCTURE, ALUMINA, MICROHARDNESS*

1. Introduction

The purpose was to study the regularities of formation of ultrafine structure in Al_2O_3 ceramics by magnetic - pulse compression and spark plasma sintering, and getting out of Al_2O_3 nanopowder compacts having high density and microhardness, observed experimentally in [1]. Overview magnetic pulse compaction and spark plasma sintering of powder materials [2] has showed that the combined application of these two technologies in the practice of compacting powders is very rare and unique.

The studies were conducted on the powder Al_2O_3, obtained by the explosion of aluminium wire in the oxygen-containing gas produced by "Advanced Powder Technology", Tomsk. The specific surface area is 35-40 m^2 / g. The mean particle size of 36 nm, an average size from the surface - 45 nm, a mass median size - 54 nanometers. Most of the powder was in a state of δ-phase. The part of the powder was heated in air to a temperature of 1300°C to transfer from unstable low temperature phases to stable α-phase.

2. Experimental results

Spark plasma sintering was performed in vacuum with LABOX-Sinter Land 625 in the graphite mold with an inside diameter of 10 mm at a pressure of 50 MPa. Temperature was determined by pyrometer. The mass of alumina powder was 0.4 g. The thickness of the resulting compacts was a little over 1 mm. Heating was performed at a rate of 100°C / min to 1400°C and staying10 minutes at this temperature.

In conventional pressure compaction was 185 MPa. Pressure at MPC was defined by high voltage discharge. For δ- Al2O3 we have used a single pulse with a discharge voltage of 1.8 kV, and for α- Al2O3 we have used five pulses with a discharge voltage of 2.0 kV. Selected compaction modes correspond to the boundary of the overpressing. If MCP compact was cracked, then it was ground in a mortar and this powder was loaded into a mold for SPS.

SPS results of α and δ phases alumina powders with four kinds of pre-treatment are shown in Figures 1 and 2.
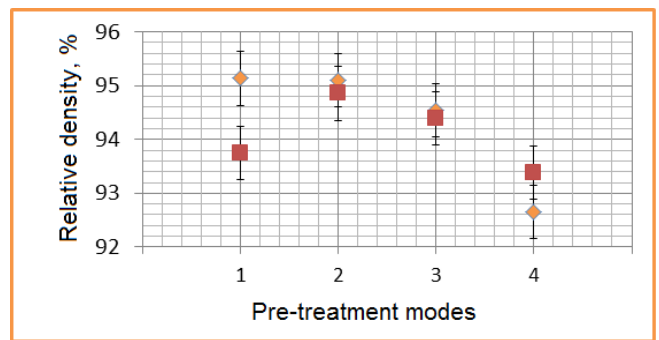
Fig. 1. *Relative density of the SPS compact depending on the type of pre-treatment.*

The numbers on the x-axis correspond to: 1 − the initial powder material (without training), 2 − powder after the traditional pressing, 3 - after the MPC, 4 − milled powder after MPC. Rhombs correspond to the original δ-phase Al2O3 powder, quadrates correspond to the α-phase Al2O3 powder or powder compact before the SPS.
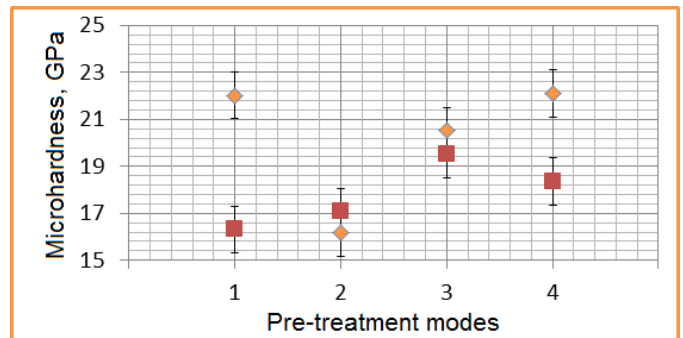
Fig. 2. *Microhardness on the surface of SPS compacts depending on the type of pre-treatment.*

At the fracture surface of the sintered pellets for both types α and δ phases of alumina powders present anomalous zones (AZ) a bimodal structure with length of about 300 microns with a microhardness much higher than on the surface microhardness of compacts (Fig. 3).
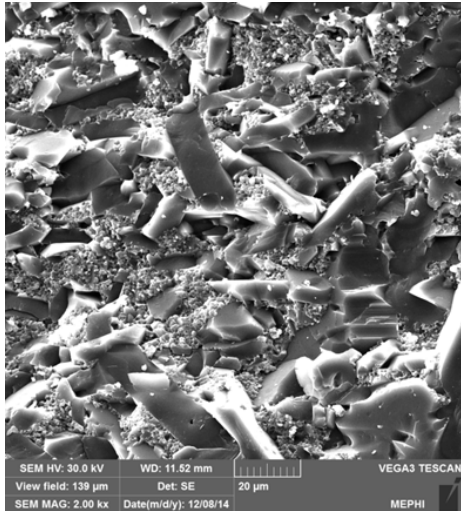
Fig. 3. *Microstructure zones bimodal structure.*

Dimensions of large crystallites in anomalous zones reach 40 microns. The proportion of fracture surface occupied by the anomalous zones increases from the edge to the center of the sample. In the center of the proportion of AZ is up to 40%. MPC leads to a more uniform distribution of AZ along the diameter of compact.
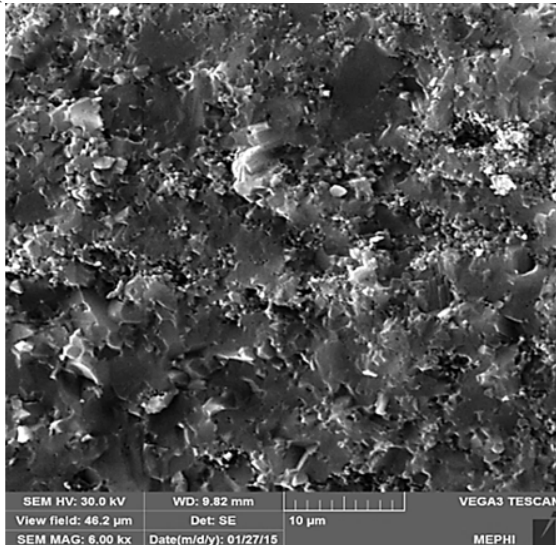
Fig. 4. *Microstructure with alternating coarse and fine-grained layers (mainly for compacts of α-phase Al_2O_3).*

The microstructure of the compact fracture surface between AZ depends on the phase state of the particles of the initial powder. The homogeneous microstructure of δ-Al2O3 powder regardless of the method of pre-treatment has an average grain size of 0.5-0.8 microns after SPS. Fine grains in anomalous zones have a similar

size. The microstructure of α-Al2O3 samples between AZ is bilayer. It consists of layers of large and small grains (Fig. 4).
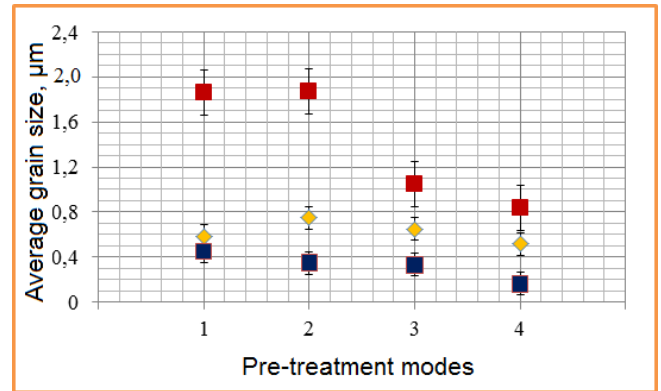
Fig. 5. *The average grain size alumina outside the zones with abnormal structure (coarse-grained layers - red quadrates; fine-grained layers - blue quadrates; original δ-phase Al_2O_3 - rhombs)*

Their dimensions are shown in Fig. 5.

3. Conclusion

Best results for the microhardness and density for all the studied options were obtained by SPS of initial nanopowder δ-Al$_2$O$_3$ without any pretreatment.

MPC of δ-alumina before SPS leads to a more uniform distribution of anomalous zones along diameter compact.

MPC of α-alumina before SPS leads to an increase of the microhardness on the surface of compacts, leads to equalize the distribution of anomalous zones along diameter compact and leads to reduce the size of the grains in a layered structure between AZ.

Acknowledgements

References

1. Lee J.K., Hong S.J., Lee M.K., Sung J.H., Lee C.G., You Y.Z. Fabrication of high-density nanostructured alumina by the combined processes of magnetic pulsed compaction (MPC) and spark plasma sintering (SPS), Solid State Phenomena, 118, 597-602 (2006).

2. Zholnin A.G., Yakushkin A.A., Rykovsky A.I., Grigoriev E.G. Olevsky E.Yu. The current state of technology magnetic pulse compression and its prospects, Nuclear Physics and Engineering, 5, 1, 62-76. (2014).

OBTAINING OF ALUMINIUM FOAM BY INTRODUCING MECHANOCOMPOSITES INTO THE MELT

ПОЛУЧЕНИЕ ПЕНОАЛЮМИНИЯ ВВЕДЕНИЕМ В РАСПЛАВ МЕХАНОКОМПОЗИТОВ

Prof., Dr. Eng., Cor. Member of NAS of Belarus Ilyushchenko A.[1], Cand. Eng., Assoc. Prof. Kusin R.[2],
Cand. Eng., Assoc. Prof. Letsko A.I.[2], Charniak I.[3], Ilyukevich A.I.[2], Zhehzdryn D.[3], Haliakov M. [2]
State research and production powder metallurgy association, State Scientific Institution "Powder metallurgy institute" [1],
Belarusian state agriculture technical university [2], State Scientific Institution "Powder metallurgy institute"[3] - Minsk, Republic of Belarus
E-mail: nil23niipm@tut.by, irinacharniak@tut.by

Abstract *The report focuses on the process of obtaining closed cell aluminum foam by introducing a composite material obtained by high energy mechanical treatment in a planetary mill into the melt. In contrast to known methods, the paper describes the foaming performed by introducing compressed precursors based on aluminum into the melt. Air-atomized aluminum powder and titanium hydride were used as raw materials for the production of precursors, AK5M2 silumin melt was used for the basis. Implementation of these works does not require the creation of a protective atmosphere and equipment for hot pressing. Photographs of the samples' appearance and study results have been presented. It has been shown that the method of introducing mechanocomposites into the melt may be used for the manufacture of closed cell aluminum foam.*

KEYWORDS: ALUMINIUM FOAM, ALUMINIUM-BASED MELT, MECHANOCOMPOSITES, HIGH-ENERGY MECHANICAL TREATMENT, PROPERTIES

1. Introduction

Recently there has been a considerable interest in the development of new compounds and technologies for production of aluminum foam because the products from this material possess an unusual set of properties due to chemical and physical properties of aluminum and the anisotropic structure of the material.

Aluminum foam is a cellular aluminum-based material. There are two types of aluminum foam:

(a) close-cellular; and
(b) open-cellular.

Aluminum foam is widely used in various branches of engineering and construction. It is also applicable for manufacturing filters and heat exchangers, sound insulation material, etc.

The method for production of open-cellular foam aluminum is as follows: Liquid metal is cast into a mould with filler (water-soluble salt with the melting temperature which is higher than the liquidus of the implemented alloy) [1, 2]. After removal of the filler we have a solid with interconnected pores.

Basic methods for production of close-cellular foam aluminum [3, 4, 5]:

Gas purging through the molten Al-SiC or Al-Al$_2$O$_3$. It is the least expensive method which is used for production of foam aluminum with a relative density of 0.03-0.1 and pore diameter of 5-20 mm [3, 4].

Addition of titanium hydride (zirconium) into the melt followed by dynamic stirring, heating and pressure control during cooling of the resulting material [3, 4]. *Mixing of metal powder (mainly aluminum) with titanium hydride (TiH$_2$), followed by melting to a pasty consistency* [3, 4, 5].

Mixing of the charge components may occur as a result of either a direct mixing or simultaneous milling [3, 4], or mechanical alloying of the matrix material by a foaming agent [5]. This technique [3 - 6] involves four steps: preparing powder mixtures of a matrix alloy and foaming agent; compacting; heating to the foaming temperature and aging; cooling. This method is suitable for Al-, Zn-, Fe-, Pb-, and Au- alloys. Foaming occurs by introduction of solid mixed powders of different chemical substances into the metal.

The method of mechanical alloying is a promising method for producing foam aluminum. It involves handling of powder components and their mixtures of various compositions in high-energy mills and the subsequent consolidation of the newly-formed activated mixture for producing semi-finished or finished components [7]. The advantage of mechanical alloying is the use of production waste and scrap of aluminum alloys, which greatly reduces the cost of the process.

In this paper we suggest entering mechanocomposites into the silumin melt in order to obtain close-cellular foam aluminum. Foaming is achieved by introducing pressed mechanocomposites into the silumin melt (Grade AK5M2). The mechanocomposites are obtained from mechanically alloyed aluminum powder and titanium hydride, a foaming agent. The implementation of the process does not require additional machining (obtaining cuttings, grinding etc.) of the matrix alloy, supply of gas medium for foaming the melt, hot [8] or a two stage compacting of mechanocomposites [5].

The purpose of this work is to study the process of obtaining aluminum foam with closed porosity by means of introducing mechanocomposites (based on dispersed aluminum powder) into the melt.

2. Results and discussion

In order to investigate the process of producing aluminum foam with closed porosity we used aluminum powder obtained by spraying molten metal by the gas flow, titanium hydride TiH$_2$ and silumin alloy of Grade AK5M2. The content of the foaming agent TiH$_2$ in the charge of the mechanocomposite Al + TiH$_2$ was Al 99,25 - Ti 0,75 % wt, Al 99,0 - Ti 1,0 % wt, Al 98,5 - Ti 1,5 % wt, Al 98,25 - Ti 1,75 % wt, Al 98,0 - Ti 2,0 % wt; Al 97,75 - Ti 2,25 % wt. The process of preparation comprises the following steps: drying of initial powders, mixing, mechanical alloying, extrusion, foaming.

Drying of initial powders. The powders were dried on stainless steel trays. The depth of filling was not more than 30 mm. Drying was carried out in the oven SNVS 4,5.4,5.4/3I1 at 80 - 90 °C for two hours.

Mixing. In the creation of the mechanocomposite for producing aluminum foam we used the method of mechanical alloying which consists in intensive plastic deformation of the acquired charge in a high-energy mill. Initially suspended samples of dispersed aluminum powder fractions (-0.315 + 0.2) mm and 50 grams of the foaming agent (titanium hydride powder containing 1.5 % by weight of the powder) was placed in the mixer SMB-4 and stirred for four hours at the rotational speed of 60 min^{-1}. The photos describing the morphology of the powder particles of aluminum and titanium hydride are shown in Figure 1.

Mechanical alloying. Mechanical alloying of the powder mixture was carried out in a planetary ball mill RM400MA (Retsch, Germany) at the ratio of 10:1 (the weight of the balls to weight of the processed material). The rotational speed of the planetary disc was 400 rev/min (corresponding to an overload of 26 g) for 30 minutes.
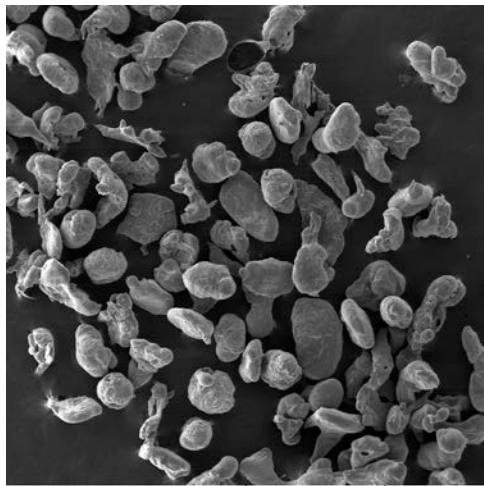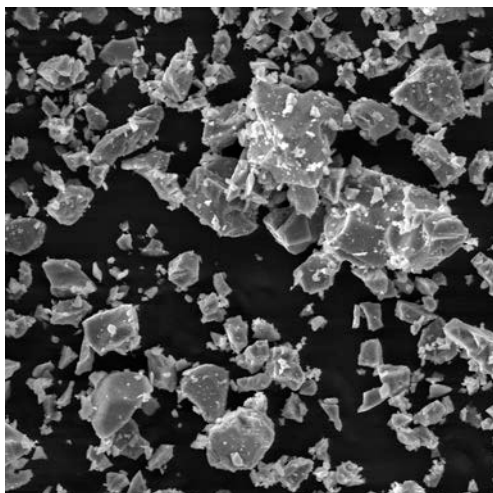
Fig. 1 *Surface morphology of particles in the initial powders*
a) aluminum, atomization of molten metals by a gas flow (argon) × 50;
b) titanium hydride (TiH₂), × 1000
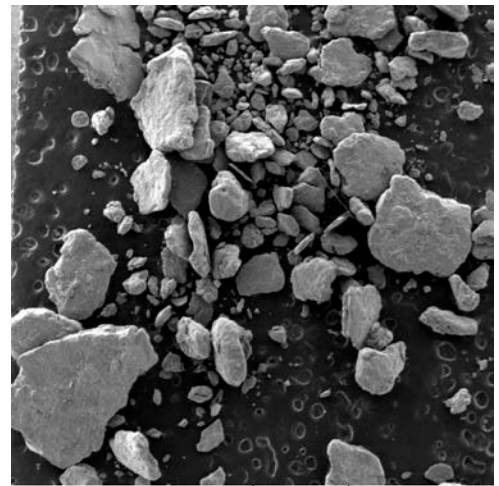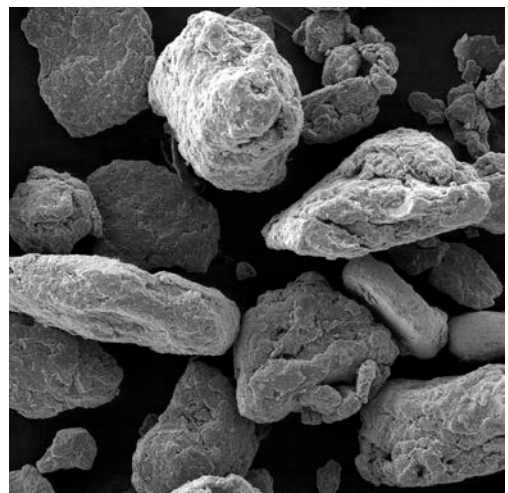
Fig. 2 *Surface morphology of mechanocomposites Al – 1.5% TiH₂, for producing aluminum foam, 30 minutes after mechanical alloying in the planetary mill at different magnifications a) × 34; b) × 200*

We used steel balls (structural bearing steel) of 10 mm in diameter as grinding media. The surface morphology of the acquired mechanocomposites was performed using a scanning electron microscope MIRA from Tescan (Czech Republic) in the backscatter electron mode at accelerating voltage of 20 kW (Figure 2).

The phase composition study of the mechanocomposite $Al + TiH_2$ after mechanical alloying was performed in $Cu_{k\alpha}$ radiation using an x-ray diffractometer DRON-3. The analysis results show that the phase composition of the samples as follows: aluminum (Al), titanium hydride (TiH_2), aluminum hydride (AlH_3), titanium aluminide (Al_3Ti). The X-ray diffraction image of the sample mechanocomposite is shown in Figure 3.
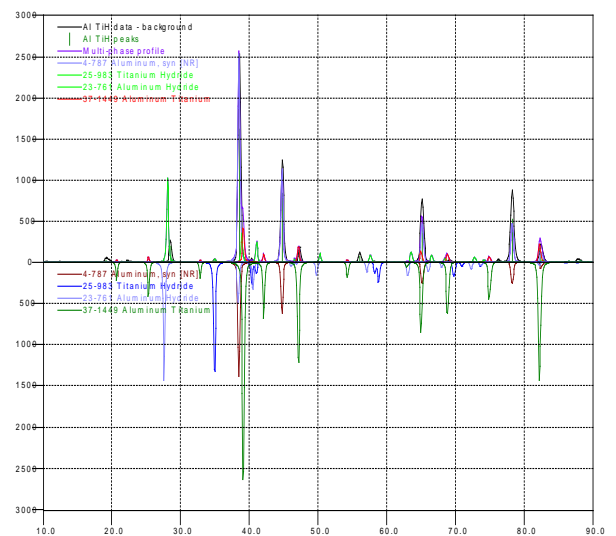
Fig. 3 *X-ray diffraction image of the sample mechanocomposite*
Al + TiH₂

18

During the high-energy treatment a partial interaction of Al and TiH$_2$ takes place with formation of intermetallics Al$_3$Ti and AlH$_3$. Semi-quantitative analysis using the programs DRWIN (point-to-point X-ray processing) and Qual (comparison of the cards with processed X-ray images) is difficult due to the superposition of the main peaks of the identifiable phases.

Extrusion. The sample of mechanocomposite Al + TiH$_2$ was weighed on the scales VK-600 within the accuracy of 0.01 g. It was filled into the forming block with the diameter of 30 mm and then molded in a press type ZD40 at 425 MPa. After molding the preform is extruded from the die. Appearance of compacts is shown in Figure 4.

Fig. 4 *Appearance of a compact made of the mechanocomposite Al + TiH$_2$*

Foaming. Foaming was achieved by introducing compacts of the mechanocomposite Al + TiH2 into the silumin melt AK5M2. The silumin AK5M2 was melted at 700 °C in a muffle furnace SNOL 1.6 equipped with a pot for manufacturing test specimens of foam aluminum by mechanical alloying. The pot with the melt was removed from the furnace chamber and mechanocomposite compacts were added into the melt. While warming up the mechanocomposite to 350-400 °C, decomposition of the foaming agent intensified, together with evolution of hydrogen. During decomposition of the foaming agent the mechanocomposite was destroyed. Its particles were distributed in the melt, releasing hydrogen and foaming the silumin melt. Then the fixture was placed in the refrigerator for the final crystallization of the melt. After cooling, the experimental sample of aluminum foam was taken out. The structure of the aluminum foam is shown in Figure 5.
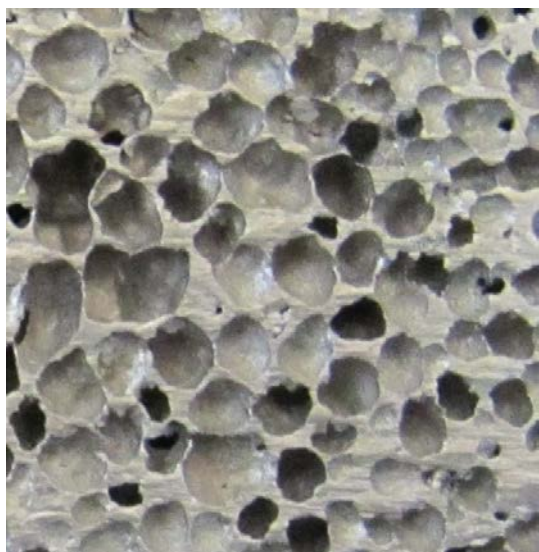
Fig. 5 *Structure of aluminum foam. The mechanocomposite Al + TiH$_2$ contains 1.5 % of the foaming agent (titanium hydride)*

The study of dependence of porosity on the content of the foaming agent showed the following results. When the charge contains less than 1.25 % of TiH$_2$ the porosity of the samples is uneven, some solid portions are not foamed and the close cell rate is low: (48 % or lower). The samples prepared using the charge with 1.25 – 1.5 % TiH$_2$ have a uniform structure, high close cell rate (56 and 63 %) and no cavities. The samples prepared using the charge with 1.75 % TiH$_2$ have uneven structure and contain unmelted inclusions of compacts. When the amount of TiH$_2$ exceeds 2 % the samples have open pore structure, cavities in the surface and a low close cell rate (lower than 55 %).

Based on the acquired data, the optimal composition of a workpiece for processing in a charge shall contain 1.5% of the foaming agent.

The results show that when the mechanocomposite Al + TiH$_2$ contains 1.5 % of TiH$_2$ there is a complete dissolution and uniform distribution of AK5M2 silumin in the melt. We observed a uniform distribution of closed pores without cavities. The porosity of the samples containing 1.5 % of the foaming agent TiH$_2$ was 63 %.

3. Conclusion

The study results show that when the mechanocomposite Al + TiH$_2$ contains 1.5% of TiH$_2$ there is a complete dissolution and uniform distribution of AK5M2 silumin in the melt. The porosity of the samples containing 1.5% of the foaming agent TiH$_2$ was 63%.

It is proved that the proposed method of manufacturing closed cell aluminum foam allows obtaining a uniform structure of closed pores. The method implies introduction of mechanically alloyed atomized aluminum-based powder into the melt.

The described works do not require additional mechanical treatment (shaving, grinding, etc.) of the matrix alloy, admission of gas environment for foaming the melt, hot [8], or a two stage compacting of mechanocomposites [5].

4. Literature

1. Kovtunov A., Khokhlov Y., Chernyshova Y. Technology of manufacturing products from foam aluminum. The proceedings of V All-Russian scientific conference "Problems and prospects of development of aviation, ground transportation and energy "ANTE-2009". 2009, vol. 2, pp. 320-322, (in Russian).

2. Pat. 2400552 Russian Federation, IPC C22C 1/08, C22B 21/00, B22D 21/04. Method for producing foam aluminum. Kovtunov A., Chermashentseva T., Semistenov D., Sidorov V. Applicant and patentee OOO Srednevolzhskij sertifikacionno-diagnosticheskij centr "Del'ta". No. 2008146788/0 dd 26.11.2008; publ. 27.09.2010, Bulletin No.27, 4 p. (in Russian).

3. Butarovich D. Aluminum foam as an energy absorbing material and its mechanical properties (eds. D. Butarovich, A. Smirnov, D. Ryabov) Izvestija vysshih uchebnyh zavedenij. Mashinostroenie, No. 7, pp. 53-58, 2011 (in Russian).

4. Ashby, M.F. Metal Foams: A Design Guide [Text] / MF Ashby, A.G. Evans, N.A. Fleck, L.J. Gibson, J.W. Hutchinson and H.N.G. Wadley, Butterworth-Heinemann, 2000.

5. Ivanov D. Research and modeling of aluminum foam produced by alloying from recycled aluminum raw materials (eds. O. Ivanov, A. Aksenov, I. Ivanov) Izvestija vuzov. Cvetnaja metallurgija. No. 6, pp. 56-61, 2007 (in Russian).

6. Ivanov D. Research and development of aluminum foam produced by mechanical alloying from secondary raw materials. Dissertator: Cand. Sc. Eng: Dmitry O. Ivanov. 05.16.01, Moscow, 2008 (in Russian).

7. Kuzmich Y. Mechanical alloying (eds. Y. Kuzmich, I. Kolesnikova V. Serba, B. Freidin; Executive Editor: E. Poliakov), Moscow: Nauka, 213 p., ISBN 5-02-033726-9, 2005 (in Russian).

8. Ersoy, Emrah. An experimental study on hot formability of closed cell metallic foams (eds. Emrah Ersoy, Yusuf Özçatalbaş, Ersin Bahçeci) The Proceedings of 1st International Symposium: Porous and Powder Materials (PPM 2013), 3-6 September 2013, Izmir Turkey, pp. 68-72; ISBN 978-975-6590-05-8.

CREATING NANOSTRUCTURED SUPERHARD AND HEAT-RESISTANT SURFACE LAYERS ON CARBON TOOL STEEL AT INFLUENCE TO INTENSE ELECTRON BEAMS

СОЗДАНИЕ НАНОСТРУКТУРИРОВАННЫХ СВЕРХТВЕРДЫХ И ЖАРОПРОЧНЫХ ПОВЕРХНОСТНЫХ СЛОЕВ НА УГЛЕРОДИСТЫХ ИНСТРУМЕНТАЛЬНЫХ СТАЛЯХ ПРИ ВОЗДЕЙСТВИИ ИНТЕНСИВНЫХ ЭЛЕКТРОННЫХ ПУЧКОВ

Senior Researcher, Candidate of Engineering Sciences Milonov A.S., Postgraduate Danzheev B.A., Research Officer Dasheev D.E., Main Scientist Researcher, Doctor of Engineering Sciences, Assoc. Prof. Smirnyagina N.N.
Institute of Physical Materials Science SB RAS, 670047, Ulan-Ude, Russia,
e-mail: terwer81@mail.ru, bel.tunka@mail.ru, fokter@mail.ru, smirnyagina09@mail.ru

Absract: *The saturation of the surface layers of metals and alloys boron is conducted with the purpose of increase of their surface hardness, wear resistance, etc. Multicomponent layers containing in its composition borides of refractory metals, as a rule, formed by the methods of chemical-thermal processing in the interaction boriding component with refractory or by saturation boron refractory impurities metal or alloy.*

In this work, we studied the features of formation of vanadium and iron borides on the surface of instrumental steels U8A and R18 under the influence of intense electron beams in continuous and pulse modes.

KEYWORDS: ELECTRON BEAM, BORIDES, ALLOYS, MICROHARDNESS, X-RAY DIFFRACTION, STRUCTURE, THE SELF-PROPAGATING HIGH-TEMPERATURE SYNTHESIS (SHS)

1. Introduction

The surface layers saturation of metals and alloys from boron spend with the purpose of increase of their surface hardness, wear resistance, etc. Application of electronic heating with high (> 10^9 W/m^2) specific capacity in vacuum owing to fast not inertial achievement of limiting heats and ease of regulation of heating in a wide range of temperatures opens sample opportunities for creation of boride layers.

In [1] it was informed about formation of strengthening coating of TiB$_2$, CrB$_2$, VB$_2$, W$_2$B$_5$ on carbonaceous steels under influence of an electron beam on boron compound reactionary daub in vacuum. The assumption of an active role of a surface metal has been made at electron beam alloying of self-heating synthesis products which initiated by an electron beam and proceeding in reactionary daub of steochemetric mixtures.

In this work, we studied the features of formation of vanadium and iron borides on the surface of instrumental steels U8A and R18 under the influence of intense electron beams in continuous and pulse modes.

2. Layers based on the boride VB$_2$ on steel U8A

Vanadium boride layers VB$_2$ (and forth, and borides of iron Fe$_2$B and FeB) at the same time synthesized and formed on the surface of cutting plates size 12×12×5 mm with roughness Rz = 4.41 ÷ 4.02 microns of instrumental steels U8A and R18. Samples were prepared by applying the reactionary daubs on the pre-prepared (well-fat) surface of the steel. In the composition of the daubs consisted of 1:1 by volume stoichiometric mixture oxide, boron containing and carbon component and organic binder - solution 1:10 glue BF-6 in acetone. As initial substances used amorphous boron, charcoal (birch) and oxides V$_2$O$_3$, Fe$_2$O$_3$. Processing of samples was conducted within 2-5 minutes with the power of electron beam 150-300 watts. The pressure in the vacuum chamber did not exceed 2×10^{-3} Pa [2, 3].

X-ray diffraction revealed that in the boride layer on steel U8A observed prevalence of carbide phases (cementite). This can be explained only by the deviation from stoichiometry by evaporation of the intermediate boron oxide. Application of the protective layer of amorphous oxide B$_2$O$_3$ (1:1 by volume reactionary daub: daub based B$_2$O$_3$) allowed to form a more uniform boride layers. It was found that the weight of the crystalline phases in the samples is

92.3%, and the amorphous phases – 7.7%, while the crystallite size ranges from 15 to 70 nm.
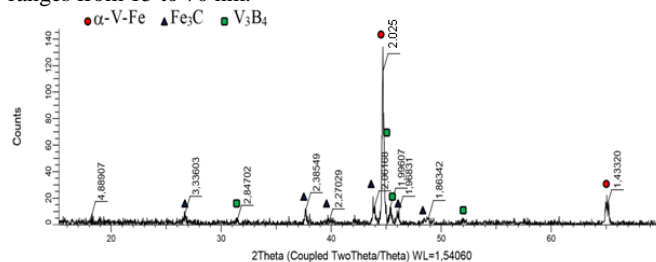
Figure 1. *X-ray pattern of layer based VB$_2$, formed on steel U8A*

On X-ray patterns of all investigated vanadium boride layers can be observed reflections of refractions belonging vanadium ferrite α-Fe-V, the corresponding phase α-Fe$_9$V space group *Im3m*, with a cubic lattice parameter a = 0.2878 nm and cementite Fe$_3$C (PDF 00-003-0989), space group *Pbnm* with rhombic elementary cell with parameters a = 0.4518, b = 0.5069 and c = 0.6736nm, z = 4 (Figure 1).

On X-ray patterns of vanadium diboride layers found boride V$_3$B$_4$ (PDF 03-065-2551, space group *Immm*, with elemental rhombic cell with parameters a = 0.303, b = 1.318 and c = 0.2986 nm, z = 2). Education vanadium diboride VB$_2$ radiographically not detected, although there are reflexes, light intensity related to the interplanar distances of this phase. In this regard, more research is needed.
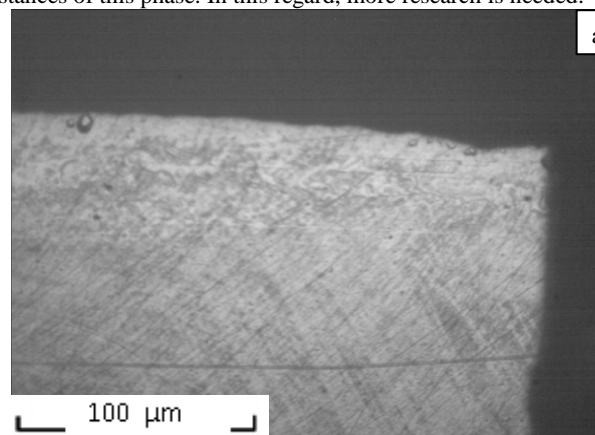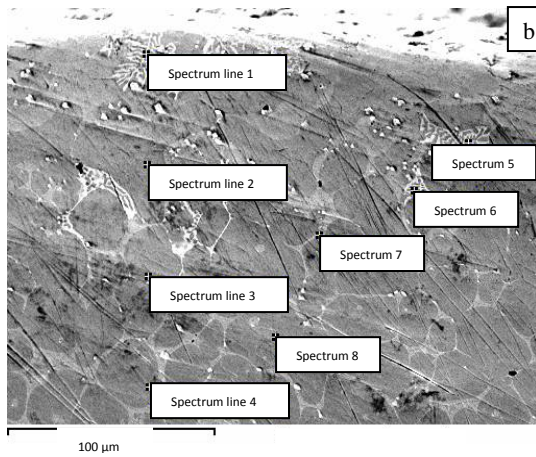
Figure 2. General view (etched layer) (a) and structure (b) layer VB$_2$ on steel U8A

Figure 3. General view (a) and structure (b) boride layer FeB on steel P18

Figure 2 shows a general view (Figure 2.a) and the structure of the boride layer VB$_2$ on the surface of cutter plate steel U8A (Figure 2.b). Layer thickness reaches up to 500 μm.

Microhardness testing showed uneven distribution of its thickness in the cross-section. Separate very rare inclusions have microhardness HV≈ 24000 MPa and are located in the surface layers. Next we will see two areas: in the first area microhardness reaches 2500 MPa, and in second - 1500 MPa. The metal base is microhardness 200 MPa.

3. Layers of iron borides Fe$_2$B and FeB at high-cutting steel R18.

X-ray diffraction (XRD) revealed that in the samples of cutter plate steel R18 after electron beam treatment reflexes following phases are present: the metal substrate - α-Fe and carbide W$_3$Fe$_3$C. It was found that the weight of the crystalline phase is 92.7% and the amorphous phase – 7.3%.

Boride FeB located near the surface of the coating. This is evidenced by the results of the investigation of the end surface of the cutter plate steel R18 and X-ray analysis data (scanning electron microscope JSM-6510LV JEOL with microanalysis system INCA (Figure 3).

Application of the protective layer of amorphous oxide B$_2$O$_3$ contributed obtaining equilibrium boride layers Fe$_2$B and FeB.

Figure 4. Structure of the surface layer on the steel R18 after electron beam boriding, a – at the power density of the electron beam J =2.8×10^4 W/cm^2, b – at the power density of the electron beam J=2.5×10^4 W/cm^2, c,d – at the power density of the electron beam up to J =2.2×10^4 W/cm^2

4. Wear resistance of boride layers on high-cutting steel R18

When the electron beam boriding steel R18 with the power density of the electron beam J =2.8× 10^4 (W/cm^2) layer was formed as a result of deep weld penetration, which determined its structure. Figure 4a shows that when directed crystallization main axis line dendrites oriented in the direction of heat removal. The structure of dendrites (chain separate globules) indicates of the intermittent nature of their education. When power density of the electron beam J=2.5×10^4 (W/cm^2) layer consists predominantly of stellate dendrites (Figure 4b). When reducing the power density up to J =2.2×10^4 (W/cm^2), surface layer also contains stellate dendrites, but their number is not dominant (Figure 4c,d). Microhardness layer is 1100-1860 kg/mm^2. The thickness of layer is 25-100 μm.
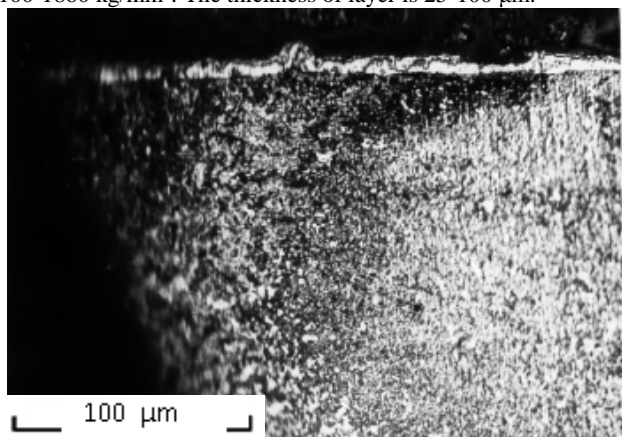
Figure 5. The microstructure of cutters from steel R18 after electron beam treatment

After treatment by the electron beam of cutter plate with boron-containing daubs, on the surface formed layer with thickness 8-10 μm (Figure 5). The resulting layer have a specified thickness practically over its entire length. With increasing × 500 shows that the layer contains particles which are located not only within the layer, but also at the boundary layer - base. This suggests that these particles are carbides of alloying elements (tungsten, chromium, molybdenum and vanadium). Layer was firmly held on the metal base. Microhardness layer slightly higher microhardness is 550 bases and HV and 410 HV, respectively.

To assess the tribological properties of the resulting layer tests conducted strength incisors. Tests were performed on lathes 1A616 on the following modes: feed - 0.1 mm / rev, rate speed - 224 rev /

min, depth of cut - 1.0 mm. Processed material - steel 45 and sus321. Wear incisors determined by the rear surface with a magnifying glass Brinell. Geometric parameters of incisors: rake angle γ= 15°, the main rear angle α = 8°, plan approach angle φ = 45°. Criterion for stability incisors taken the time to reach the limit flank wear of 0.6 mm.

The results are given in figure 6. The figure shows that formation boride layers thickness of 8-10 μm on the front surface, allows to increase the resistance of incisors almost 1.5 times (for processed steel sus321).
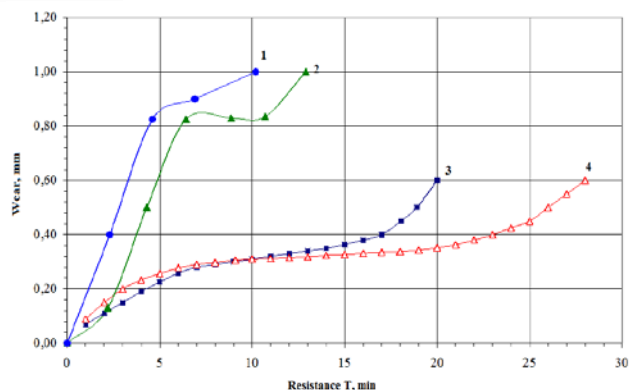
Figure 6. Kinetics of wear cutters from steel R18 1-R18 hard. (steel sus321), 2-R18 thermochemical treatment (steel 45), 3-R18 electron-beam boriding (steel sus321), 4-R18 hard. (steel 45)

5. Conclusion

Conditions for the formation, structure and properties boride layers on the surface cutting plates of carbon steel U8A formed during electron beam processing in vacuum were investigated and discussed.It found that at the directional crystallization the main axis of line dendrites is focused in the direction of heat removal. The structure of dendrites (a chain separate globuly) speaks about intermittent nature of their education. Microhardness layer constitutes 1100-1860 HV. The thickness of 25-100 μm.

The formation boride layers thickness of 8-10 microns on the front surface, allows to increase the resistance of incisors almost 1.5 times (for processed steel sus321).

A more significant increase of resistance incisors are associated with increased thickness boride layers. When electron beam boriding thickness of boriding layer can be up to 300 microns, but the temperature processing is 1100-1200°C. The processing time is 2-3 minutes. On this basis, electron-beam boriding cannot be recommended as a final, but as an intermediate processing operation of the cutting tool, for example, before hardening. It should be noted that to achieve the same thickness of a layer when diffusion borating (for example, when borating in sealed containers with safety valve) is required not less than 3 hours.

6. Acknowledgments

7. Literature
1. N.N. Smirnyagina, I.G. Sizov, A.P. Semenov, Neorgan. Materials. 2002. - vol. 138. - № 1. - pp 48-54.
2. Dasheev D.E., Smirnyagina N.N. Features of the process of self-propagating high-temperature synthesis, a structure and strong properties of borides iron layers on the carbonaceous steel 3, generated under a powerful electron beam in vacuum. // News of higher educational institutions. Physics. - 2012. - V. 55. - № 12/2. - pp. 51-54.
3. Dasheev D.E., Smirnyagina N.N. Features of the process of self-propagating high-temperature synthesis, a structure and strong properties of borides iron layers on the carbon steels, generated under a powerful electron beam in vacuum //J. Chem. Chem. Eng. 2013.- V.7.- № 4.- pp 319-325.

MODELING AND OPTIMIZATION OF THE COMPOSITION OF TITANIUM -BASED ALLOYS BY APPROXIMATION WITH REGRESSION MODELS

Nikolay Tontchev[1], Martin Ivanov[2] Emil Yankov[3]

[1]University of Transport, 158 Geo Milev str.,1574 Sofia, Bulgaria, e-mail: tontchev@vtu.bg

[2] New Bulgarian University – Sofia, [3] "Angel Kanchev" University of Ruse

Abstract: *The article is dedicated to an approach optimizing a task of statistical modeling of the mechanical properties of products in real production metallurgy design. The approach is designed for the benefit of producers-metallurgists aimed at providing panels of Ti - alloys of a specific set of eventual industrial properties. This is accomplished by a procedure of composition optimizing based on existing certificates of brands Ti - alloys. The article presents an approach using mathematical models of optimization problem following the implementation of approach the classical methodology capable of decision-making in the production practice.*

Keywords: METALLURGICAL DESIGN, TENSILE PROPERTIES, COMPOSITION-PROCESSING-PROPERTY CORRELATION, OPTIMIZATION OF THE COMPOSITION

1. Introduction

An effective approach at metallurgical design is to use data from previous experience, processed up to a statistical model, based on a large amount of data related by composition, processing and properties. The design of the alloy composition and the optimization of the technological-process parameters are directly related to the resolution of the compromise between the measured values related to certain selected indicators of the quality of a set of materials for a test group or a class [1]. The most characteristic for these approaches is that they do not use the principles of metallurgy and metal physics. It is relied mainly only on an a priori information about the relation "composition and processing and their influence on the properties." Compared with physical models, the advantage of statistical models is their ability to explore a complex of properties and to obtain information in a timely and effective manner, even when there are no well-established physical theories and models.

The aim of this study is to present a robust approach for determining the influence of alloying elements on the properties of Ti - alloys that ensures better results than the input ones used to obtain a mathematical model.The formulated optimization models are used at the stage of modeling the mechanical properties of the composition of Ti - alloys during the production metallurgy process.

The multidimensional regression analysis is one of the most popular data-mining methods. It has been applied successfully to the study of multiple relationships in metallurgical industry, [2] – [4]. Due to the nature of each statistical analysis, the coefficients of limitations imposed by the regression analysis are known only approximately. That should be reflected in the mathematical model of the optimization problem.

2. General description of the approach

The analysis presented in this paper is related to the analysis of mechanical properties of Ti - specimens described by the following parameters: yield strength, Rp 02 [MPa], tensile strength and relative elongation (A [%]). The limitations connected with these

parameters are due to Ti grade characteristics and customer's specifications. However, the main problem is that these parameters cannot be under direct observation during the manufacturing process, so any limitations associated with them cannot be clearly defined in the optimization model. That means that we must develop models linking the final mechanical properties of the specimen/sample of the steel chemical composition as well as the parameters of the production process.

The regression analysis allows describing the relation between the variables of input and output, without going into the phenomenon nature during the process.

The regression models presented below have been created based on the data collected during the industrial production process.

The statistical analysis described in this section is based on a data set of 300 records extracted from the whole database.

The Pareto front was built based on this initial information related to the couple of parameters yield strength, Rp_{02} [MPa] and relative elongation (A [%]). The chemical composition of the various compositions is given in an implicit form in the case. From the list of compositions in the full range of variations there have been selected Pareto compositions for which the sum of the basic elements had a relatively small value. The selection is focused on compositions for which the relatively small price of their expensive elements does not affect the values of the explored parameters for optimization. The obtained regression models are related to this information. In respect to the problem under examination, nonlinear regression dependencies have been identified for each of the mechanical properties of alloys. The regression dependencies are of the following kind:

Here bij are the regression model parameters. The coefficients in equations are defined in Table 1. The models can be used for prediction if the check-up F > F (0.5, v1,v2) described in details has been made.

The relationship between the derived coefficients in Table 1 and the specific chemical elements is described in the regression elements.

Rp_{02} = 1211.88 + 51.5221 Al - 24.9734 Mo - 80.7796 Sn + 96.9246 Zr + 209.828 Cr + 80.3385 Fe + 72.0976 V - 21.4625 Si + 40.3190 O - 6.81555 Al^2 - 106.347 Al Mo - 69.9600 Al Sn - 43.6439 Al Zr + 15.4261 Al Cr -61.9896 Al Fe -81.5665 Al V + 10.3925 Al Si + 47.3631 Al O + 31.7825 Mo^2 - 24.5042 Mo Sn - 19.5766 Mo Zr - 43.8777 Mo Cr - 34.0499 Mo Fe - 70.3951 Mo V - 51.3807 Mo Si + 60.8373 Mo O + 6.35824 Sn^2 - 62.3299 Sn Zr - 49.0562 Sn Cr + 47.2030 Sn Fe - 84.9186 Sn V + 7.34492 Sn Si + 47.5112 Sn O + 44.0214 Zr^2 -39.5834 Zr Cr - 34.9639 Zr Fe + 19.4983 Zr V + 34.0014 Zr Si + 1.40613 Zr O + 109.626 Cr^2 - 26.3554 C Fe + 12.6771 Cr V + 0.829980 Cr SI - 24.8476 Cr O - 75.0358 Fe^2 + 3.91375 Fe V + 25.5956 Fe Si - 67.2523 Fe O - 6.09390 V^2 + 19.2299 V Si + 17.1889 V O -51.7804 Si^2 +19.0743 Si O -38.5409 O^2

№	designation	Rp $_{02}$	A	№	designation	Rp $_{02}$	A
1	b(0 0)	1211.88	43.4377	29	b(3 4)	-62.3299	7.48801
2	b(1 0)	51.5221	-12.4873	30	b(3 5)	-49.0562	3.57374
3	b(2 0)	-24.9734	5.83605	31	b(3 6)	47.2030	-13.2362
4	b(3 0)	-80.7796	16.1346	32	b(3 7)	-84.9186	18.1995
5	b(4 0)	96.9246	-26.5634	33	b(3 8	7.34492	2.45297
6	b(5 0)	209.828	-41.6628	34	b(3 9)	47.5112	-7.84135
7	b(6 0)	80.3385	-11.3614	35	b(4 4)	44.0214	-12.5869
8	b(7 0)	72.0976	-12.2634	36	b(4 5)	-39.5834	11.2109
9	b(8 0)	-21.4625	9.45284	37	b(4 6)	-34.9639	11.6078
10	b(9 0)	40.3190	-7.32094	38	b(4 7)	19.4983	-1.06720
11	b(1 1)	-6.81555	4.99262	39	b(4 8)	34.0014	-5.39692
12	b(1 2)	-106.347	32.8537	40	b(4 9)	1.40613	3.89560
13	b(1 3)	-69.9600	13.9749	41	b(5 5)	109.626	-11.8927
14	b(1 4)	-43.6439	6.60931	42	b(5 6)	-26.3554	18.2370
15	b(1 5)	15.4261	2.81458	43	b(5 7)	12.6771	12.9706
16	b(1 6)	-61.9896	24.7026	44	b(5 8)	0.829980	0.427527
17	b(1 7)	-81.5665	26.9275	45	b(5 9)	-24.8476	8.14636
18	b(1 8)	10.3925	-4.94533	46	b(6 6)	-75.0358	22.7628
19	b(1 9)	47.3631	-7.11438	47	b(6 7)	3.91375	14.6460
20	b(2 2)	31.7825	-8.72509	48	b(6 8)	25.5956	-10.9786
21	b(2 3)	-24.5042	3.37836	49	b(6 9)	-67.2523	18.1532
22	b(2 4)	-19.5766	1.36551	50	b(7 7)	-6.09390	1.46032
23	b(2 5)	-43.8777	13.8703	51	b(7 8)	19.2299	-4.26022
24	b(2 6)	-34.0499	13.3358	52	b(7 9)	17.1889	-6.80520
25	b(2 7)	-70.3951	18.9816	53	b(8 8)	-51.7804	14.9821
26	b(2 8)	-51.3807	9.02304	54	b(8 9)	19.0743	-5.02353
27	b(2 9)	60.8373	-3.70434	55	b(9 9)	-38.5409	1.21278
28	b(3 3)	6.35824	2.60378				
Rp $_{02}$	R = 0.9880			F cal. = 18.8637 $_{(a=0.05,54,25)}$ > 1.8367 = F tabl			
A	R = 0.9906			F cal. = 24.2416 $_{(a=0.05,54,25)}$ > 1.8367= F tabl			

A = 43.4377- 12.4873 Al + 5.83605 Mo + 16.1346 Sn - 26.5634 Zr - 41.6628 Cr -11.3614 Fe - 12.2634 V + 9.45284 Si - 7.32094 O + 4.99262 Al ^{2} + 32.8537 Al Mo + 13.9749 Al Sn + 6.60931 Al Zr + 2.81458 Al Cr + 24.7026 Al Fe + 26.9275 Al V- 4.94533 Al Si - 7.11438 Al O - 8.72509 Mo ^{2} +3.37836 Mo Si + 1.36551 Mo Zr + 13.8703 Mo Cr + 13.3358 Mo Fe + 18.9816 Mo V + 9.02304 Mo Si -3.70434 Mo O + 2.60378 Sn^2 +7.48801 Sn Zr + 3.57374 Sn Cr- 13.2362 Sn Fe + 18.1995 Sn V +2.45297 Sn Si-7.84135 Sn O - 12.5869 Zr ^{2} + 11.2109 Zr Cr + 11.6078 Zr Fe - 1.06720 Zr V - 5.39692 Zr Si + 3.89560 Zr O - 11.8927 Cr ^{2} + 18.2370 Cr Fe + 12.9706 Cr V + 0.427527 Cr Si + 8.14636 Cr O + 22.7628 Fe ^{2} + 14.6460 Fe V - 10.9786 Fe Si + 18.1532 Fe O + 1.46032 V ^{2} - 4.26022 V Si - 6.8052 V O + 14.9821 Si^2 - 5.02353 Si O + 1.21278 O ^{2}

The numerical experiment [6] has proved the ability to improve the quality of Ti alloy of a certain class. Mathematical models suitable for forecasting and optimization have been derived. The approach of Taguchi applied has lead to a desired result, to separate variables Xi for the examined parameters that do not influence significantly on the final result. With this limit, the numerical optimization for maximum search has been conducted with each chemical composition. That allows improving it. Relative elongation A turned to be less variable index and yield strength Re requires caution with extreme selecting. The decision of bi-criteria problem set has been defined thus proving that the Taguchi approach is applicable to a similar class of problems.Following the applied optimization procedure and based on the derived models, a solution was formulated. According to it, the content of aluminum and molybdenum is about 8-9 percent, and the values of vanadium, chromium and silicon are negligible. Fig. from 1-8 visualizes an interpretation of the main alloying elements and their effect on the investigated variables at fixed values of the rest of the elements that are equal to the determined optimal

Conclusion

It has been proven that during the design of the properties of the materials it is possible to determine effective solutions via defining a multicriteria problem. It has been proven that during modeling process costs for the different Ti - alloys grades in aggregate, it is possible to evaluate equally possible for realization technological routes.Optimal compositions of a Ti-alloys have been determined grade by Pareto-front in terms of strength and ductility that are experimentally verified for a particular application. The number and the amount of alloying elements in low-alloy steels are determined. For Ti - alloys with economic alloying there are constructed models defining the relationship.

References

1. **Tontchev N**. Materials Science, Effective solutions and Technological variants, 2014/3/3, LAMBERT Academic Publishing
2. **Malinov, S, Sha, McKeown, J.J.**: Modelling and Correlation between Processing Parameters and Properties of Titanium Alloys using Artificial Neural Network. Computational Material Science 21, 375—394 (2001)
3. **Potemkin V.K.,O.S. Khlybov, V.A. Peshkov**, Complex mathematical model for predicting mechanical properties and structure of steel sheets, Metal Science and Heat Treatment 42, 11-12 (2000).
4. **Palanisamy P., I. Rajendran, S. Shanmugasundaram**, Prediction of tool wear using regression and ANN models in end-milling operation, International Journal of Advanced Manufacturing Technology 37, 29-41 (2008).
5. **Rodrigues P.C.M., E.V. Pereloma, D.B. Santos,** Mechanical properties of an HSLA bainitic steel subjected to controlled rolling with accelerated cooling, Materials Science and Engineering A283, 136-143 (2000).
6. **Tontchev N., Y. Kalev,** (2013): Determing Influence of Alloying Elements on Properties of Alloys by Robust Experiment, MEST Journal, July, pp. 31 – 39.

Relative elongation (A [%])
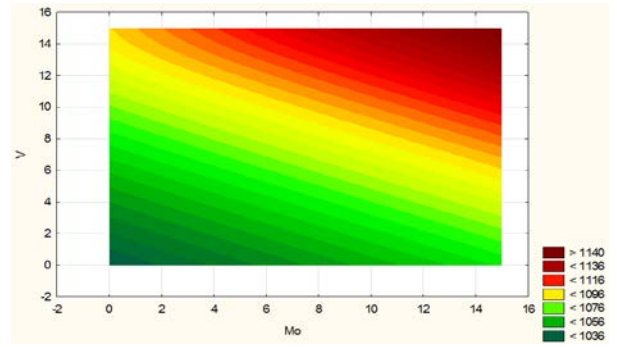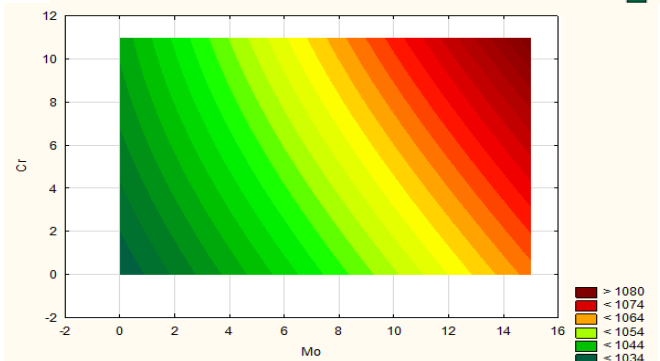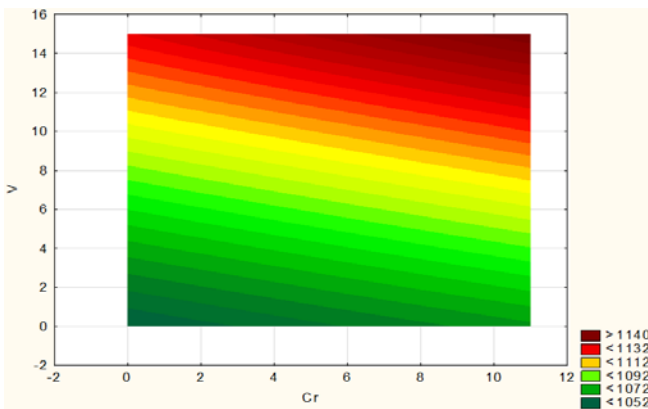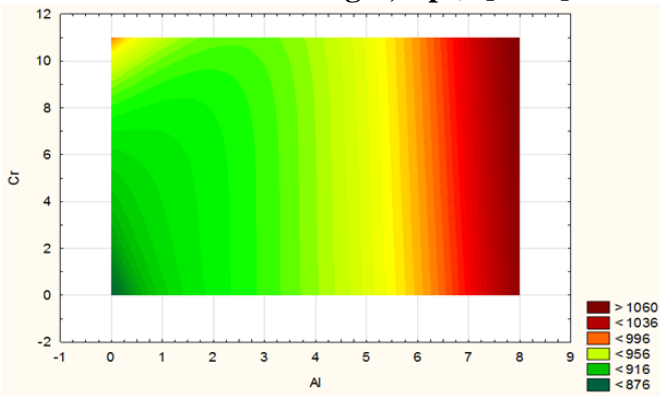
Yield strength, Rp $_{02}$ [MPa]
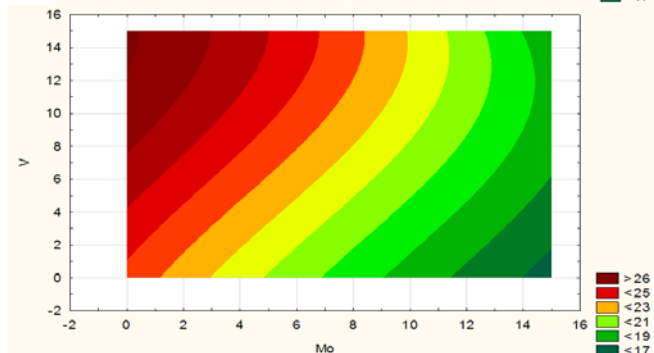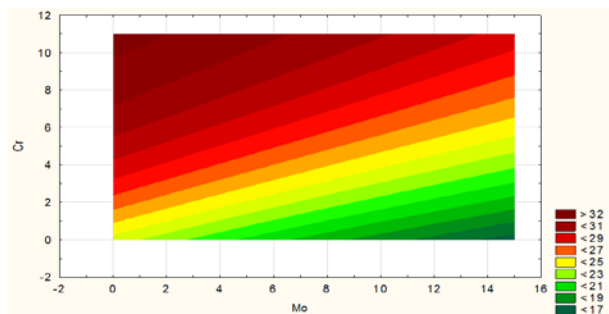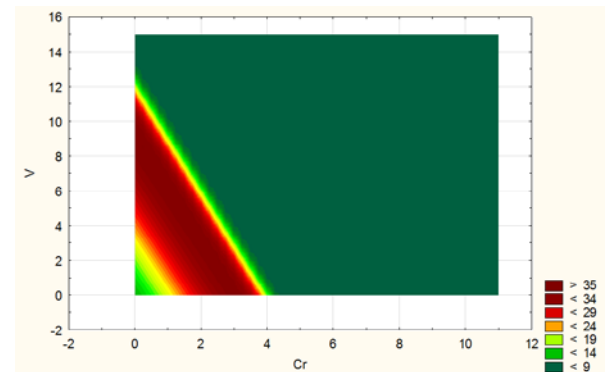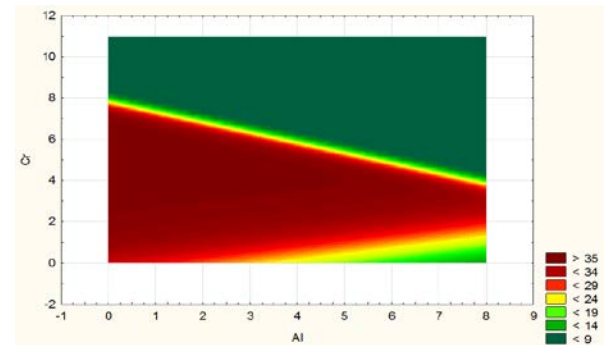
DESIGN OF POLYMER COMPOSITE PIPES PRODUCED BY FILAMENT WINDING TECHNOLOGY

Pop Metodieva[1] B., MSc. Zhezhova S.[1], Srebrenkoska S. [2], Naseva S. [1], Prof. Dr Srebrenkoska V.[1]

[1]Faculty of Technology, University Goce Delchev – Shtip, R.Macedonia
[2]Faculty of Technology and Metallurgy, Ss.Cyril & Methodius University, Skopje, R.Macedonia
E-mail: vineta.srebrenkoska@ugd.edu.mk

Abstract: *The aim of this study is to investigate the design of continuous fiber reinforced composite pipes, produced by filament winding technique. For this purpose, the full factorial experimental design was implemented. When designing filament winding composites three major factors are the most important: fiber orientation, fiber tension and velocity of the filament winding. The ultimate target is to achieve the composite pipes with good characteristics as bearing material for construction with the lowest possible weight. Preparation of the composites was done by applying the 2^3 full factorial experimental design. For the purposes of these investigation, eight test specimen configurations are made and on the basis that, test results should provide material properties useful in the design stage. The velocity of the filament winding was taken to be the first factor, the second – fiber tension and the third – winding angle. The first factor low and high levels were chosen to be 525 m/min and 21 m/min, respectively, for the second factor – 64 N and 110 N, respectively and for the third factor – 100 and 900, respectively.*

KEYWORDS: \ FILAMENT WINDING, GLASS FIBERS, EPOXY RESIN, COMPOSITE PIPES.

1. Introduction

Development of new composites and new applications of composites is accelerating due to the requirement of materials with unusual combination of properties that cannot be met by the conventional monolithic materials. Actually, composite materials are capable of covering this requirement in all means because of their heterogeneous nature (Krivokuća, M. et. al., 1999).

Properties of composites are strongly influenced by the properties of their constituent material, their distribution, and the interaction among them. The composite properties may be the volume fraction sum of the properties of the constituents, or the constituents may interact in a synergistic way so as to provide properties in the composite that are not accounted for by a simple volume –fraction sum of the properties of the constituents (Roux, M, 2010).

Fiber – reinforced composite materials consist of fibers of high strength and modulus embedded in or bonded to a matrix with distinct interfaces between them. In this form, both fibers and matrix retain their physical and chemical identities, yet they produce a combination of properties that cannot be achieved with either of the constituents acting alone. In general, fibers are the principal load-carrying members, while the surrounding matrix keeps them in the desired location and orientation, acts as a load transfer medium between them and protects them from environmental damages due to elevated temperatures and humidity, for example (Dorigato A., Pegoretti A., 2014).

Many fiber-reinforced composites often a combination of strength and modulus that are either comparable to or better than many traditional metallic materials. Because of their low density, the strength-weight ratios and modulus weight ratios of these composite materials are markedly superior to those of metallic materials. In addition, fatigue strength as well as fatigue damage tolerance of many composite materials are excellent. For these reasons, fiber reinforced composites have emerged as a major class of structural materials and are either used or being considered for use as substitution for metals in many weight-critical components in aerospace, automotive, and other industries. Filament winding technique is a very important and widely used technique for production of fiber reinforced composites (Mallick, P.K, 2007).

For the production of composite materials by the filament winding technology, a reinforcing agent in the form of continuous fibers (glass, carbon, aramid, etc.) and an impregnation agent in the form of liquid resin (polyester, epoxy, etc.) are used.

The basis of this technology includes winding of resin-impregnated fibers into a tool and hardening of the wound structure (Figure 1).
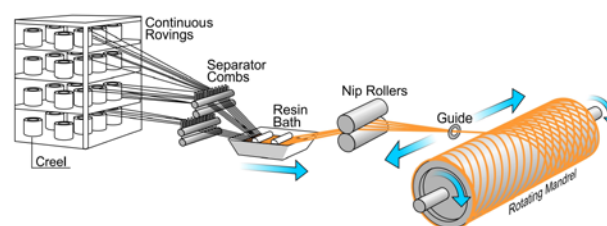
Figure 1. *Schematic presentation of the filament winding technology*

This technology enables the fiber to be placed into the direction of the load that may be expected during exploitation of construction elements. Owing to this unique capability, the mechanical properties of fibers in the longitudinal direction can be maximally exploited (Belingardi, G. et al., 2006).

Based on that, it is clear that the filament winding technology is used for creating new materials with distinct anisotropy according to the direction in which the fiber is placed. In other words, different directions result in a material with different mechanical properties.

Thus produced composite materials have the highest percent of fibers of all composite materials and small density. This fact is important for loaded elements of construction, which also need to have small mass.

2. Preconditions and means for resolving the problem

a. Experimental stand

For the production of the composites 10 bobbins of E-glass fiber roving 185P with 1200tex from Owens Corning were used. The glass fibers were impregnated into epoxy resin system Araldite LY564/Aradur 917/Accelerator 960-1

from Huntsman.

The preparation of the composites was done by applying the 2^3 full factorial experimental design. For the purposes of these investigation, eight test specimen configurations are made and on the basis that, test results should provide material properties useful in the design stage. The velocity of the filament winding was taken to be the first factor, the second – fiber tension and the third – winding angle. The first factor low and high levels were chosen to be 5,25 m/min and 21 m/min, respectively, for the second factor – 64 N and 110 N, respectively and for the third factor – 100 and 900, respectively (Table 1).

Samples with different winding designs were winded on iron mandrel with pins on the both sides with help of laboratory filament winding machine MAW FB 6/1 with six axes, roller type resin bath manufactured from Mikrosam A.D. Fibers pass through a resin bath after tensioning system and gets wet before winding operation. After winding samples were cured with industrial heater at 80oC and at 140°C, for four hours.

Table 1. *Full factorial experimental design - 2^3*

No. exp.	Matrix of full factorial experimental design							Characteristics (conditions of the experiment)		
	X_1	X_2	X_3	$X_1 X_2$	$X_1 X_3$	$X_2 X_3$	$X_1 X_2 X_3$	X_1 (m/min) velocity of the filament winding	X_2 (N) fiber tension	X_3 (°) winding angle
1	-1	-1	-1	+1	+1	+1	-1	5,25	64	10
2	+1	-1	-1	-1	-1	+1	+1	21	64	10
3	-1	+1	-1	-1	+1	-1	+1	5,25	110	10
4	+1	+1	-1	+1	-1	-1	-1	21	110	10
5	-1	-1	+1	+1	-1	-1	+1	5,25	64	90
6	+1	-1	+1	-1	+1	-1	-1	21	64	90
7	-1	+1	+1	-1	-1	+1	-1	5,25	110	90
8	+1	+1	+1	+1	+1	+1	+1	21	110	90

Primary level	$X_1 = 13,125$	$X_2 = 87$	$X_3 = 50$
Interval of variation	7,875	23	40
Lower level	5,25	64	10
Upper level	21	110	90

3. Results and discussion

Tensioning system is an important part of filament winding. This importance gets critical when winding at high angles. Since tension changes the friction force between fiber and the mandrel, it should be kept at a certain value during winding operation (Jones, R. M., 1998).

Fiber tension also affects the volumetric ratio of composite at a given point. Excessive resin, due to a low tension, can result in decreased mechanical properties (Putic, S., et. al., 2007). Therefore, tensioning systems should be capable of rewinding a certain value of fiber. This condition occurs when fiber band reverses at the end of tube, while winding at low angles.

Wetting can be done by two commonly used bathing type: drum bath and dip bath.

Drum bath provide: less fiber damage than dip bath, this is especially important when using carbon fibers, drum baths can be heated for a better wetting action, lowering resin viscosity, reducing fiber speed, increasing fiber path on the drum are other methods used for better wetting action.

Dip bath provides: a better wetting action, resin can be heated during the travel of fiber through a dip bath, non-rotating surfaces are used for guidance, non-rotating surfaces provide good wetting, dip baths are used with aramid or glass fibers. Each layer of reinforcement can vary in winding tension, winding angle, or resin content.

In filament winding, one can vary winding tension, winding angle and/or resin content in each layer of reinforcement until desired thickness and strength of the composite are achieved. The properties of the finished composite can be varied by the type of winding pattern selected (Babu, M., et al., 2009). Three basic filament winding patterns are:

1) Hoop Winding: It is known as girth or circumferential winding. Strictly speaking, hoop winding is a high angle helical winding that approaches an angle of 90 degrees. Each full rotation of the mandrel advances the band delivery by one full bandwidth (Figure 2).
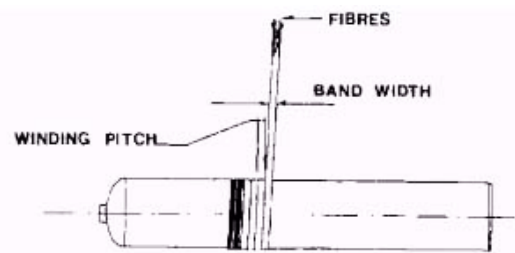
Figure 2. *Presentation of hoop winding of layers*

2) Helical Winding: In helical winding, mandrel rotates at a constant speed while the fiber feed carriage transverses back and forth at a speed regulated to generate the desired helical angles (Figure 3).
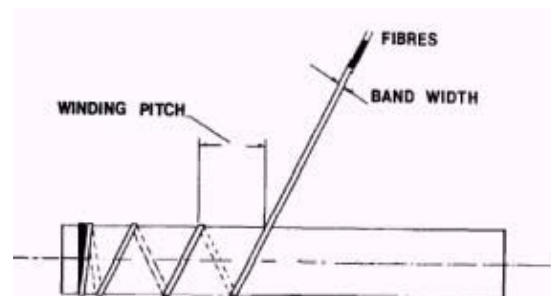
Figure 3. Presentation of coupled helical winding of layers

3) Polar Winding: In polar winding, the fiber passes tangentially to the polar opening at one end of the chamber, reverses direction, and passes tangentially to the opposite side of the polar opening at the other end (Figure

4).
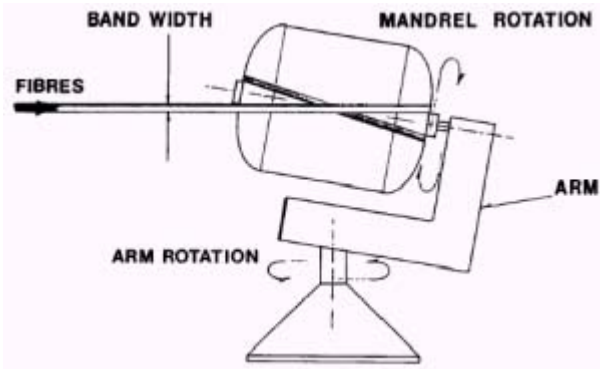
Figure 4. Presentation of polar winding of layers

In other words, fibers are wrapped from pole to pole, as the mandrel arm rotates about the longitudinal axis as shown in Figure 2. It is used to wind almost axial fibers on domed end type of pressure vessels. On vessels with parallel sides, a subsequent circumferential winding would be done.

In the above three, helical winding has great versatility. Coupled helical winding of layers ($\pm\Theta$) are usually preferred, whereas hoop winding - winding angle, very close to 90° can also be used. Very low winding angle values need some arrangements at the ends of the mandrel, such as pins, etc. By varying the winding angle with respect to the mandrel axis, directional strength can be obtained by considering the loads, which will operate on the finished product. Almost any combination of diameter and length may be wound by trading off wind angle and circuits to close the patterns. Usually, all composite tubes and pressure vessels are produced by means of helical winding.

Filament winding is a manufacturing process which can offer:

• A high degree of automation;

• Relatively high processing speeds (> 50 m/min winding speed);

• An ability to fabricate composites with relatively high fibre volume fractions (~ 70%).

The main limitation of filament winding technique is the difficulty in production of complex shapes due to the requirement of very complex mandrel designs. In addition, production of reverse curvature parts is not possible by using this technique.

Figure 5. Produced glass fiber/epoxy resin filament wound composite pipes

4. Conclusion

The glass fiber/epoxy resin composite pipes were produced by using of filament winding technology. For the designing of the filament winding composite pipes the full factorial experimental design - 2^3 was applied. Base on that eight test specimen configurations were made. Three major factors were taken and two levels of variation. The first factor low and high levels were chosen to be 5,25 m/min and 21 m/min, respectively, for the second factor – 64 N and 110 N, respectively and for the third factor – 10^0 and 90^0, respectively. The effect of a filament-winding processing variables on longitudinal and hoop tensile and bending properties of the prepared composites further will be investigated. The produced filament wound composite pipes are shown on figure 5.

5. References

1. Babu, M. S., Srikanth G. & Biswas, S. Composite Fabrication by Filament Winding - An Insight. AEC/MECH/2009.
2. Belingardi, G., Cavatorta, M. P., Frasca C., Compos. Sci. Techol. 66, pp. 222-232, 2006.
3. Dorigato A., Pegoretti A., J. Compos. Mat., 48, pp. 1121-1130, 2014.
4. Jones, R. M., Mechanics Of Composite Materials (Materials Science & Engineering Series) Hardcover – July 1, 1998
5. Krivokuća, M., Putić, S., Uskoković, P. Aleksić. R., Uticaj strukture na savojna svojstva laminarnog kompozitnog materijala, III Jugoslovenska Konferencija o Novim Materijalima YUCOMAT 99, Herceg-Novi, Zbornik izvoda, (1999), p.228.
6. Mallick, P.K., Fiber-Reinforced Composites: Materials, Manufacturing, and Design, Third Edition (Mechanical Engineering), 2007.
7. Putic, S., Stamenovic, M., Zrlic,M., Bajaceta, B, Bending properties of Glass – Polyester Composite Pipes, 3th International Conference on Deformation Processing and Structure of Materials, Belgrade, 2007.
8. Roux, M., Reinforced Nanocomposites for electrical Applications, Master thesis, European School of Material Sciences and Engineering, France, 2010.

DETERMINING OF STRAIN RATIO IN TENSILE TEST
USING BY IMAGE PROCESSING

Ass. Prof. Dr. Daei Sorkhabi A. H., Eng. Vahdat Panahi Shokouh V., Eng. Parsa Khanghah S.
Department of Mechanical Engineering, Tabriz Branch, Islamic Azad University, Tabriz, Iran.
Email: amirsorkhabi@iaut.ac.ir

Abstract: *In tensile machines to measure the change in length of the specimen during the stress, most time extensometer and various contact methods and tools, such as strain gauges are used, but these methods have limitations and low accuracy that cause unexpected and different results from the theoretical values for the strain. In this paper, to address this shortcoming and improve strain measurement, a non-contact method using image processing techniques in the MATLAB environment is introduced. for this purpose after capturing a move of tensile test and converting that in to some high quality pictures and using image processing we put some pattern in the first image and with using a special algorithm with name of Digital Image Correlation (DIC) detect that patterns until the last image then we can use of displacement algorithm and calculate change in the specimen's length and after that we can also have "Strain" with using these values.*

KEYWORDS: DIGITAL IMAGE CORRELATION, PATTERN RECOGNITION, STRAIN

Introduction: Nowadays we can see in order to perform strain test and record strain-stress changes, many of corporations or Academic Centers use of tensile machines. In these devices two different mechanisms measure the force and length change. For measure of the force they use of the change in length of the spring or use of force meters. Also the general mechanism for measuring the change in length of the specimen is using of strain gauge or Shaft encoder or Extensometer that all of these conventional instruments have special limitation for themselves. Therefore, in this study, to reducing these deficiencies in tensile testing machine we prepare a new and non-contact method that use of image processing to solve these problems. Fig 1)
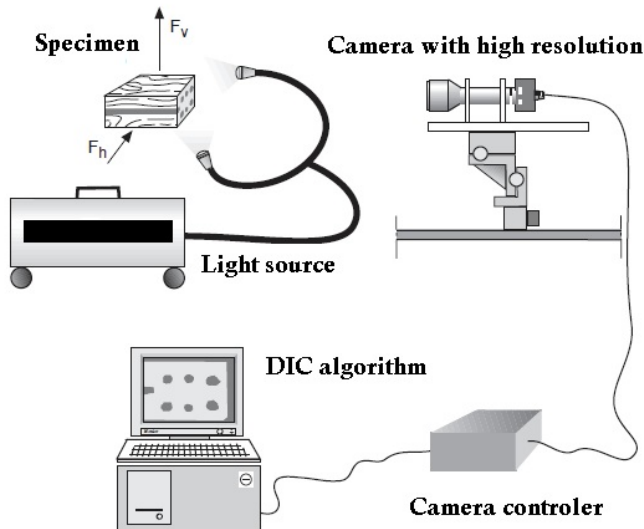
Fig. 1: *A schematic overview of research*

As you see tensile test specimen is connected to the machine and after that a camera with a high speed shooting capture movie as our specimen tolerate a force Then algorithms for image processing and digital image correlation function in MATLAB environment, measure variability of the sample. New method for detecting changes in the length is using of digital image correlation [1]. Image processing is a new and very powerful technique in computer science and electronics which has been implemented in several studies in various fields. For example, Shell and Nicola have used this method to achieve their goals [2,3].The use of image processing has many advantages, for one it is not difficult like conventional methods and also it has good accuracy. We can say there are several algorithms for computing the strain of an object that most common of them is based on image correlation. Correlation or cross-correlation between two images is a standard approach for the detection of object features which has also been widely used to measure the surface deformation. This method of analysis is called digital image correlation (DIC) which can detect form of shape and its movement. DIC is an optical metrology based on digital image processing and numerical computing. It was first developed by a group of researchers at the University of South Carolina in the 1980s [4–8] when digital image processing and numerical computing were still in their infancy [8]. In this technology some spot (like black and white points) will be selected in the surface of specimen and then we will take a picture. Now our pattern is ready. Many of these patterns will be prepared before deformation and also after deformation. These patterns will be then sent to the computer after digitization. In the next step digital images will be compared with each other. Generally a subset of pixels (30×30 or 40×40) from original picture will be selected. The algorithm works like this:

Position of the subset in the first picture will be searched in the second picture with matching of Gray Levels and for each point will be calculated a level of Gray light intensity and therefore we can find the closest match points in the second image with the original image subsets. Thus, the position of the points in the secondary image is obtained. After getting these subsets in the second picture we can have movement amount of specific points. Fig 2 can show an overall view of this topic:
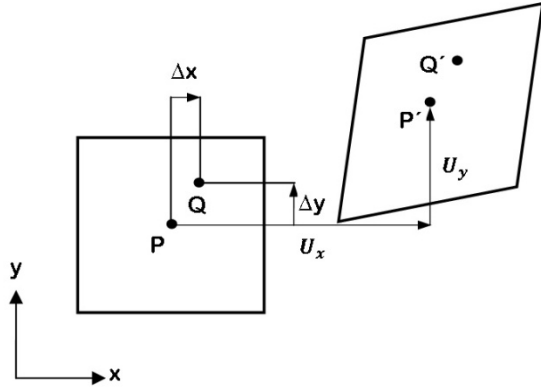
Fig 2. *Moving points in successive images*

In order to better estimate the displacement, one particular factor "S" is defined as the normalized cross-correlation:

$$(1) \quad s\left(x,y,u_x,u_y,\frac{\partial u_x}{\partial x},\frac{\partial u_x}{\partial y},\frac{\partial u_y}{\partial x},\frac{\partial u_y}{\partial y}\right)=1-\frac{\sum I_u(x,y)I_d\left(x^*,y^*\right)}{\sqrt{\sum I_u(x,y)^2 \sum I_d\left(x^*,y^*\right)^2}}$$

here u_x and u_y are movement parameters in the center of subset. I_u and I_u show Gray levels from Original image and the deformed image respectively. (x, y) and (x^*, y^*) are Coordinates of the point before and after deformation. So that the Coordinate of (x^*, y^*) after deformation is related to (x, y) before deformation.

$$(2) \quad x^* = x + u_x + \frac{\partial u_x}{\partial x}\Delta x + \frac{\partial u_x}{\partial y}\Delta y$$

$$(3) \quad y^* = y + u_y + \frac{\partial u_y}{\partial x}\Delta x + \frac{\partial u_y}{\partial y}\Delta y$$

We should also mention that all of this work can be performed in the MATLAB environment. In other words, we can advance our project with help of image processing toolbox functions and there is no need for the user to use more complex formulas.

The core of the correlation tool is based upon a Matlab routine which uses a normalized cross correlation to correlate a part of the source image with the target image (Fig 3). This routine uses the grey scale levels of the pixels in the area of interest. The routine returns for each pixel in the target image a correlation value between -1 and 1. The value 1 means that the part of the source image is exactly the same as the area in the target image, 0 means that no correlation exists and -1 means that the analysed area in the target image is a negative of the source image. Because DIC is an image based technology, a pixel based coordinate system is used. In this correlation tool the X and Y coordinate within an image are defined as shown in Fig. 3. The correlation square is always uneven with the pixel of interest exactly in the centre of this square. The size of the square must be such that enough detail of the specimen surface is included such that the square is unique. For instance if only one pixel is taken in the example, many

locations exist in the target image which are the same. In the correlation tool the size of this square can be adapted.
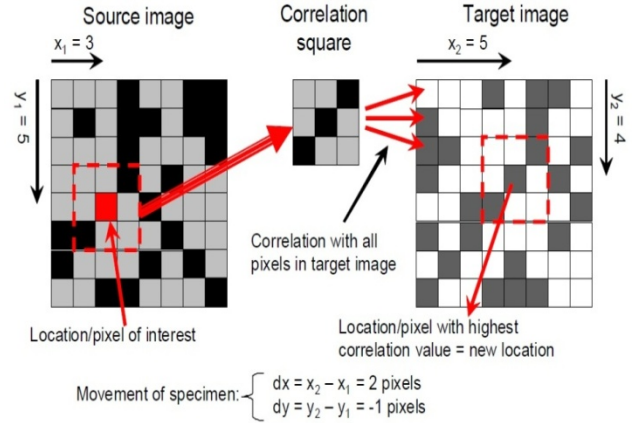
Fig 3. *Correlation process for one pixel*

The correlation square is compared with all the pixels in the target image, returning a correlation value for each pixel, resulting in a data set as illustrated by Fig 4. The location in the target image that corresponds best to the correlation square is clearly recognized by the peak with the highest correlation value. However, the new coordinate has an accuracy of 1 pixel which is not accurate enough for strain measurements. To get higher accuracy a method was developed which uses the correlation values around the peak to get sub pixel level accuracy. To obtain that a 6th degree polynomial surface is fitted through the correlation values of the pixels around the pixel with the highest correlation value, using a least squares approach. By filling a grid of sub pixel coordinates into the function of the fitted polynomial surface, a new maximum can be obtained at sub pixel level. In the correlation tool the resolution in which the coordinates are given is 0.01 pixels. It was found that a higher resolution did not further contribute to the accuracy of the measurement [19].
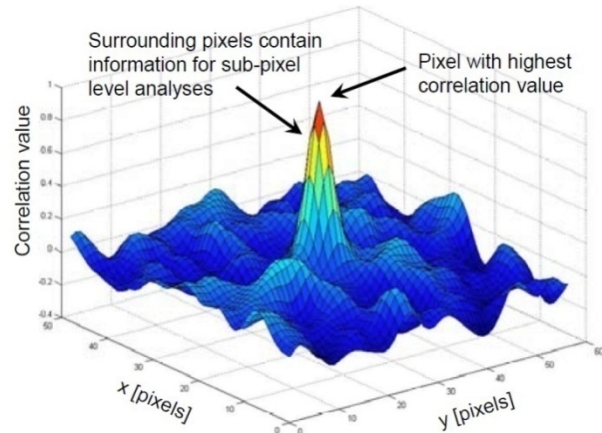
Fig 4. *Correlation values for an area in a target image*

Implementation:

The main processing in this test is defined like this:

For the first step we should prepare some pictures from our specimen before deformation. In this test, in order to remove possible vibrations, for example vibrations caused by the tensile test machine, we use of video camera. Finally, we can prepare some good pictures without any vibration. For this purpose we use a software that is suitable for video cameras (Fig 5). Other available software may be used for the purpose of this research.
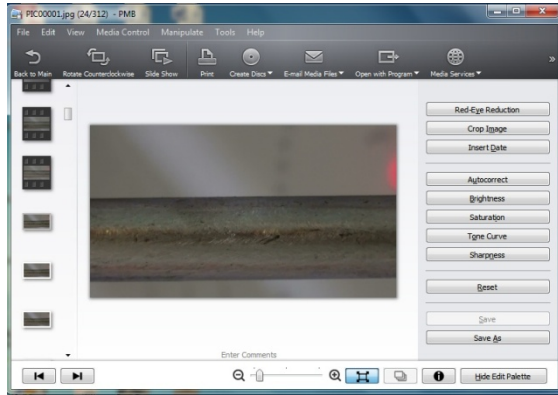
Fig 5. *PMB software from "SONY" corporation*

as we mentioned we have a video camera that its specifications is as follows(Fig 6):

Lens: Carl Zeiss® Vario-Tessar / 30m
Zoom Ratio (Optical) 25X
Zoom Ratio (Digital) 300X

In the next step the prepared images should be processed. For this purpose all pictures are sent to the MATLAB environment. After this the first image will be called for processing. With help of written codes we can select a desire region for processing. We will do that with making a rectangle region (Grid) that can be processed. In simple terms, the image processing code will only focus on these points. Fig7 and demonstrate an example of this way.

Fig 6. *Shoot picture with XR150E.*

.

Fig 7. *Select the desired region for processing*

As it can be seen in Fig 8 we have some yellow points for processing although in this level we can increase a points density which will be more accurate. However, the processing time will increase. In fact we can say processing time relates both parameters. First number of pictures and second point density

In the third phase, correlation algorithm starts and searches points in the first image onto the second image. This is done using "Cpcorr" function in the MATLAB environment. This function using normalized image correlation algorithm and match its input arguments that they have acquired from both pictures first, before deformation and second, after deformation. As a result, coordinates of specified points in the first picture will be emerged in the second picture. (To learn more about this function refer to the MATLAB Help). Although it is noteworthy we should have image processing toolbox in MATLAB. After finding the location of specified points in the second picture they will save and process will be continued in the third picture and like this process will be gone until the final stage. It should also be noted that if "Cpcorr" function cannot detect the position of some points it will return points to its previous position. In this case some points that are static in their position during the processing will be demonstrated. Also we should say if we increase the points density in the first stage its probability will be less that "Cpcorr" function don't be able to detect position of points or in other word Noises will decrease dramatically. However, processing some area like this will require a computer system with powerful processors. Two different phases of image processing are visible in Fig 8
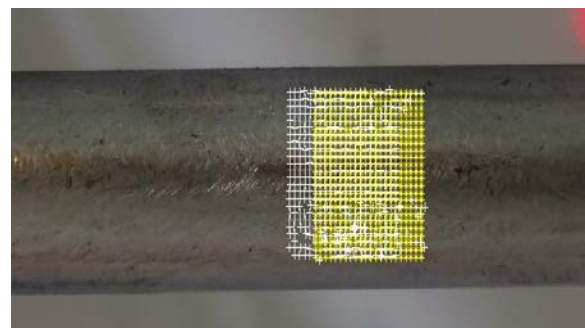
Fig 8. *Coordinates of the points in picture 32*

In the fourth phase we can get the desired amount of displacement or traction during the test using the coordinates of points obtained for each image and processing and mathematical calculations on them. The result of the process will have two matrices. A matrix for the x coordinates of the points in each image and also other matrix y coordinates for the points in the same image. (Fig 9)
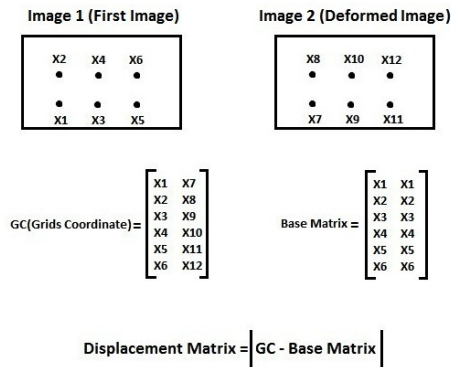
Fig 9. Calculating displacement matrix in X dimension

Now with caring that the displacement matrix is available, we can calculate strain. It can be said the core of this research at this stage will implement like this:

It uses "GC" matrix, Displacement Matrix, and also a function with name of "Lsqcurvefit" in "matlab" optimization toolbox to calculate optimal strain. Optimal strain for processed pictures will fit with a liner function and then strain amount for each picture will detect.

Result: With caring to image correlation Algorithm and also calculations the results will be presented like bellow: The plot (Fig 10) is related to the strain in the tensile direction. As shown, the strain is specified for each image.
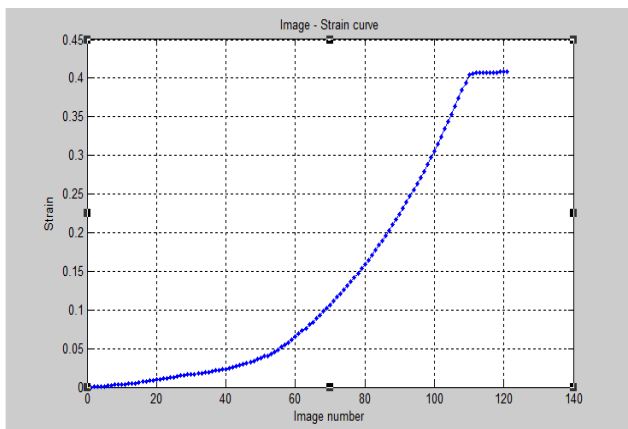
Fig 10. Strain plot in a tensile direction

Conclusions: With considering the results that are obtained through image correlation Algorithm and using of image processing techniques we can say although this method needs more accuracy during test but obtained results show our information after test can be reliable and even sometimes it can compete with conventional methods. So we can use of this method for an alternative ways for calculating Poisson's ratio.

References:

[1] Bing Pan, Kemao Qian, Huimin Xie and Anand Asundi. (2009), "Two-dimensional digital image correlation for in-plane displacement and strain measurement",Measurement Science and Technology., 20, 062001

[2] Nicolella D.P., Nicholls A.E, Lankford J.and, 2001,Davy D.T, Machine Vision Photogrammetry: a technique for measurement of microstructural strain in cortical bone, journal of Biomechanics, 34,135-139.

[3] G'Sell C., Hiver J.M. and Dahoun A.,2002, Experimental characterization of deformation damage in solid polymersunder tension, and its interrelation with necking, International journal of Solids and Structures 39,3857 3872.

[4] PetersWH and RansonWF 1981 Digital imaging techniques in experimental stress analysis Opt. Eng. 21 427–31

[5] Chu T C et al 1985 Applications of digital-image-correlation techniques to experimental mechanics Exp. Mech.25 232–44

[6] Sutton M A et al 1986 Application of an optimized digital correlation method to planar deformation analysis Image Vis. Comput 4 143–50

[7] Peters W H et al 1983 Application of digital correlation methods to rigid body mechanics Opt. Eng. 22 738–42

[8] Sutton M A, McNeill S R, Helm J D and Chao Y J 2000 Advances in two-dimensional and three-dimensional computer vision Topics in Applied Physics 77, 323–72

COMPARATIVE ANALYSIS OF THE ANALYTICAL METHODS FOR ASSESSING THE PRECISION OF THE MEASURING SYSTEM

Mr. Eng. Gjakovski I[1], Executive manager Dr.Eng. Brkovski D[2], Prof.Dr.Cvetkovski S[3]
Insurance Policy AD[1], RZ Inter-transsped AD Skopje[2] Macedonia, Faculty of Technology and Metallurgy[3] Skopje, Macedonia,
E-mail: ivan_gjakovski@yahoo.com, dean_brkovski@intertranssped.com.mk, sveto@tmf.ukim.edu.mk,

Abstract
The results of performed analysis and the study of analytical methods for assessing the precision of the measuring system are presented in this paper. Studies are related to the methods for assessing the precision based on the range calculation and the method of variances analysis (ANOVA). The importance of each factor in variation inducation in the measurement process is estimated by applying both methods in the analysis of the same measured sample. In order to assess the accuracy and efficiency of the applied methods, the obtained results are compared, which is the basis for obtaining specific conclusions. Reliability of the obtained results from the investigations are verified by applying the tools of programming package MINITAB.

KEYWORDS: PRECISION, ANALYTHICAL METHODS, MEASURING SYSTEM, VARIATIONS

1. Introduction

Modern measurement techniques has developed various measuring devices. Certain types of measuring devices have different specific properties, but also some common general characteristics that allow comparation. One of the basic metrological characteristics of the measuring device is its precision.

Measuring equipment precision - is the ability of the measuring device to show the similar measured values (Figure 1).

1) accurate and precise 2) inaccurate and precise

3) accurate and impreccise 4) inaccurate and imprecise
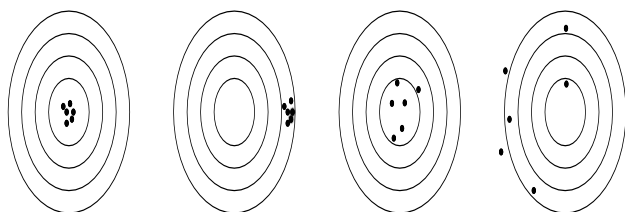
Figure 1: *Possibilities of accuracy and precision or inaccuracy and imprecision of a measurement [G1]*

The metrological charastheristics – measurement precission contains two typical aspects [G1] :

- repeatability of the measurement results, the degree of mutual overlapping of each measurement results obtained in mutually multiple repetition of the measuring operation over a measured value, which value is time-independent (constant), using the same measurement equipment, the same operator and the same ambient conditions.
- reproducibility of the measurement results, the variations that occur when multiple realization of the measurement process, using the same measurement equipment and different operators.

In practice, analytical and graphical procedures are used for assess the measurement systems accuracy. Analytical procedures for the determination of repeatability and reproducibility of the measuring system are aimed to determine (quantify) which part of the calculated variations of the observed measurement process are due to the variations of the measuring system, while graphical procedures allow analysis of the measurement process.

Analytical methods for repeatability and reproducibility calculation of the measuring system, which are subject of this paper can be:

• Method based on range, which assess the measurement variations by comparing the standard deviations of the factors in the measurement process. This "traditional" method divides the total variation in three categories: variations from product to product (variations induced in the manufacturing process), measurement repeatability and reproducibility (variations caused by the measuring system).

• ANOVA (Analysis of Variance) method - investigates the effects of one or more qualitative inputs (factors) on the quantitative outputs, that helps assessing which of the factors have the most significant impact on the output (answer). ANOVA Gauge R & R is a method which uses ANOVA random effects model for measurement systems analysis. This method calculates the level of variations induced in the measuring process of the measurement system and compares it with the total variation in order to determine the "quality" of the measuring system, i.e. its participation in the total variation. This method goes a step forward in terms of the first method and the component reproducibility is separated in two subcomponents: operator and operator - measured sample component in interaction.

Which analytical method will be applied depends on the measurement nature. If it is a non-destructive test (test sample after measuring retains all its properties), there is possibility to use both analytical methods.

In the case of a destructive test (test sample after measuring loses its characteristics, and repeated measurement is not possible) can be applied only ANOVA - method. The of homogeneity of the tested samples serie should be assumed, i.e. all samples in the tested

serie sufficiently identical to be able to consider operation with the same samples. Otherwise the variations of the process will "mask" the variations of the measuring system.

2. Preparation, planning and realization of then engineering experiment

In order to realize the analysis of the measuring system accuracy as a function of the measuring equipment and operator, it is necessary more operators to measure more samples on the same measurement equipment several times in reference conditions. Experiment is prepared from the measured samples. The aim is as much as possible sources of variation to be covered in the measurement process in order to be properly understood and assessed.

The aspect of measurement reproducibility to be covered, it is necessary the participation of more operators. Some standards [A1] require the participation of at least ten operators, but others require participation of only two or three operators for the same sample measuring.

To cover aspects of the measurement repeatability, the same samples are measured several times by the same operators. Each measurement cycle of each sample must include the whole set of required operations, including the complete handling, sampling and disposal of the measuring sample from the measuring system.

To include the interaction between the operator and the sample (eg some sample could be more difficult for measuring than the other samples), usually five till ten samples are measured.

Of course, this is not a universal criteria for the minimum samples recommended for R & R matrix. This is the question for the person which manage the experiment to establish a balance between the risks, measurements and laboratory ability. Model 10x2x2 (10 samples, two operators and two repetitions of measurements) is acceptable sample for certain studies, although there are little degrees of freedom for the component of the operator.

In order the measuring sample to be considered as relevant for further processing and carry out more valid conclusions it is necessary to check the existence of harsh errors and their elimination and verification of the fulfillment of the conditions of normality and homogenity of the measuring sample:

1) As a first step in the process of determining of the participation of measuring equipment and operator in the total level of variations from the set of measured values by applying the Grabs criteria [G2], harsh errors are identified and eliminated for measured values of each operator separately.
2) In the next step of the analysis, it is necessary to test the fulfillment of the conditions for normality of measured results and homogeneity of the variations. This is done through testing the hypothesis by applying more tests:
- for testing of normality: λ - test, λ- test, Anderson – Darling, Ryan – Joiner, Kolmogorov – Smirnov test, by using of probability diagram or by p - value analyze e.t.c.

- for testing of homogeneity: z – test, Student t – test, Fisher F – test e.t.c.

3. Results

Example number 1. *R&R Analisis of the mearuring system precision*

<u>Table 1:</u> *Measured values in the analysis of the components to the measuring system precision.*

Number	FIRST OPERATOR		SECOND OPERATOR	
Product	First measurement	Second measurement	First measurement	Second measurement
1	50,08	50,08	50,06	50,06
2	50,04	50,05	50,04	50,04
3	50,03	50,02	50,04	50,02
4	49,99	49,96	49,98	49,98
5	50,10	50,08	50,08	50,06
6	49,98	50,00	49,99	50,00
7	50,08	50,06	50,10	50,09
8	49,99	50,00	50,01	50,01
9	50,02	50,02	50,00	50,01
10	49,96	49,94	49,98	49,99

By the implementation of Grabs test for the series of measurements on the first and the second operator high values of p – indicator can be seen, significantly bigger than the level of trust α = 0.05 (p = 1.000 for the first operator, and p = 0.923 for the second operator) and can be concluded that in both series of measurements do not exist unusually measurements – harsh errors.

Although it is about series with a relatively small number of measurements (twenty measurements in serie), the two series of measurements (from the first and the second operator), show a high degree of compliance to normal distribution (p = 0.199 for the first operator, and p = 0.168 for the second operator),
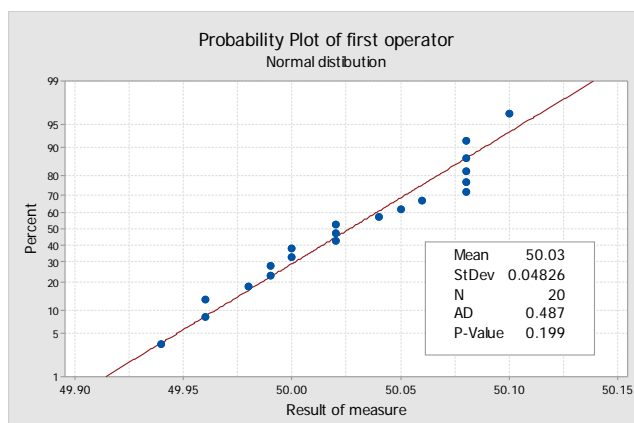
Figure. 2 *Analysisof the measurind results normality by using of probability diagram*

The existence of consistency of the variations and their uniformity can be determined by using of t – test for analysis of the homogeneity of the variations of whole measured sample.

Table 2: *Calculated values in the analysis of the components to the measuring system precision using a balanced ANOVA - method.*

Sources	Var. comp.	% Participation	Standard deviation	% Participation
Measuring system	0,0002381	12,58%	0,0154290	35,47%
Repeatibility	0,0001025	5,42%	0,0101242	23,27%
Reproducibility	0,0001356	7,16%	0,0116428	26,76%
Operator	0,0000000	0,00%	0,0000000	0,00%
Product*Operator	0,0001356	7,16%	0,0698570	26,76%
Product	0,0016544	87,42%	0,2440490	93,50%
Total variations	0,0018925	100,00%	0,2610170	100,00%

Table 3: *Calculated values in the analysis of the components to the measuring system precision using a method based on range*

Source	Var. Comp.	% Participation	Standard deviation.	% Participation
Measuring system	0,0001039	7,36%	0,0101950	27,13%
Repeatibility	0,0001039	7,36%	0,0101950	27,13%
Reproducibility	0,0000000	0,00%	0,0000000	0,00%
Product	0,0013078	92,64%	0,0361635	96,25%
Total variations	0,0014117	100,00%	0,0375731	100,00%

4. Conclusion

Both methods for assess the accuracy of the measuring system show that the manufacturing process is the most important factor that induces variations. Variations of the measuring system according to ANOVA – almost equally is due to the repeatability (variation of the measuring instrument) and reproducibility (variations induced by the interaction of the operator and the measuring sample). Because the method based on range did not detect variations from the interaction of the operator and the measuring sample, the whole measuring system variations are shown for repeatability.

• Procedure for analysis of the components on variation and procedure for standard deviation factors analysis are used in the analysis of the measuring system. The obtained results with both procedures are equally indicative. Which metrics will be used depends on the purpose of the research. If the measuring system is used in process for improvement, (reduction of variations in the manufacturing process), analysis of the components of variations is used, and if assessed the quality of the product in terms of meeting the specified values, then analysis of the standard deviations is used.

• Ability of ANOVA - Method to assess the variations caused by interaction of the operator and measuring sample makes this method more effective in detecting the sources of variation. Furthermore, only ANOVA – Method is applied in the realization of the analysis of the measuring system in the case of destructive test. The application of ANOVA method can significantly improve the view for measuring system precission by fulfillment of assumptions for realization of engineering experiment, by possession of mathematical, technical and practical experience of the operator and computer supported analytical process.

5. Literature

[A1] ASTM E 691 *Standard Practice for Conducting an Interlabaratories Study to Determine the Precision of a Test Method*

[G1] Ѓаковски Иван – Анализа на методите за дефинирање на метролошките карактеристики на мерните алати, Магистерска работа, Универзитет Свети Кирил и Методиј, Машински Факултет – Скопје, Јуни 2012.

[I1] ISO/IEC: GUIDE TO THE EXPRESSION OF UNCERTAINTY IN MEASUREMENTS 1995.

[M1] MINITAB RELEASE 17.0.1 – STATISTICAL SOFTWARE

[P1] Patki Mukul – Investigation, Improvement and Extension of Tecniques for Measurement System Analysis, Oklahoma State University Stillwater, Oklahoma.

THE RESISTANCE OF AISI 316Ti STEEL TO PITTING IN 1 M CHLORIDE ACIDIC SOLUTION IN THE ABSENCE AND PRESENCE OF INORGANIC INHIBITOR

RNDr. Viera Zatkalíková, PhD., Ing. Lenka Markovičová, PhD., Ing. Miroslav Omasta, Ing. Monika Oravcová

Department of Materials Engineering, Faculty of Mechanical Engineering, University of Žilina, Slovakia

viera.zatkalikova@fstroj.uniza.sk

Abstract: AISI 316Ti stainless steel is prone to local corrosion in aggressive chloride environments. Its resistance to pitting in the absence and presence of molybdate inhibitor was tested by two independent tests with different mechanisms of corrosion process: by exposure (24 hours immersion test) and electrochemically (potentiodynamic polarisation test). Both tests were carried out in 1 M chloride acidic solution without inhibitor and with two different amounts of added inhibitor (concentration ratio inhibitive/aggressive anions was 1:10 and 1:20 respectively), at room temperature. Results of immersion tests were evaluated on the bases of corrosion rates calculated from corrosion losses during immersion and by morphology of pitting. Results of potentiodynamic polarisation tests were evaluated by pitting potentials.

Keywords: STAINLESS STEEL, PITTING CORROSION, MOLYBDATE, IMMERSION TEST, POTENTIODYNAMIC TEST

1. Introduction

Austenitic stainless steels have high resistance to uniform corrosion in oxidation environments due to their passive oxidic surface film. However, aggressive ions present in environment (namely chlorides) cause local breakdown of this protective film and they enable a progress of the pitting corrosion. This corrosion type is very dangerous and deleterious and it may cause a major failure in industrial applications [1-4]. The best way to prevent the pitting corrosion attack is developing new highly resistant alloys. The major disadvantage of these materials is their high cost compared with conventional stainless steels due to the higher percentage of the alloying elements such as Cr, Ni, Mo as well as the complexity of the fabrication process [5]. The favorable effect of some alloying elements e. g. Cr and Mo can be achieved by their addition into aggressive solution in the form of nonaggressive anions (molybdates MoO_4^{2-}, chromates CrO_4^{2-}) that can adsorb on the metal surface, strengthen the passive film and inhibit the pitting corrosion process [5].

Many authors underline that a corrosion inhibitor acts effectively only above a certain concentration ratio of non-aggressive to aggressive anions [1, 2, 6]. The authors [6] apply the ratio between concentration of molybdate ions and concentration of chloride ions 1:10 and they document positive effect of the inhibitor on the embryonic stages of pitting corrosion (metastable pitting) and on the value of the pitting potential as well (in acidic chloride solution). However, there are some authors, who have tested inhibitors added into solution in a very broad interval of concentration ratios, and they also bring positive results about their inhibitive effects [4, 5, 7, 8].

According to many authors, chromans are very efficient pitting corrosion inhibitors [1, 2, 4-6], but they have an important disadvantage. These species are highly toxic and therefore ecologically unfriendly and handling them requires very strict rules. From this point of view molybdates are much more suitable for ordinary use.

AISI 316Ti is Cr-Ni-Mo austenitic stainless steel stabilized by Ti widely used in various industrial and biomedical applications [2, 3, 5, 9]. In spite of its wide use and high Pitting Resistance Equivalent Number (PREN=23.688) [10] this steel is prone to local corrosion failure in chloride solutions [2, 3, 5, 9].

This paper deals with the pitting corrosion resistance of the above mentioned steel in the absence and presence of sodium molybdate (Na_2MoO_4), which was tested by 24 hours immersion test and by potentiodynamic polarisation test. Both tests are independent, with different mechanisms of corrosion process. They were carried out in 1 M chloride acidic solution without inhibitor and with two different amounts of added inhibitor (concentration ratio inhibitive/aggressive anions was 1:10 and 1:20 respectively), at the temperature of 20 ± 3 °C. Results of immersion tests were evaluated on the bases of corrosion rates calculated from corrosion losses during immersion and by morphology of pitting (observed visually and by optical microscope). Results of potentiodynamic polarisation tests were evaluated by pitting potentials.

2. Experimental material

AISI 316Ti stainless steel with chemical composition listed in Table 1 was used as an experimental material.

Table 1: Chemical composition of experimental material (wt. %)

Cr	Ni	Mo	Mn	N	Ti
16.5	10.6	2.12	1.69	0.012	0.41
C	Si	P	S	Fe	
0.04	0.43	0.026	0.002	balance	

Microstructure of experimental material (optical metallographic microscope Neophot 32) in longitudinal section is shown in Fig. 1. It is created by polyedric austenitic grains with observable twins, which could be created by annealing or by rolling. Parallel lines arose by the rolling during the technologic process. Observed microstructure contains numerous carbides. (Mo, Ti)C carbides are of cubic shape, $(Mo, Cr)_{23}C_6$ carbides [11] are localized along the above mentioned lines.
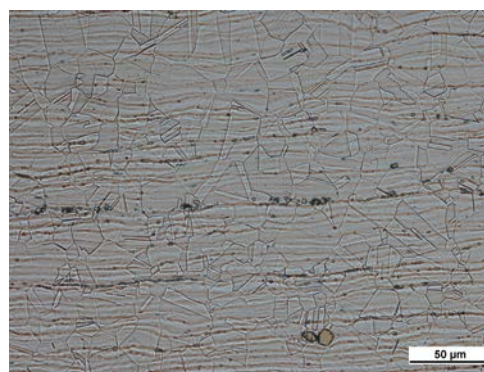
Fig. 1 Microstructure of AISI 316Ti stainless steel in longitudinal section (etch.10 cm^3 HNO_3 + 20 cm^3 H_3PO_4 + 30 cm^3 glycerin, for 5 minutes)

3. Experimental conditions and methods

1 M chloride solution was used as the basic corrosion environment for both immersion and potentiodynamic polarisation tests. 1 M chloride solution was represented by 5 % $FeCl_3$ (pH=1.2) for immersion tests and by 0.9 M NaCl + 0.1 M HCl (pH=1.1) for potentiodynamic tests. The basic solution was applied without inhibitor and with two concentrations of molybdate inhibitor: 0.05

M and 0.1 M (it means the concentration ratio inhibitive/aggressive anions 1:20 and 1:10 respectively).

Immersion tests

The specimen's shape for immersion tests was rectangular (30 mm x 80 mm x 1.5 mm). The specimen surface was not treated (mechanically or chemically) only the edges were grinded by abrasive paper grain 600. The grease was removed by diethyl ether. The specimens were weighted out with accuracy ± 0.000 01 g (Mettler Toledo XS 205). All immersion tests were 24 hours and they were carried out at ambient temperature 20 ± 3 °C [2, 9, 10]. The group of three parallel specimens was tested for each solution. After exposure the specimens were carefully brushed, washed by de-mineralized water, freely dried up and weighted out again.

Pitted surfaces of specimens after immersion tests were observed by the optical microscope NIKON AZ 100. Average corrosion rates ($g.m^{-2}.h^{-1}$) were calculated from corrosion losses ($g.m^{-2}$) during the immersion tests.

Potentiodynamic polarization tests

Potentiodynamic polarisation tests were carried out in a three electrode cell of corrosion measuring system (VoltaLab 10 with VSP unit). Potentiodynamic polarisation curves were obtained by the EC-LAB SOFT software. Potential between the sample and the electrolyte has been settled for 10 minutes before the polarization. Scan range was -0.3V – 0.9V vs the open circuit potential and the scan rate was 1mV/s. The surface of working electrode AISI 316Ti of 1 cm^2 area was not mechanically treated, only rinsed with diethyl ether before measurement. The saturated calomel electrode (SCE) was applied as the reference electrode and platinum foil as a counter electrode. All experiments were carried out at ambient temperature of 20 ± 3°C. At least five experiment repeats were carried out for all specimens.

4. Experimental results and discussion

Tested specimens were locally damaged by pitting during immersion tests (Fig. 2). The corrosion failure is localized non-uniformly. Pits seem to be situated into lines related with rolling. $(Mo, Cr)_{23}C_6$ carbides occur along this lines (Fig. 1) and they may affect negatively the quality of passive film in these places [11]. Local corrosion failure is also situated to the edges of specimens and to the holes for hanging with higher surface roughness (Fig. 2).
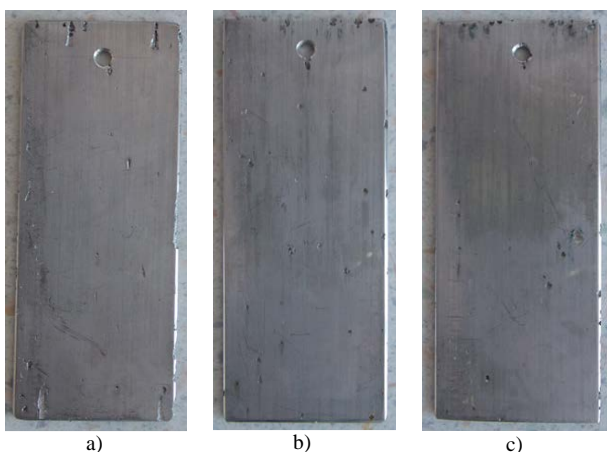
Fig. 2 *Pitted surfaces of tested specimens after 24-hours immersion test: a) without inhibitor, b) with 0,05 M molybdate, c) with 0,1M molybdate.*

As we can see in Fig. 2 a), the pits on the specimen immersed in 1 M chloride solution without inhibitor are oblong and generally bigger than pits in Figs. 2 b) and 2 c). The specimens immersed in solution with inhibitor have similar character of pitting – the shape of pits is rounder and specimens edges are less damaged than in case without inhibitor. The typical pit shapes and profiles are shown and can be compared in Fig. 3. This comparison confirms differences of pit shapes observed visually (Fig. 2). Molybdate ions

MoO_4^{2-} are considered an efficient oxidizing anodic inhibitor for pitting corrosion of stainless steels. The primary step of their action is the adsorption on the metal surface which enables to prevent the breakdown of surface passive film [6, 8]. Subsequently, Mo^{6+} (present in MoO_4^{2-}) is reduced to Mo^{4+} and MoO_2 is formed [6]. The adsorption of molybdate on the steel surface probably prevented growth of pits sideways and caused better bounded rounder pits. This phenomenon can be observed on the profiles of pits as well. As we can see, the molybdate inhibitor limited the width of pits, but it did not prevent their increase in depth.
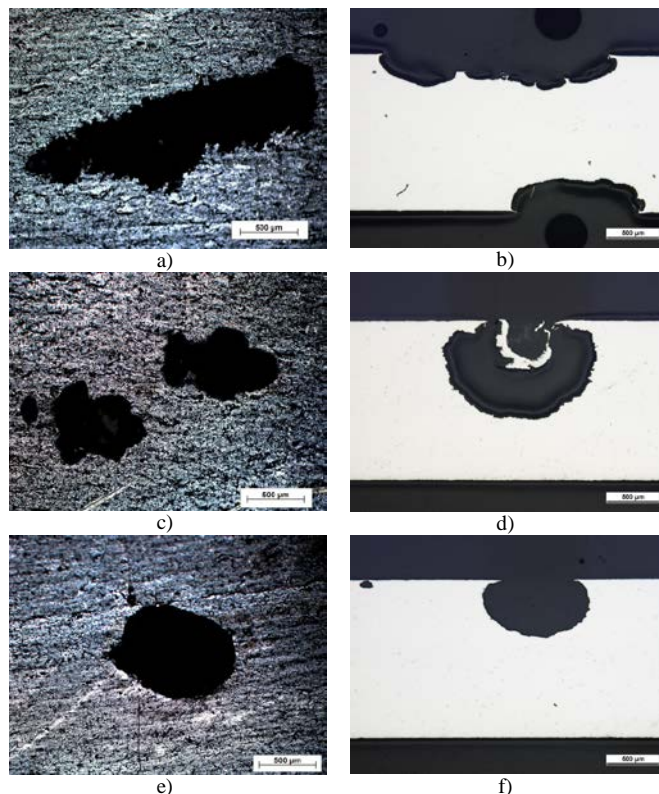
Fig. 3 *Typical shapes and profiles of pits after 24-hours immersion test: a), b) without inhibitor, c), d) with 0,05 M molybdate, e), f) with 0,1M molybdate.*

Average corrosion rates calculated from corrosion losses during the immersion tests in dependence on the molybdate concentration are shown in Fig. 4. Obviously, the average corrosion rate decreases with the increase of inhibitor concentration. However the corrosion rate based on the corrosion loss cannot be generally considered as the essential factor of evaluation of pitting corrosion resistance because of non-uniform, local character of pitting. However, it helps make an idea about probable changes in the pitting corrosion kinetics [2, 9].
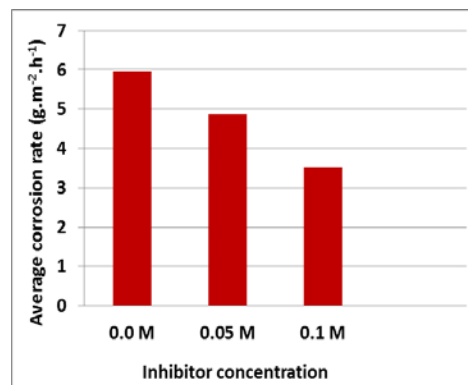
Fig. 4 *Average corrosion rates in dependence on inhibitor concentration*

Potentiodynamic polarisation curves enable determination of the pitting potential (E_p), which is an important electrochemical characteristic of the resistance to pitting. When the potential reaches

this critical value, current density suddenly increases, denoting the breakdown of the passive film and the beginning of stable pit growth. The shift of E_p to more positive values on the polarisation curve means the rise of stability to pitting [1, 2, 9, 10].

Potentiodynamic polarisation curves of AISI 316Ti stainless steel in 1 M Cl⁻ solution in the absence and presence of molybdate inhibitor (0.05 M and 0.1 M additions) are shown in Fig. 5. Pitting potentials in dependence on inhibitor concentration are compared in Fig. 6. The higher inhibitor concentration (0.1 M) caused the extension of the passive region and the shift of E_p to higher positive potential values. According to curve 2 the lower inhibitor concentration (0.05 M) was not sufficient to improve the resistance to stable pitting in comparison with the case without inhibitor (E_p is only slightly higher, Fig. 6).
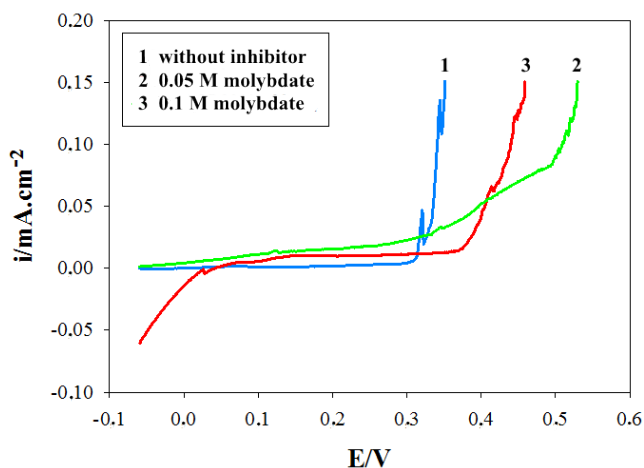
Fig. 5 *Anodic potentiodynamic curves for AISI 316Ti working electrode in 1 M Cl⁻ solution: 1 without inhibitor, 2 with 0.05 M molybdate, 3 with 0.1 M molybdate*
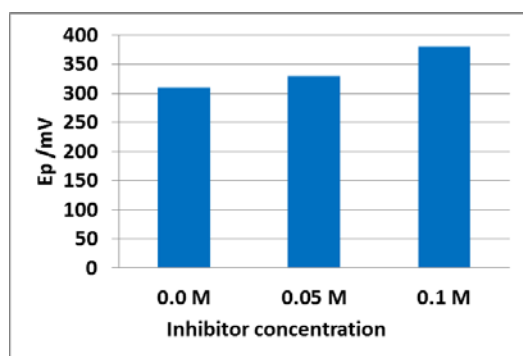
Fig. 6 *Comparison of the pitting potentials (E_p) in dependence on concentration of molybdate inhibitor in 1 M chloride solutions*

Moreover, a passive current density in presence of 0.05 M molybdate is rather high and it points to lower stability of passive stage in this case.

5. Conclusion

Presence of molybdate inhibitor in 1 M chloride solution (represented by 5 % FeCl₃ solution) did not prevent a local pitting corrosion of tested steel during 24 hours immersion test. The inhibitor used positively affected the shape of pits (the pits became rounder and better bounded) but it did not prevent their increase in depth. The appearance of pitting seemed to be influenced only by the presence of inhibitor, not by its higher or lower concentration (0.1 M and 0.05 M).

Performed potentiodynamic polarisation tests showed a marked shift of the pitting potential E_p to higher positive values in the case of 0.1 M concentration of inhibitor and it points to higher resistance

to pitting. However, this result does not correlate clearly with results of performed immersion test.

In spite of some partial positive results (results of potentiodynamic polarisation test), a use of the molybdate inhibitor does not seem to be a reliable means which would prevent a local corrosion of AISI 316Ti stainless steel in 1 M chloride acidic solution.

References

1. SZKLARSKA-SMIALOVSKA, Z. *Pitting and crevice corrosion.* Houston, Nace, 590 p., (2005).
2. LIPTÁKOVÁ, T. *Bodová korózia nehrdzavejúcich ocelí. (Pitting corrosion of stainless steels.)* Žilina, EDIS – Žilinská univerzita, 67 p., (2009).
3. ČÍHAL, V. *Korozivzdorné oceli a slitiny.(Stainless steels and alloys.)* Praha, Academia, 437 p., (1999).
4. EBRAHIMI, N., MOAYED, M. H., DAVOODI, A. *Critical pitting temperature dependence of 2205 duplex stainless steel on dichromate ion concentration in chloride medium.* Corrosion Science, vol. 53, pp. 1278-1287, (2011).
5. EL DAHAN, H. A. *Pitting corrosion inhibition of 316 stainless steel in phosphoric acid-chloride solutions.* Journal of Materials Science, vol. 34, pp. 851-857, (1999).
6. ILEVBARE, G. O., BURSTEIN, G. T. *The inhibion of pitting corrosion of stainless steels by chromate and molybdate ions.* Corrosion Science, vol. 45, pp. 1545-1569, (2003).
7. ZUO, Y., WANG, H., ZHAO, J., XIONG, J. *The effects of some anions on metastase pitting of AISI 316L stainless steel.* Corrosion Science, vol. 44, pp. 13-24, (2002).
8. REFAEY, S. A. M., ABD EL-REHIM, S. S., TAHA, F., SALEH, M. B. AHMED, R. A. *Inhibition of chloride localized corrosion of mild steel by PO_4^{3-}, CrO_4^{2-}, MoO_4^{2-}, and NO_2^- anions.* Applied Surface Science, vol. 158, pp. 190–196, (2000).
9. ZATKALÍKOVÁ, V. *Bodová korózia ocele AISI 316Ti pri rôznych prevádzkových podmienkach.* (*Pitting corrosion of AISI 316Ti at various operating conditions.*) PhD Thesis: ŽU v Žiline, Žilina, p. 77, (2008).
10. BABOIAN, R. *Corrosion Test and Standards: Aplication and Interpretation*, *ASTM Manual Series.* Philadelphia, USA, PA 19103, (1995).
11. PARDO, A., MERINO, M. C., COY, A. E., VIEJO, F., CARBONERAS, M., ARRABAL, R. *Influence of Ti, C and N concentration on the intergranular corrosion behavior of AISI 316Ti and 321 stainless steels.* Acta Materialia, vol. 55, pp. 2239-2251, (2007).

STRUCTURAL, ELASTIC AND ELECTRONIC PROPERTIES OF Cu_2MnZ(Z=Al, Ga, In, Si, Ge, Sn, Sb): A FIRST-PRINCIPLES STUDY

Assoc. Prof. Dr. Uğur Ş.[1], M.Sc. Ulusu E.[1],

Faculty of Science,Department of Physics, Gazi University 06500, Teknikokullar, Ankara, Turkey [1]

suleugur@gazi.edu.tr

Abstract: *The structural, elastic, electronic and phonon properties of Cu_2MnZ(Z=Al, Si, Ge, Ga, Sn, Sb, In) are investigated by first-principles calculations based on density functional theory. In this approach the local-density approximation (LDA) and generalized gradient approximation (GGA) are used for the exchange-correlation (XC) potential. The calculated lattice constant, bulk modulus, and elastic constants are in agreement with the previous ab-initio calculations and available experimental results. Electronic properties are discussed from the calculations of band structure and density of states. The direct method is used to derive the phonon frequencies and density of states.*

Keywords: HEUSLER ALLOY, ELECTRONIC BAND STRUCTURE, ELASTIC CONSTANTS, PHONON

1. Introduction

Heusler alloys have received much study due to their potential as key materials for spintronic devices [1-5]. Heusler compounds belong to a group of ternary intermetallics with the stoichiometric composition, X_2YZ, ordered in $L2_1$-type structure (space group Fm-3m) and many of these compounds are ferromagnetic. Full-Heusler alloys X_2YZ crystallize in the $L2_1$ structure. The unit cell consists of four interpenetrating fcc sublattices with the positions (0,0,0) and (0.5,0.5,0.5) for X, (0.25,0.25,0.25) for Y and (0.75,0.75,0.75) for Z atom. For Cu_2MnAl, the electronic, optical, elastic and magnetic properties were studied by Rai et al. [6] using the full potential linearized augmented plane wave method with the generalized gradient approximation (FPLAPW-GGA). They found that Cu_2MnAl is a ferromagnet metallic compound. In this work, we have aimed at to provide some additional information to the exhibit data on the structural, elastic, electronic and phonon properties of Cu_2MnZ(Z=Al, Ga, In, Si, Ge, Sn, Sb) alloys. The full phonon-dispersion curves are necessary for a microscopic understanding of the lattice dynamics. Knowledge of the phonon spectrum plays a significant role in determining various material properties, such as phase transition, thermodynamic stability, transport and thermal properties.

2. Computational Methods

The calculations were performed within the density functional theory, as implemented in the MedeA-Vasp package [7, 8]. In order to ensure the reliability of the calculations, the total energy and lattice parameter of Cu_2MnZ(Z=Al, Si, Ge, Ga, Sn, Sb, In) alloys were calculated with respect to plane wave cutoff energy E_{cut} and k-point sampling. The optimization of the structural parameters is performed until the forces on the atoms are less than 0.02 eV/Å. The elastic properties (G, E) were calculated from the Hill value, which is a geometric mean of the Voigt and Reuss values [9]. The phonon dispersion curves of the considered materials have been calculated through the direct method [10], in which the forces are calculated via the Hellmann-Feynman (HF) theorem.

3. Results and Discussion

In Table 1, we summarize our calculated convergence parameters (E_{cut} and k-point), equilibrium lattice constant (a_0) Bulk modulus (B) and total magnetic moments (Mt) of Cu_2MnZ(Z=Al, Si, Ge, Ga, Sn, Sb, In) compared with the available data in the literature. There is a good agreement between our results and that previously reported [6].

Table 1: *Calculated convergence parameters (Ecut, k-point), lattice constants (a_o), Bulk modulus (B) and total magnetic moments (Mt) for Cu_2MnZ(Z=Al, Si, Ge, Ga, Sn, Sb, In) alloys.*

		E_{cut} (eV)	k-point	a_0 (Å)	B (GPa)	M_t (μB)
GGA-PBE	Cu_2MnAl	376,696	7x7x7	5,928606 / 5,957[6]	124,24 / 115,64 [6]	3,5764 / 3,568 [6]
	Cu_2MnSi	344,196	8x8x8	5,864956	133,60	3,7303
	Cu_2MnGe	395,823	9x9x9	6,005586	114,80	3,9944
	Cu_2MnGa	344,196	5x5x5	5,956234	121,19	3,6176
	Cu_2MnSn	360,446	7x7x7	6,233775	101,31	3,8685
	Cu_2MnSb	360,537	6x6x6	6,313866	96,50	3,9057
	Cu_2MnIn	344,196	6x6x6	6,202166	106,96	3,7879
LDA	Cu_2MnAl	376,696	6x6x6	5,755385	153,49	3,2020
	$Cu_2Mn Si$	340,446	7x7x7	5,677539	170,76	3,3961
	Cu_2MnGe	361,492	6x6x6	5,815464	147,32	3,6596
	Cu_2MnGa	360,446	6x6x6	5,761216	164,45	3,3771
	Cu_2MnSn	344,196	7x7x7	6,038436	139,36	3,6249
	Cu_2MnSb	360,446	6x6x6	6,102149	125,51	3,6367
	Cu_2MnIn	360,537	5x5x5	6,002546	139,22	3,5131

Table 2: *The calculated elastic constants Cij (in GPa), shear moduli (in GPa) and Young's modulus (in GPa).*

		C_{11}	C_{12}	C_{44}	G	E
GGA-PBE	Cu_2MnAl	137.2 / 137.68 [6]	117.75 / 104.614 [6]	105.28 / 460.41 [6]	67.06 / 116.04 [6]	170.50
	Cu_2MnSi	128.33	136.24	89.43	52.08	138.27
	Cu_2MnGe	110.64	116.88	65.72	38.18	103.12
	Cu_2MnGa	124.49	119.55	90.00	54.99	143.30
	Cu_2MnSn	105.93	99.00	64.75	40.24	106.60
	Cu_2MnSb	80.38	104.56	29.27	12.73	36.58
	Cu_2MnIn	114.45	103.22	78.26	49.20	127.98
LDA	Cu_2MnAl	170.13	145.17	129.76	82.85	210.65
	$Cu_2Mn Si$	162.48	174.90	105.41	60.76	162.95
	Cu_2MnGe	137.52	152.22	85.38	48.29	130.59
	Cu_2MnGa	169.35	162.01	117.77	72.13	188.79
	Cu_2MnSn	142.35	137.86	83.84	51.20	136.85
	Cu_2MnSb	103.65	136.43	46.87	21.56	61.18
	Cu_2MnIn	149.53	134.06	100.69	63.51	165.38

The elastic constants require knowledge of the derivative of the energy as a function of lattice strain. In the case of cubic system, there are only three independent elastic constants, namely, C_{11}, C_{12} and C_{44}. The well-known Born stability criteria are a set of conditions on the elastic constants (C_{ij}) that are related to the second-order change in the internal energy of a crystal under deformation. Cu_2MnZ(Z=Al, Ga, Sn, In) all fulfill the stability criteria, while the unstable Cu_2MnZ(Z= Si, Ge, Sb) fails to satisfy the Born criterion.

The electronic structure plays an important role in determining
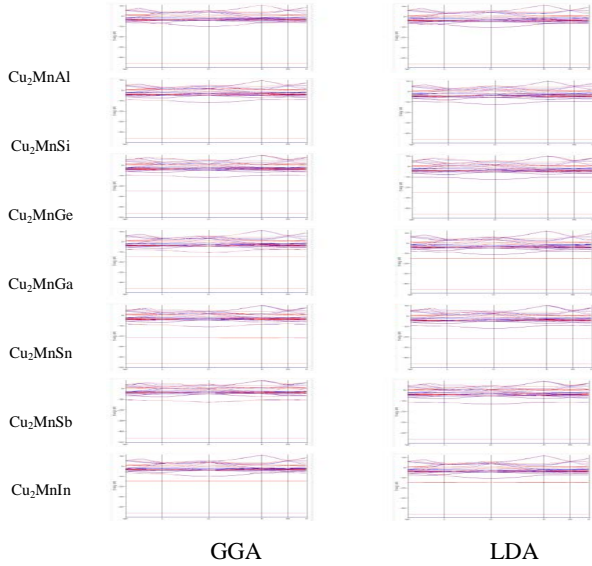
Fig. 1 *The spin resolved electronic band structure of Cu_2MnZ(Z=Al, Si, Ge, Ga, Sn, Sb, In). Solid red and blue lines are corresponding to spin up and down states, respectively.*

the magnetic properties of Heusler compounds. Fig. 1 shows the electronic structure of the Cu_2MnZ(Z=Al, Si, Ge, Ga, Sn, Sb, In). Band structure calculations, which were performed using various methods (GGA, LDA) show almost the same shape. There is no gap between the two spin density of states at the Fermi level, meaning that it exhibits a typical metallic nature.

Fig. 2 shows the phonon dispersion curves along the high-
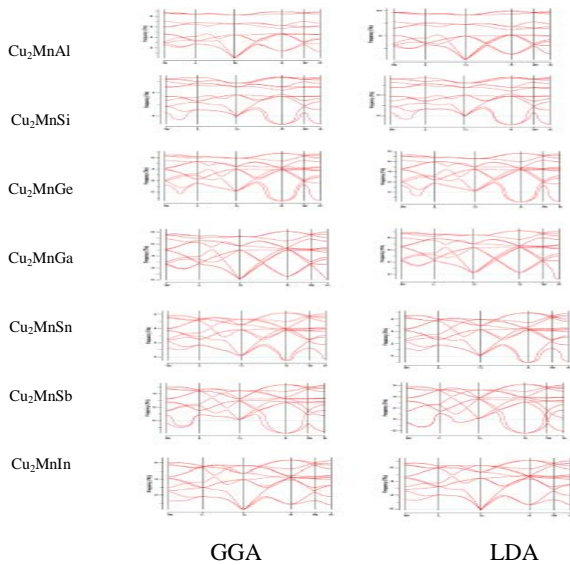
Fig. 2 *Calculated phonon dispersions of Cu_2MnZ(Z=Al, Si, Ge, Ga, Sn, Sb, In).*

symmetry directions for Cu_2MnZ(Z=Al, Si, Ge, Ga, Sn, Sb, In). The calculated phonon dispersion curves of Cu_2MnAl and Cu_2MnIn confirm that these two compounds are dynamically stable in the $L2_1$-type structure without any imaginary phonon frequencies.

4. Conclusion

Structural, elastic, electronic and phonon properties for a series of Cu containing bulk Heusler alloys Cu_2MnZ(Z=Al, Si, Ge, Ga, Sn, Sb, In) were investigated by first-principles investigations. The lattice constant has been calculated using two different methods GGA and LDA and gave excellent agreement with others. The band structure for the Cu_2MnZ(Z=Al, Si, Ge, Ga, Sn, Sb, In) alloys were analysed and compared. The phonon properties of Cu_2MnZ(Z=Al, Si, Ge, Ga, Sn, Sb, In) were studied in the direct method.

References

[1] Fang C. M., Wijs G. A. de and Groot R. A. de, J. Appl. Phys., 91 (2002) 8340.

[2] Wolf S. A., Awschalom D. D., Buhrman R. A., Daughton J. Molnar M., S. von, Roukes M. L., Chtchelkanova A. Y. and Treger D. M., Science, 294 (2001) 1488.

[3] Otto M. J., Feil H., Bruggen R. A. van and Haas C., J. Magn. Magn. Mater., 70 (1987) 33.

[4] Groot R. A. de, Mueller F. M., Engen P. G. van, and Buschow K. H., Phys. Rev. Lett., 50 (1983) 2024.

[5] Kobayashi K., Umetsu R.Y., Fujita A., Oikawa K., Kainuma R., Fukamichi K. and Ishida K., Journal of Alloys and Compounds, 399 (2005) 60.

[6] Rai D.P. and Thapa R.K., Journal of Alloys and Compounds, 612 (2014) 355.

[7] Kresse G. and Hafner J., Phys. Rev. B, 47 (1993) 558.

[8] Kresse G. and Furthmuller J., Phys. Rev. B, 54 (1993) 1169.

[9] Anderson O.L., J. Phys. Chem. Solids 24 (1963) 909.

[10] Parlinski K., Li Z. Q. and Kawazoe Y., Phys. Rev. Lett., 78 (1997) 4063.

INVESTIGATION OF EFFECT OF TEXTURE ON COLD RESISTANCE OF NEW GENERATION STEELS FOR BUILDING STRUCTURES

ИССЛЕДОВАНИЕ ВЛИЯНИЯ ТЕКСТУРЫ НА ХЛАДОСТОЙКОСТЬ СТАЛЕЙ НОВОГО ПОКОЛЕНИЯ ДЛЯ СТРОИТЕЛЬНЫХ КОНСТРУКЦИЙ

Sen. Sc., PhD Arsenkin A.M.[1] , Res. Eng. M.V. Zheleznyi [1,2], Prof., Dr Sc. Odesskiy P.D.[3], PhD, Ass. Prof. I.V. Schetinin[2],

PhD, Ass. Prof. M.V. Gorshenkov[2], Prof., Dr Sc. Vedyakov I.I.[3]

A.A. Baikov Institute of Metallurgy and Materials Science of Russian Academy of Sciences[1]

National university of science and technology "MIS&S"[2]

V.A. Kucherenko Central Research Institute of Building Structures of JSC «Research Center «Building»[3],

E-mail: tsniisk@rambler.ru, odesskiy@tsniisk.ru, x25xe@mail.ru, alex_arsenkin@yahoo.com

Abstract:

Due to technological particularities of low carbon low alloy API 5L X80 steels producing they have strong texture and its inhomogeneity on plate thickness. Charpy impact tests at ambient and negative temperatures and investigation of texture of samples of API 5L X80 steel were performed. By the method of X-ray structural analysis DPF, IPF and ODF were obtained. Texture components and their volume fraction were determined. It was shown that correlation between volume fractions of main texture components, misoriented grains fraction and DBTT exists. As a result analysis of texture parameters allowed characterization of effect of texture on cold resistance of low carbon low alloy API 5L X80 steel.

KEY WORDS: LOW CARBON MICROALLOYED API 5L X80 PIPE STEELS, TEXTURE, MICROSTRUCTURE, IMPACT TOUGHNESS, COLD RESISTANCE.

1. Introduction

At present, the API 5L X80 grade pipe steels are widely used for building structures, thereby reducing the metal and energy consumption [1-3]. This is associated with a unique set of mechanical and processing properties of low carbon microalloyed steels: combination of high strength, plasticity, ductility, weldability, seismic resistance, and fire resistance [4, 5]. Typically building construction units made of sheet >25 mm in thickness are used. In such thick sheets strong structural inhomogeneity can be formed, induced by chemical inhomogeneity, nonuniformity of deformation and temperature over sheet sequence in the rolling process and heat treatment. This structural inhomogeneity leads to inhomogeneity of mechanical properties and anisotropy [6]. One of the factors that affect the mechanical properties and cold resistance of these steels is the texture formed during rolling and transformation [7]. It is believed that the formation of austenite deformation texture components {110} <1-12> leads to the formation of the ferrite texture {332} <113>, which is preferred for achieving high strength and toughness. Austenite recrystallization causes the formation of the texture component {100} <001>, which transforms into the ferrite texture {100} <011>, that is highly

undesirable, since it coincides with the cleavage plane of the ferrite [8]. The problem of the impact of a texture on cold resistance and fracture of steels is not still clear. For example, in [9] it was found that the increasing of volume fraction of the {001} <110> components is accompanied by the decrease of DBTT. So this work is devoted to determination of the role of texture in cold resistance of the API 5L X80 grade pipe steels.

2. Preconditions and means for resolving the problem

2.1 Material and procedures

The materials under the study represented *API* 5L X80 low carbon low alloy steels after thermo-mechanical processing, produced in manufacturing conditions. The chemical compositions of the steels are presented in Table 1. The mechanical properties of the steels are given in Table 2. The samples under the study were cut from pipes of 1420 mm in diameter and 27,7 (steels #1, 3, Table 1) and 33,4 mm (steel #2, Table 1) in wall thickness.

Table 1 – Chemical composition of the steels under the study

#	C	Si	Mn	Ni	P	S	Cu	Cr	Al	V	Mo	Ti	W	Nb	N
1	0,071	0,240	1,76	0,248	0,007	0,006	0,036	0,084	0,027	0,021	0,244	0,020	0,030	0,059	0.0033
2	0,067	0,275	1,67	0,235	0,010	0,005	0,047	0,077	0,024	0,023	0,254	0,024	0,022	0,074	0.0041
3	0,073	0,252	1,58	0,241	0,007	0,005	0,151	0,220	0,037	0,018	0,195	0,015	0,020	0,080	0.0029

Table 2 – Mechanical properties of studied steels

#	$\sigma_{0,2}$, MPa	σ_b, MPa	$\sigma_{0,2}/\sigma_b$	δ_5,%	ψ,%
1	567	672	0,83	20	68
2	617	690	0,89	17	72
3	570	675	0,84	20	70

Samples for impact bending tests were cut at a depth of 2 mm from the pipe surface, and the notch was oriented perpendicularly to the rolling direction. To study the effect of structural nonuniformity over the sheet thickness on cold resistance, the samples were also cut from the central region of the pipe wall of the steel #2. Standard V-notch samples of 10x10x55 mm in size were tested with instrumented impact test machine Roell Amsler RKP-450 (Zwick / Roell) at temperatures of +20, -20, -40, -60, -80, -105, -120, -160, and -196°C. The experimental temperature dependence of toughness was approximated by the function $F(T) = A+B*\tanh(T-T_0)/C$, where A and B are the half-sum and half-difference of the levels of the upper and lower shelves of serial curves, respectively, $F(T_0) = A$, and the C parameter was determined graphically [21]. The ductile-brittle transition temperature (DBTT) was taken as T_0. The texture of the samples was examined with a Rigaku ULTIMA IV X-ray diffractometer. With usage of MoKα radiation by the divergent beam method inverse pole figures (IPF) were obtained and by the parallel beam method in CoKα radiation direct pole figures (DPF) were plotted. For each sample, the XRD patterns were taken from two planes parallel to the rolling plane and located at a depth of 2 mm from the surface and at center of the pipe wall thickness. With help of software ToolBox MTEX 4.0 from DPF orientation distribution functions (ODF) were calculated, volume fractions of main texture components and misoriented constituent were determined.

2.2 Results and discussion

As a results of Charpy impact tests values of ductile brittle transition temperature for the steels were determined. Steel #3 had maximal DBTT value. Minimal DBTT value was determined for steel #2 (table 3).

Table 3 – DBTT values for the steels under the study

#	DBTT, °C
1	-88
2	-86
3	-101

The comparison of the DBTT values of the samples cut from the center and near the surface of the pipe wall (by the example of steel #2) showed that the DBTT of the surface layers of the pipe wall was below by >30 degrees than that of the central part of the pipe wall (Table 4).

Table 4 – DBTT values of steel samples cut from the center and near the surface of the pipe wall

Sample	DBTT, °C
Pipe wall edge	-86
Pipe wall mid-thickness	-52

Thus plates for pipe production possess strong inhomogeneity of ductility over plate cross section. Because of deformation and cooling nonuniformity over the plate thickness, the texture also differ at different distances from the rolling surface [29]. Analysis of the results showed that texture in studied steels contained two main components (100) and (211). In all the samples, there is a pronounced texture component (100), due to the austenite recrystallization texture. The study showed heterogeneity of texture components over pipe wall thickness. Comparison of obtained DPF showed their strong difference near the surface and in the center of pipe wall.

a) b) c)

d) e) f)

g) h) e)
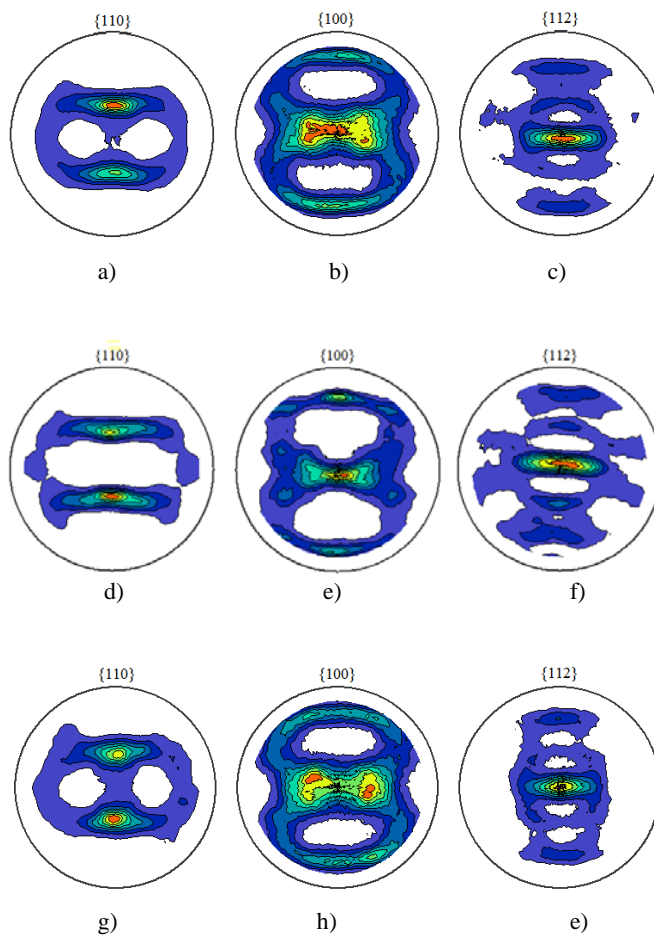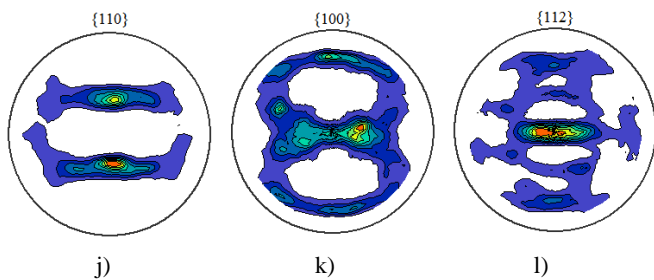
Figure 1 - DPF obtained from steel #1 and #3 for the edge of pipe wall (a,b,c, g, h, e) and the center (d,e,f, j,k,l) respectively

It should be noticed that there is main difference in DPF {100} of center and edge of pipe wall. As it is seen from fig. 1 a, d, g, j pronounced texture components were {112}(110) and {111}(112). Investigation of ODF for the steels under the study showed that edge of pipe wall contained as known misoriented constituent (fig.2). It should be reminded that it is just pipe wall edge has lower DBTT.
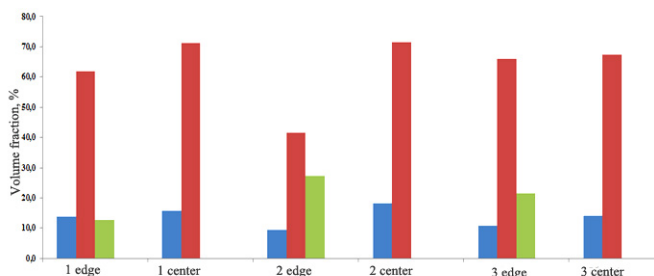
Figure 2 – Volume fractions of texture component {100}- sum of components {112}<001>, {111}<110>, {111}<112>, {011}<011>, {332}<113>, {113} <011> and misoriented constituent

Also steel having lower DBTT possesses maximal sum of total component and misoriented constituent. Analysis IPF showed that growth of DBTT was accompanied by increasing of pole density of {100} component and decreasing of {112} texture component.

3. Conclusion

The study showed that the plates for pipe production possess strong inhomogeneity of ductility and texture over the plate thickness.

Steels having a low DBTT value were characterized by low pole density of texture components (100) and increased pole density of orientation (211). Also steel with high cold resistance (low DBTT) has maximal sum of total component and misoriented constituent.

4. Literature

1. F.C. Feher, A.K. De and M. Manohar: Value-added Nb microalloyed construction steels. Symp. Proc. Singapure, 2012, pp. 45-54.

2. L.M. Silvestre, R.J. Pimenta, M.A. Stuart Nogueira et al.: Value-added Nb microalloyed construction steels symp. Proc. Singapure, 2012, pp. 89-102.

3. M. King, W. Whitby, G.Hanshaw: Value-added Nb microalloyed construction steels symp. Proc. Singapure, 2012, pp. 3-40.

4. K.S. Sivakumaran: Value-added Nb microalloyed construction steels symp. Proc. Singapure, 2012, pp. 103-114.

5. J.G. Speer, D.K. Matlock, S.G. Jansto: Value-added Nb microalloyed construction steels symp. Proc. Singapure, 2012, pp. 115-131.

6. P.K.C. Venkatsurya, R.D.K. Misra, M.D. Mulholland, M. Manohar and J.E. Hartman: Metall. Mater. Trans. A, 2014, vol. 45A, pp.2335-42.

7. G. Krauss: Steels Processing Structure and Performance, ASM International Materials Park, Ohio, 2005, pp 230-32.

8. H. K. D. H Bhadeshia: Bainite in steels. Transformations, microstructures and properties, IOM Communications Ltd., London, 2001, pp. 348-358.

9. V.M. Schastlivtsev, T.I. Tabatchikova, I.L. Yakovleva, L.Y. Egorova, I.V. Gervas'eva, A.A. Kruglova, E.I. Khlusova, V.V. Orlov: The Physics of Metals and Metallography, 2010, vol.109, No.3, pp.289-299.

RELATIONSHIP BETWEEN PARAMETERS OF TEMPERING AND EDDY CURRENT TESTING OF CARBURIZED PARTS

ВРЪЗКА МЕЖДУ ПАРАМЕТРИТЕ НА ОТВРЪЩАНЕ И ВИХРОВОТОКОВОТО ИЗПИТВАНЕ НА НАВЪГЛЕРОДЕНИ ДЕТАЙЛИ

СВЯЗЬ ПАРАМЕТРОВ ОТПУСКА И ВИХРЕТОКОВОГО ИССЛЕДОВАНИЯ НАУГЛЕРОЖЕННЫХ ДЕТАЛЕЙ

Ivanov J. St., MSc
"M+S Hydraulic" AD, Kazanlak, Bulgaria
E-mail: jeanivanov@yahoo.de

Abstract: *The process of low-temperature tempering has been studied by eddy current testing and measuring the hardness HRC at a constant temperature as well as at increasing temperature and duration. Technological factors of tempering were considered in their interdependence, according to the Hollomon-Jaffe equation. It has been argued that the factor levels, temperature and duration, are determined by the carburization and quenching results. Eddy current testing has been introduced as an indicator of quality with high sensitivity to changing technological factors; it has integral importance in terms of structural changes and electromagnetic properties of the parts. Hardness and electromagnetic characteristics, as indicators of quality after low-temperature tempering, were presented as a function of the tempering parameter Pa.*

Keywords: EDDY CURRENTS, LOW-TEMPERATURE TEMPERING, CARBURIZING, QUENCHING, HOLLOMON-JAFFE

1. Introduction

The tempering of carburized and quenched parts is the obligatory final stage of the technology of the thermochemical treatment. During this stage the purpose is to reduce the effects of quenching which reduce the potential for exploitation or subsequent treatment of parts, as well as to achieve different combinations of useful levels of the mechanical properties. After quenching, the properties achieved at room temperature change when the temperature rises and after various durations of heat treatment they try to achieve equilibrium. During this stage, called tempering, all changes which occur in the parts are related to diffusion processes. The latter are activated thermally and involve the dislocation of alloying elements, carbon, and impurities in the steel parts. The 150-250^{0}C levels define the basic characteristic of low-temperature tempering. Having in mind the stronger effect of temperature on the results of tempering [7] the main classification of the process is based on limiting discrete values of that technological factor. The limits of the other technological factor, i.e the duration of the process, are not so clearly defined. The usual technological solution is the application of isothermal and isochronal diagrams of tempering [12]. It is not difficult to predict that like every other search for equilibrium, with occurring diffusion processes [1], tempering would lead to different levels of mechanical properties depending on its duration. One should not underestimate the phase difference, grain size and the presence of defects, connected with carburising and quenching processes. That is the reason why this paper looks for arguments in favour of the statement that the technological factors, temperature and duration of tempering, should not be considered constant or fixed values, but they should change dynamically depending on the results of the previous processes of thermochemical treatment. On the other hand, the control of the tempering results control presents another challenge due to the nature of hardness measurements, the extent of this control, and the thickness of the layer, where changes are measured. Typically, when this zone is measured according to the Rockwell scale C, it does not exceed 0.1 mm, but it is there and also in depths up to 0.3 mm that carburized layers develop the main flaws.

2. Elements of the tempering theory

The process of low-temperature tempering causes the transformation of tetragonal martensite into cubic martensite [4, 5, 6, 7, 8] and the formation of hexagonal ε-carbides Fe2,4 C 10-20 mm in size [7]. Apart from carbides and martensite, the structure retains different quantities of residual (paramagnetic) austenite as the temperature of the end martensite transformation drops below 0^0C [7]. With the quantity of carbon gradually diminishing, martensite reacts differently to temperature treatment by decreasing its tetragonality and tension. If the layer structure consists of martensite alone, it might be possible to register unequivocal changes after the tempering process. The layered structure with a gradual transition to the steel core, and the possible presence of characteristic sub-layers, such as:
- Surface oxidation layer;
- Carbides and troostite layer;
- Residual austenite layer;
- Martensite layer,
results in complications and uncertainty in the final grading of parts which have been gas carburized [2,10]. Steel improvement tempering seems a far better studied process; one of its characteristic features is the mutual relationship between the technological factors, temperature and time, a relationship called "tempering parameter" by Hollomon-Jaffe [1, 2, 3, 11]:

$$(1) \quad Pa = T.(a + log\ \tau)$$

Where:
Pa is the tempering parameter;
T is the temperature in Kelvin degrees;
τ is the tempering time in seconds [7] or hours [1,2,3];
a is a constant which for most steels is equal to 20 [2,3].

There is too little information on the usage of this correlation in the control of low-temperature tempering of carburized and quenched parts [7]. The value of the constant a depends on the type of steel and the rate of heating and cooling of parts, i.e. it depends on their size and shape, too. That is why the value of the a constant has to be determined by a number of research teams. For steels meant for

carburization, the a constant has been determined to be equal to 15-17 [7].

The $\mathbf{Pa}$ parameter is in direct correlation with hardness. For example, for improvable steels, one hour is needed in order to achieve the same hardness at 400°C, while at 390°C, the time increases twice. For many steels the hardness-tempering parameter relation is presented graphically in the tempering diagrams [2]. The complete tempering diagram must contain data about the effect of the degree of hardening $\mathbf{Rh}$ and the tempering parameter $\mathbf{Pa}$, on hardness and toughness. $\mathbf{Rh}$ is the correlation between the desired value of hardness and the maximum value of hardness [1, 2]. The tempering parameter allows for different combinations of factors $\mathbf{T}$ and $\boldsymbol{\tau}$, which will result in the same hardness, and according to many researchers, also in relative similarity of the rest of the mechanical properties [7, 8, 10]. Such tempering modes are called isoscleric [8]. This premise is at the basis of many cost-effective tempering processes. It is also desirable, in case embrittlement develops during tempering, that the desired hardness be achieved in a short time and maximum high temperatures [11].

Unlike improvable steels, carburized and hardened steels pose too many complications, connected both with quenching results, and their behavior during tempering. They experience the influence of quite a few of the major factors in carburizing, the process kinetics, carbon activity, and many others. Although the Hollomon-Jaffe correlation requires the availability of quite a lot of empirical information, it makes it possible to estimate the expected hardness quite accurately in a number of computer controlled gas carburizing units [7].

The other significant difference from improvable steels lies in the method of tempering results control, where if hardness penetration is sufficient, HRC, HV10, and HV30 hardness measurements offer good grade reliability. This, however, does not apply to hardness measurements of carburized and quenched parts [11]. A number of factors make the results for measured hardness uncertain. Among them are the presence of defective layers, sub-layers with increased contents of retained austenite, low-depth carburizing, the measured surface class or type, etc. These make it necessary to find an additional quality criterion. The metallographic control of low-temperature tempering is practically very hard to achieve [2, 4, 9]. In the search of a method which could register the changes in carburized layers of different thickness, eddy current testing offers a wide range of capabilities. According to the theory of eddy currents, the latter react to changes in the inside tensions, the change in electro-magnetic properties of separate phases and conglomerate structures, and depending on the excitation frequency, they derive information from layers of different depth, etc.[15, 16]. The high sensitivity of eddy current testing to tempering conditions has been studied many times and has been well proven by a great number of planned experiments[13, 14].

3. Object and methodology of the research

4 20CrMo5, BDS EN 10084 steel shafts have been studied. The parts were tested with eddy currents at different duration of tempering, at 225°C. Another 4 shafts of the same steel were tested at increasing duration and incremental temperature change. In the second group testing, apart from the electromagnetic property Z, [17], HRC hardness [18] was measured as well. The data was processed by means of statistical processing software [19].

4. Objectives of research

The objective of eddy current testing research is to find a criterion for the levels of tempering processes, "degree of tempering", so that this criterion could become an indicator of the quality of the thermochemical treatment.
The research also aims to collect data on the behavior of parts during tempering and present the data in relation to the tempering

parameter $\mathbf{Pa}$, so that this would become a prerequisite for optimizing and creating a cost-effective process of low-temperature tempering, and eddy current testing would be used as a quick and comfortable means of control.

5. Results of the experiment

5.1 Isothermal tempering: temperature 225°C and increasing duration of up to 6 hours

Table 1 and Figure 1 display the results of the eddy current testing of 4 threaded conical output shafts.
Table 1 contains the following designations:

$$\{Z_i \equiv Z(i) = R(i) + X_L(i); i = 1,2,3,4\}$$

{R (i) ; i = 1, 2, 3, 4} – active resistance
{X_L (i) ; i = 1, 2, 3, 4}- inductive reactance
The values {R} and {X_L} are displayed by Eddy Current Tester MIZ 21B after the necessary calibration has been done.

Table 1 *Variations in the electromagnetic property {Zi;i= 1, 2, 3, 4} for the i shaft in relation to the tempering duration τ at 225°C.*

Time - h	Z_1-shaft 1	Z_2-shaft 2	Z_3-shaft 3	Z_4-shaft 4	Z-mean	Z-calculated
1	2	3	4	5	6	**7**
0	1,43	1,25	0,13	0,75	0,89	**0,45**
0,33	3	2,25	0,63	1,68	1,89	**1,67**
0,66	3,1	2,08	1,13	2,45	2,19	**2,27**
0,99	3	3,13	2	2,08	2,55	**2,71**
1,99	3,9	3,88	2,63	2,75	3,29	**3,68**
2,99	4,5	3,7	3,63	3,5	3,83	**4,40**
3,99	6,03	5,48	4,98	5,23	5,43	**5,00**
4,99	6,39	5,84	6,14	6,07	6,11	**5,51**
5,99	6,33	6,18	6,28	6,07	6,22	**5,98**
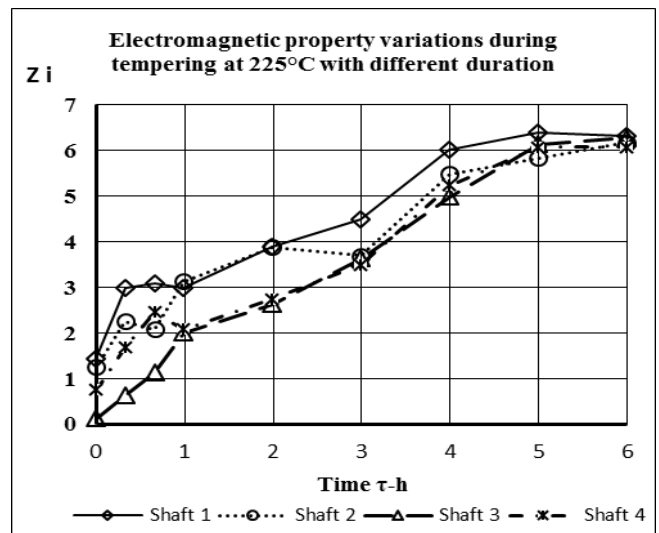
Fig.1 *Electromagnetic property variations {Zi;I = 1, 2, 3, 4} in relation to the tempering duration for different shafts at 225°C.*

Fig.2 represents the interpolation between the mean electromagnetic property Z and tempering time τ, which is described by means of the following regression model with Correlation Coefficient - Rsq=0.95:

(2) $$Y = 2.72 * X^{0.4397}$$

where Y↔ Z mean, X↔ Time τ [h].
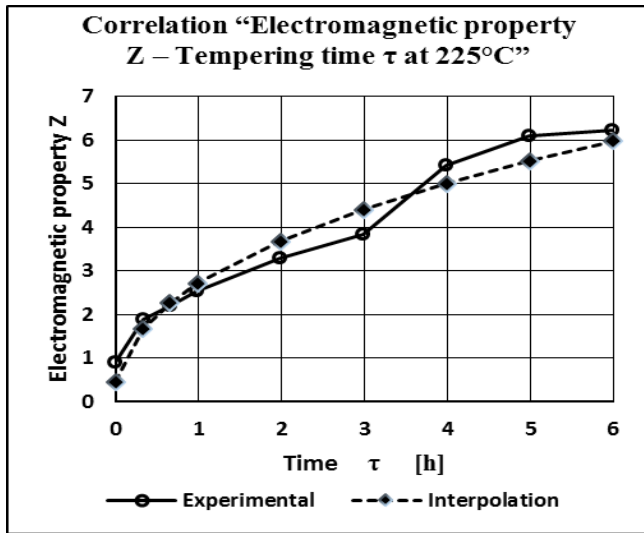
Fig. 2 *Variations in the mean electromagnetic property Z (for 4 shafts) in relation to the tempering duration τ and the interpolation curve.*

After taking the logarithm of (2), we obtain:

(3) $$log \overline{Z} = log\, 2,72 + 0,4397 * log\, \tau$$

The relationship introduced by **Hollomon-Jaffe** for the tempering parameter at constant temperature (T=constant) would be:

(4) $$Pa = T * (a + log\, \tau) = T * a + T * log\, \tau$$

or with T= constant =>

(5) $$Pa = const\, 1 + const.\, 2 * log\, \tau:$$

From (3) we get:

(6) $$log \overline{Z} = const\, 3 + const\, 4 * log\, \tau$$

The **Pa** values, calculated in (5) are given in Table 2 and Fig.3 with the constant a=15.
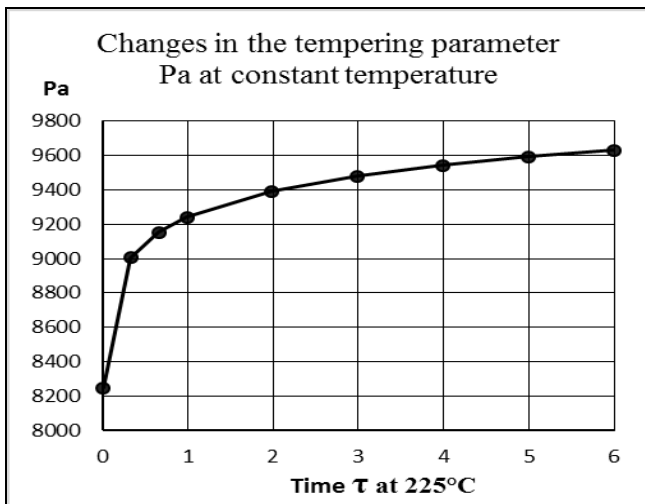
Fig.3 *Variations in the tempering parameter Pa in relation to the duration of tempering τ.*

5.2 Isothermal incremental change in tempering temperature with 1-hour hold at each level/step with a total duration of 6 hours.

The HRC hardness variations in the course of the experiment are represented by Fig. 4.
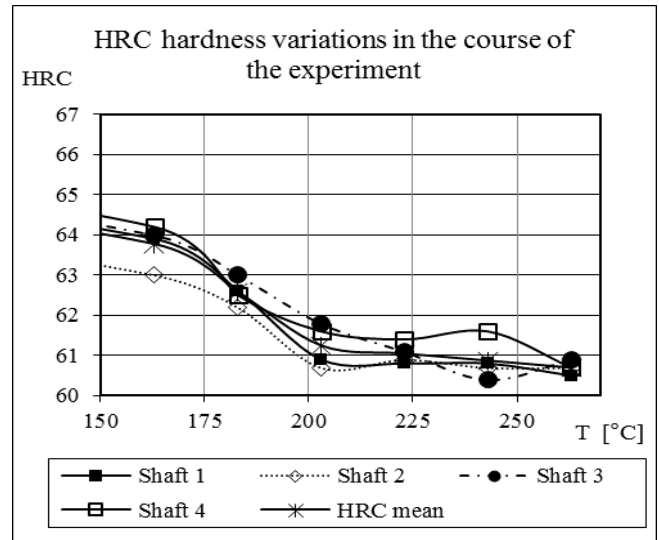
Fig. 4 *Variations in HRC hardness during low-temperature tempering at increasing temperature and duration.*

The interpolation of data on the mean hardness values for the four shafts during the different tempering stages is given by a third-degree polynomial:

(7) $$HRC = 115 - 0,6296 * T + 0,002413 * T^2 - 3,096E - 6 * T\text{\textasciicircum}3$$

and Correlation Coefficient Rsq=0.9858.

The variations in the electromagnetic property **Z** are given in Fig.5.
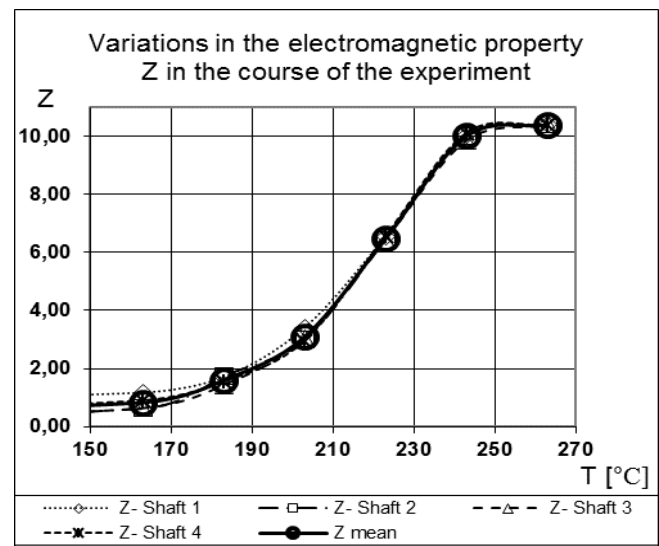
Fig.5 *Variations in the electromagnetic property Z during low-temperature tempering*

The experimental data on the electromagnetic property is also given in a third-degree polynomial:

(8) $$Z(T - \tau) = 257,2 - 3,826 * T + 0,01847 * T^2 - 2,847E - 5 * T\text{\textasciicircum}3,$$

46

The values calculated for the tempering parameter **Pa** from equation (1) are given in Table 2.

Table 2. *Experimental data on HRC and Z for the studied temperatures and duration, given by means of the tempering parameter **Pa**.*

Time [sec]	Temperature [°K]	Pa	HRC	Z
3600	436,15	8093	63,78	0,83
7200	456,15	8602	62,58	1,61
10800	476,15	9063	61,25	3,09
14400	496,15	9505	61,05	6,49
18000	516,15	9939	60,88	10,01
21600	536,15	10366	60,7	10,40
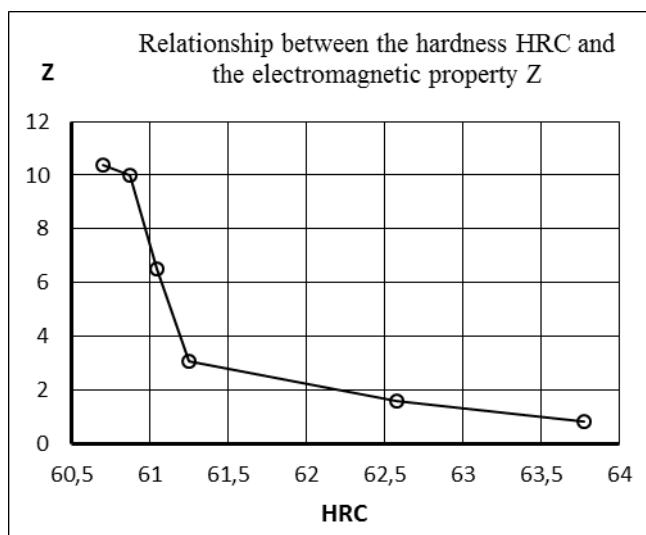
Fig.6 *Variations in the hardness HRC and the electromagnetic property Z in the course of the experiment*

Fig.6 shows the variations in the hardness HRC and the electromagnetic property Z, and Fig. 7 represents part of the master diagram of the low tempering of 20CrMo5 steel after carburizing and quenching.

Fig.7 *Changes in the hardness at different tempering parameters*

The representation of the variations in the two quality indicators HRC and Z as a function of the tempering parameter reveals a range of capabilities of recalculating and achieving the necessary combinations of the two technological factors, so that the requirements would be met.

6. Discussion

The eddy current inspection of low-temperature tempering is sensitive to the changes in the structure and the inside tension of carburized and quenched parts. It is evident in Fig.1 and Fig.4 that the changes in the hardness and the electromagnetic property have the most significant deviation at the beginning of the process. It is only after 6 hours at constant temperature and after reaching 250°C that the quality indicators for the different specimens reach equivalent levels. Even this fact alone is enough to question the feasibility of low-temperature tempering processes and durations under 3 hours. The variations in the electromagnetic property and the tempering parameter in the first group of experiments, as a function of the duration of the process, are similar, and they show that with the increase in duration at a certain temperature, the changes in the parts are closer to stability and closer to termination/completion. This is a reason why all previous changes should be considered as degrees in the tempering process. On the other hand, with the increasing temperature and duration of tempering, /the second group of experiments, Fig.5/, the electromagnetic property stops changing significantly at around 250°C. At the same time, significant changes in the hardness occur up to 200°C, Fig.4. The electromagnetic property starts changing significantly only after reaching the hardness of around 61-61.5 HRC, Fig. 6. The variations in hardness for the different tempering parameters, Fig.7, has two clear-cut linear periods: up to HRC 61.3, and after that value. After that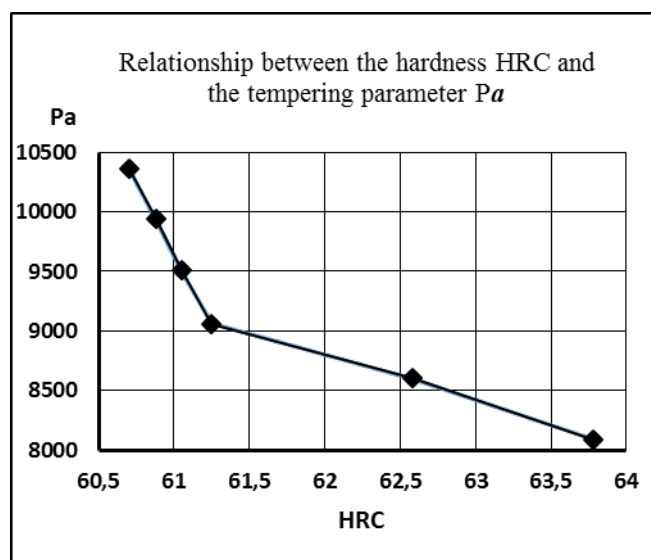 hardness value, even if the tempering parameter increases significantly, the hardness will change very slowly. This fact makes it even more difficult to control the process at this stage by measuring the hardness by Rockwell C method. It is exactly here, in this period, that the electromagnetic property variations provide a favourable means of controlling the process.

7. Conclusions

Carburized and quenched parts pose a challenge in inspecting and grading after low-temperature tempering. Commercial production creates prerequisites for big deviations in quality indicators. In the last stage of thermochemical treatment, control by means of hardness measurements is unable to detect changes in parts, and the registered level of hardness cannot guarantee the quality of the process and give a correct forecast about the exploitation potential of parts. The measurement of hardness cannot provide the necessary information about the kinetics of the occurring processes. The combination of the two technological factors, temperature and duration, into one, the tempering parameter **Pa**, is useful and convenient, and allows for the technological determination of levels by means of two-dimensional diagrams and search for cost-effective modes of low tempering. It is necessary that observation is carried out for every steel grade used. The eddy current testing provides an opportunity for the simultaneous control of the two combined technological factors; it provides information on the speed of the ongoing processes; it registers and offers a quantity criterion for statistical data on deviation inherently occurring in the parts or externally conditioned by the furnace unit. The similarity in the changes in the electro-magnetic characteristic and the Hollomon-Jaffe tempering parameter in the experimental conditions of the study proves that the results of low-temperature tempering depend on the diffusion rate, and also on the fact that these two quantities are the two sides of the same technological process: its input and its output.

8. *References*

1.Berns Hans, Stahlkunde für Ingenieure, Springer-Verlag 1993, S.43-48.

2.Liedtke. D., R.Jönsson, Wärmebehandlung, Expert Verlag, 1998, S.39-44;295-306.

3.Technologie der Wärmebehandlung von Stahl, VEB Deutscher Verlag für Grundstoffindustrie, Leipzig,1987,S.158-165.

4. Balevski A., Metal Science, Technology, Sofia, 196, .290-292,

5. Mihaylov I., etc., Technology of Heat Treatment, VIMMESS, Ruse, 1976, p.58-68

6.Schumann H., Metallographie, Deutscher Verlag für Grundstoffindustrie, Stuttgart, 1991, S.540-543

7.Kaffenberger M., Vorhersage der Einsatzhärtungsergebnisses aus dem Aufkohlungsprofil und den Abschreck- und Anlassbedingungen, Dissertation zur Erlangung des Grades eines Doktors des Ingenieurwissenschaften, Naturwissenschaftlich-Technischen fakultät Universität Siegen, 2012,S.78,131-136,175-176.

8. Gulyaev A.P., Introduction into Metal Science, Metallurgy, Moscow, 1977, p.281.

9. Lahtin Yu. M., Thermochemical treatment of metals, Metallurgy, Moscow, 1985, p.60-63

10. Quality control of heat treatment of steel products and parts, Reference book, edited by Kalner V. D., Machine building, Moscow 1984, p.193; 218-223

11. Hollomon, J.H., Jaffe, L.D. Time-Temperature relations in Tempering Steel, Metals Technology 1945-Volume XII, p.26

12. Murphy S., J.H. Woodhead, An Investigation of the Validity of Certain Tempering Parameters, Metallurgical and Materials Transactions, March 1972,Volume 3, Issue 3, p 727 .

13. Ivanov J., Eddy-current structuroscopy, technological factors and quality indicators in thermochemical treatment, XXV National conference with international participation "Defectoscopy '10", Year XVII, issue 5(115), June 2010, p. 594-601

14. Ivanov J., Eddy-current control of steels 30CrNiMo8 и 18CrNiMo7-6. Working frequency selection. Control methodology, XXIX International conference "Defectoscopy '14", June , 2014, Sozopol, Bulgaria, Year XXII, Issue 1(150), June 2014, p.335-338

15. Popov A., Eddy-current testing, Training tool, Sofia, 1984

16. Tsvetkov D., etc., Electromagnetic defectometrics, Technology, Sofia,1981

17. EN ISO 15549:2010 /DIN EN 12084-2001-06/ Non-destrictivetesting-Eddy current testing-General principles

18. DIN EN ISO 6508 1999-09 Härteprüfung nach Rockwell (HRC)

19.Qstatlab-Statistical software

(Originally written in Bulgarian)
(Originally written in Russian)

PLASMA-AIDED SURFACE FINISHING FOR
FLAME RETARDATION OF WOOD THROUGH THE USE OF SURFACTANTS

Assist.-Prof. Ivanov I., Prof. Dineff P. Ph. D.
Faculty of Electrical Engineering - Technical University of Sofia, Bulgaria
E-mail: igi@tu-sofia.bg

Abstract: *The plasma aided flame retardation of wood, wooden products and cellulosic fibrous materials has been conceived and developed as a result of plasma aided process of capillary impregnation with nitrogen- and phosphorous containing water solution. The surface pre-treatment in non-thermal equilibrium atmospheric pressure plasma substantially alters its electrical, chemical and capillary activity, thus improving some basic characteristics, such as penetration depth, water solution spreading and wicking, liquid adsorption capacity. This study has been developed as part of a large investigation on plasma-chemically activated wood surface and its capillary impregnation with nitrogen- and phosphor flame retardant containing water solution. It has been used to reveal and illustrate the impact of some ionic and silicon surfactant. The experimental studies of some chemical, ion and capillary activity changes of three species of rain-forest Mexican heart wood surfaces using selected surfactants and spreaders show that they have substantial contribution to the effective plasma-aided capillary impregnation processes.*

Keywords: ATMOSPHERIC OR AIR DIELECTRIC BARRIER DISCHARGE (*DBD*), FLAME RETARDATION OF WOOD, PLASMA-AIDED SURFECE FINISHING PROCESS, SURFACTANT, SILICON SURFACTANT, SPREADER.

1. Introduction

Surface finishing is the art in manufacturing having to do with substrate new useful texture, morphology, and properties. It is well known that these processes may range from deposition, removal, or cleaning. Such processes are conducted inside sophisticated tools that can be limited in their flexibility for research and development.

Corona surface treatment

Since 1951 *corona treatment* (*Verner Eisby*, *Vetaphone A/S*, Denmark) is currently the most used surface finishing technique in the industry for treating surfaces of polymer films and textiles. "*Corona*" is a *Dielectric Barrier Discharge* (*DBD*) in air at atmospheric pressure and room temperature. This kind of electric discharge is controlled by a dielectric barrier and is in form of streamers distributed in a haphazard manner over the surface, [4].

The *Corona surface treatment or Atmospheric pressure plasma treatment (APPT)* is essential in converting processes. A quality *Corona* is necessary to obtain sufficient wetting and adhesion on plastic films or metallic foils before the printing, laminating or coating. Due to the low surface energy (surface wettability, adhesion) of stock materials the printing press or laminator cannot run at full speed. *Corona systems* are used to create fresh clean surface that is receptive to ink, glue and lacquer. This *Corona technique* has proved to be both highly effective, cost-effective and can take place "*in-line*", [4].

In general the following rule is true: "*A material will be wetted, if its surface energy is higher than the surface tension of the liquid*". If not, there will be wetting and adhesion problems.

Durability of corona treatment or how long does it last?

Over time the obtained surface energy (*dyne-level*) will decrease and it can be necessary to corona treat the material again *just before use*. Also storage conditions and temperatures can affect the decay of the corona treatment result.

Generally, the more difficult a material is to treat the quicker it is likely to decay with time. It has been established that polymer film with very high slip additives (over 1200 ppm) can be totally resistant to printing just 24 hours after treatment, and it may be necessary to process the film immediately following treatment, or boost *the treatment in line* with the printer. Material which has not been treated under extrusion can be difficult to treat afterwards. Therefore it is recommended to treat film just after the extrusion, and then use a *refreshment treatment* just before the liquid/media is supplied to the surface, [4].
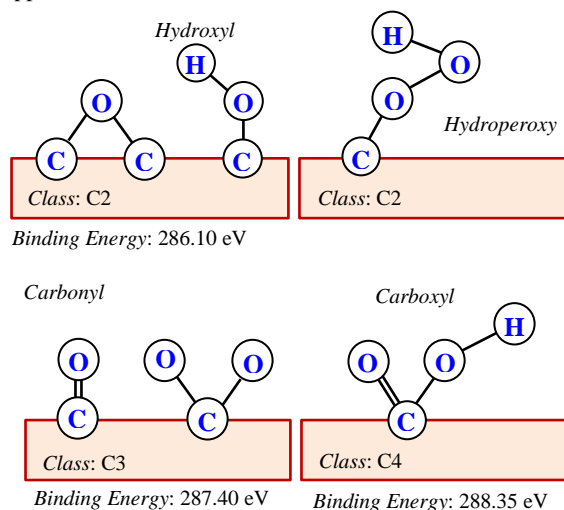
Fig. 1. Changes of wood surface chemistry after plasma surface *DBD* (corona) pre-treatment (or functionalization). Classes of various oxygen containing functional groups according to number of oxygen atoms bonding to carbon atom: *Class C2,* with one oxygen atom (C-O; C-OH); *Class C3*, with two oxygen atoms (O-C-O) or with one carbonyl oxygen atom (C=O); *Class C4*, with one carbonyl and one non-carbonyl oxygen atoms (O-C=O), (after *Kazayawoko*, 1998).

EASI-Plasma improvement

However, on some materials the *atmospheric pressure plasma effects* are limited and have a relatively short life time. *Long time surface functionalization* are achieved by using a *DBD*-plasma and adding small quantities of dopant gas for functionalization in a pure nitrogen atmosphere (*Enhanced Atmospheric Surface*

Improvement or *EASI-Plasma* treatment, *Vetaphone A/S*, 2001). The *EASI-Plasma* is more homogeneous and "*softer*" than Corona, with low heat impact to the surface and it enables the realization of a versatile controlled surface chemistry. Consequently it can be considered as a *gas primer replacing* efficiently both the use of corona treatment and liquid primer. Hydrophobic, hydrophilic or anti-fog surface properties can also be achieved with a 1 to 50 nm thin coating, [4].

Plasma surface pre-treatment "out line" or "in situ"

The *plasma-aided flame retardancy* of wood and wooden products has been developed as a result of creating new *functional coating* containing phosphor and nitrogen flame retardant. The *flame retarded coating* was built by new *plasma-aided surface finishing process* of capillary impregnation. The so called "*open time*" between plasma pre-treatment and capillary impregnation can reach up to 24 hours or the capillary impregnation is not obligatory to follow the plasma pre-treatment immediately such as corona treatment, [1].

*Plasma-aided finishing process* comprises of: *i* - plasma-chemical (*DBD-*) surface pre-treatment for increasing the wood surface energy and altering its chemical, electrical (ionic) and capillary activities; *ii*- change of ionic activity and surface tension of flame retardant (*FR*) containing water solution by ionic and non-ionic aqueous surface-active agents (surfactants), and in general for improvement some characteristics of the capillary impregnation process such as solution spreading and wicking speed, as well as the amount of the penetrated (sorbed) flame retardant. In this way, the plasma pre-treatment of wood improves wooden flame retardancy, Fig. 2, [1, 2, and 3].
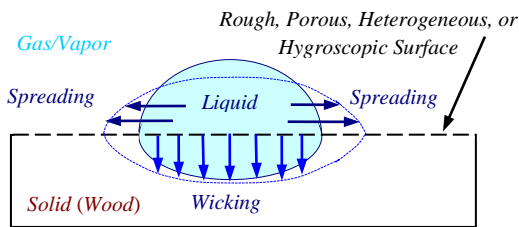
Fig. 2. *Model of wetting phenomena - the wetting phenomena on a real surface can be involved by: i - spreading of liquid over a solid surface; ii - wicking of liquid into the porous solid (such as wood).*

The *Sessile Drop Technique* is a method for characterization of wood (solid) surface energy. The measured contact angle and the known surface energy of the probe liquids are the parameters which can be used to calculate the solid sample surface energy. Time-depending change of contact angle θ of a flame retardant (*FR-*) water solution as it advances slowly over a non-ideal wood surface (e.g., not chemically homogeneous, rough or not perfectly smooth, porous and hygroscopic as in the case of most practical wood surfaces) can by determined by contact angle measurements 2 and 24 hours after *DBD*-treatment, [5].

The objective of this paper was to study the effect of some surfactants, [1, 2 and 3], on plasma-aided finishing process and more precisely on the "*open time*" between plasma treatment and capillary impregnation. Reaching an open time of 24 hours is a guarantee for the successful implementation of this plasma-aided process "*in situ*" or out of the production line. This study has been developed as part of a large research on plasma-chemically finished wood surfaces and flame retarded constructive wood products.

2. Experimental Investigation

A *low contact angle* indicates a high solid surface energy, and a high or sometimes complete degree of wetting. For example, a contact angle of zero degrees will occur when the droplet has turned into a flat puddle: this is called complete wetting. The droplet was deposited by a syringe pointed vertically down onto the wood surface and a high resolution camera captures the image, which can then be analyzed by using image analysis software. By taking pictures incrementally as the droplet advances over the surface the user can acquire a set of data to get a good time-depending change of the contact angle, [2, 3].

The apparatus used for this study was a KRÜSS Drop Shape Analyzer DSA 30. Precisely controlled tempering and humidity chambers help to provide a realistic modeling of the process conditions. Measuring range (referred to image analysis): contact angle - 1÷180 deg; surface free energy - 0.01÷1000 mN/m. Measurement resolution: contact angle - 0.1 deg; surface free energy - 0.01 mN/m. Test volume of the used sessile drop: 20 μl (20 mm^3). Zoom: 6.5 times and image resolution: 45 pix/mm, [2].

A way to experimentally determine liquid capillary penetration (spreading and wicking) is to look at the contact angle (θ). If $\theta = 0$ deg, the liquid completely wets the substrate; if $0 < \theta < 90$ deg, high wetting occurs; if $90 << \theta < 180$ deg, low wetting occurs; if $\theta = 180$ deg, the liquid does not wet the substrate at all.
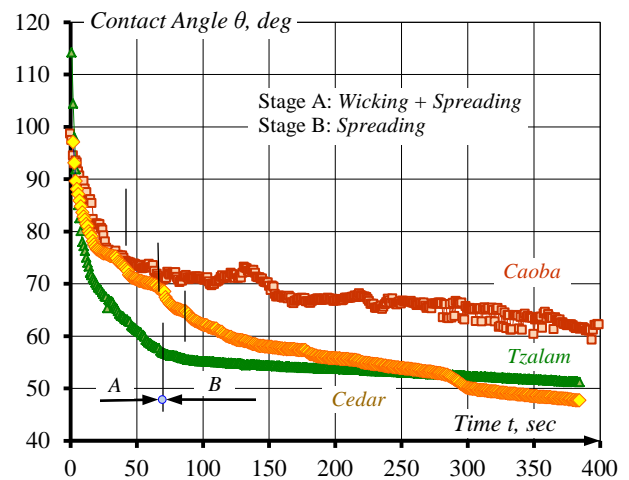
Stage A: *Wicking + Spreading*			
Duration, sec	86	47	100
Initial Contact Angle, deg	114.2	92.2	97.1
Final Contact Angle, deg	51.3	74.3	47.9
Wood Samples	*Tzalam*	*Cedar*	*Caoba*

Fig. 3. *Time-depending changes of contact angle θ of basic FR-water solution as it advances slowly over the non-ideal bare (non-plasma treated) wood surfaces. There are two very different stages of wetting behavior. The first stage A or wicking stage is completed in time of 100÷150 sec and the contact angle rapidly decreases.*

The determination of surface free energy and its disperse and polar fractions are performed after contact angle measurement with three well known probe liquids: *Water* (bifunctional); *Ethylene glycol* (acidic), and *n-Hexadecane* (neutral), [2, 3].

On the basis of prior art, as well as on our own former experience in plasma-aided capillary impregnation of wood, [1, 2], an oxidative (nitrogen oxides, NO_x) surface plasma pre-treatment has been applied on two sides of the test samples for 60 sec in a *DBD* at industrial frequency (50 Hz) and 18 kV (*RMS*) or about 25.4 kV (*PV*) voltage.

Studies of *cold plasma functionalization phenomena,* i.e. interactions of oxidative cold plasma with wood surface may add valuable information about the capillary impregnation, gluing and coating properties of wood. Such information is essential in the development of efficient processing methods and for the prediction of the functionality and durability of wood products.

Three species of rain-forest Mexican heart wood were investigated: two hardwoods, *i - Tzalam* (*Lysiloma bahamensis*); *ii - Caoba Mahogany* (*Swietenia macrophylla*); and one softwood, *White Cedar* (*Cupressus Lusitanica*).

Results and discussion

The contact angle is amended in a specific way in the study of porous media - at the initial moment it has a given value, significantly lower after 5 sec and substantially (with 30 to 50 %) less after the first or wicking stage, Fig. 2 and 3, Table 1.

Table 1. Contact angle *θ* measured dynamically by Sessile Drop Test with water – the contact angle increases dramatically after 24 hours and there is no significant wetting effect (see Caoba Mahogany).

Sessile Drop Test (Water)			
Samples	Tzalam	Cedar	Caoba
Bare Wood Samples			
Initial Contact Angel θ, deg	126.7	98.9	92.1
Contact Angel θ (5 sec), deg	97.6	92.6	71.3
Contact Angle θ (300 sec), deg	56.7	62.0	65.0
Plasma Pre-Treated Samples			
Contact Angle θ (2 hours), deg	19.2	70,2	21.3
Contact Angle θ (24 hours), deg	84,0	78.2	101,0

Reason for this characteristic for porous media (wood and wooden products) amending of contact angle, surface free energy and polarity, Table 1 and 2, is the presence of wicking that accompanies spreading and dominates in the first or wicking stage (A) of wetting and capillary impregnation process, Fig. 3.

Table 2. Calculated total surface free energy and its fractions of bare rain-forest Mexican wood samples 5 sec (Stage A: wicking+spreading) and 300 sec (*Stage B*: spreading) after droplet deposition on surface at about 22 ^{0}C.

Polar fraction and polarity (*P*) of bare wood samples increase substantially (more than two times) after completion of the

Sessile Drop Test (*Bare Wood Samples*)				
Total Surface Free Energy, mN/m				
Sample	Zisman Theory	Equation of State (EOS) Theory	Fowkes Theory	Wu Theory
5 sec after droplet deposition on wood surface				
Tzalam	30.24	31.50 ± 4.61	29.77	42.46
Cedar	32.50	33.04 ± 7.54	30.89	44.11
Caoba	33.10	32.58 ± 8.89	29.91	42.95
300 sec (5 min) after droplet deposition on wood surface				
Tzalam	34.74	42.25 ± 12.82	46.46	59.19
Cedar	34.74	38.20 ± 10.10	38.94	52.88
Caoba	34.74	38.91 ± 10.28	40.82	54.52
Fractions of Total Surface Free Energy				

	Fowkes Theory			Wu Theory		
Sample	Polar Fraction	Disperse Fraction	Polarity, *P*	Polar Fraction	Disperse Fraction	Polarity, *P*
	mN/m	mN/m	-	mN/m	mN/m	-
5 sec after droplet deposition on wood surface						
Tzalam	4.74	25.04	0.159	7.53	34.93	0.177
Cedar	4.04	26.85	0.131	6.90	37.21	0.156
Caoba	2.66	27.25	0.089	5.21	37.73	0.121
300 sec (5 min) after droplet deposition on wood surface						
Tzalam	17.67	28.78	0.380	19.45	39.74	0.329
Cedar	10.16	28.78	0.261	13.14	39.74	0.248
Caoba	12.04	28.78	0.295	14.78	39.74	0.271

wicking stage of capillary impregnation. This means that the initial contact angle affects the participation of both basic processes - wetting and capillary impregnation, which run in parallel and at different speeds. For the same purpose due to technical impossibility to measure the initial contact angle it should be measured after 5 sec from droplet deposition on the surface.

The study of the plasma treated wood surfaces makes it possible to show the effects of increase of surface free energy and of surface polarity after plasma treatment. However after 24 hours this effect decreases considerably, Table 3.

The effects of plasma aided *FR*-impregnation can be easily studied by using suitable solutions and registering the kinetics of change of the contact angle, Fig. 4, 5 and 6.

By following a similar manner it is possible to study plasma aided flame retardancy enhanced with surfactants, object of the current study, Fig. 4, 5 and 6.

Table 3. Calculated total surface free energy and its fractions of bare rain-forest Mexican wood samples 5 sec (Stage A: wicking + spreading) and 300 sec (*Stage B*: spreading) after droplet deposition on surface at about 22 ^{0}C. Sessile drop measurement with three test flame retardant (*FR-*) liquids 2 and 24 hours after plasma (*DBD-*) treatment. *NA* – unable to be measured.

Sessile Drop Test (*Plasma Treated Samples*)				
Total Surface Free Energy, mN/m				
Sample	Zisman Theory	Equation of State (EOS) Theory	Fowkes Theory	Wu Theory
Bare wood samples (5 sec)				
Tzalam	30.24	31.50 ± 4.61	29.77	42.46
Cedar	32.50	33.04 ± 7.54	30.89	44.11
Caoba	33.10	32.58 ± 8.89	29.91	42.95
2 hours after plasma treatment				
Tzalam	NA	47.08 ± 21.17	57.27	63.18
Cedar	NA	43.47 ± 21.75	49.25	56.20
Caoba	27.90	35.41 ± 7.44	37.96	40.62
24 hours after plasma treatment				
Tzalam	30.33	32.68 ± 4.96	34.77	37.54
Cedar	31.44	29.17 ± 7.65	32.08	34.81
Caoba	29.77	33.89 ± 5.48	36.07	38.77
Components of Total Surface Free Energy				

	Fowkes Theory			Wu Theory		
Sample	Polar Fraction	Disperse Fraction	Polarity	Polar Fraction	Disperse Fraction	Polarity
	mN/m	mN/m	-	mN/m	mN/m	-
Bare wood samples (5 sec)						
Tzalam	4.74	25.04	0.159	7.53	34.93	0.177
Cedar	4.04	26.85	0.131	6.90	37.21	0.156
Caoba	2.66	27.25	0.089	5.21	37.73	0.121
2 hours after plasma treatment						
Tzalam	32.09	25.18	0.560	38.88	24.30	0.615
Cedar	24.41	24.84	0.495	33.25	22.95	0.592
Caoba	10.99	26.96	0.290	14.35	26.27	0.353
24 hours after plasma treatment						
Tzalam	6.50	28.27	0.187	9.78	27.76	0.260
Cedar	2.66	29.42	0.083	5.95	28.87	0.171
Caoba	8.19	27.88	0.227	11.46	27.31	0.296

Conclusion

The obtained results allow us to make the following conclusions:

- The *Sessile Drop Technique* enables direct study of the kinetic of liquid penetration by image analysis with *FR-* water solutions – basic phosphor and nitrogen containing *FR*-solution and *FR-* solution with different surfactants;

- The *Initial Contact Angle* or this at 5 sec after the droplet deposition on the surface may be used as a common feature of wetting and penetration process without separating the two parallel running elementary processes to wicking and spreading;

- The term defined as *superhydrophilic* is used for surfaces with a liquid contact angle of less than 20 degrees, where droplets spread out nearly flat. *Plasma aided flame retardancy* is a new technology that provides this effect at open time up to two and more hours but can't provide this effect after 24 hours after plasma treatment.
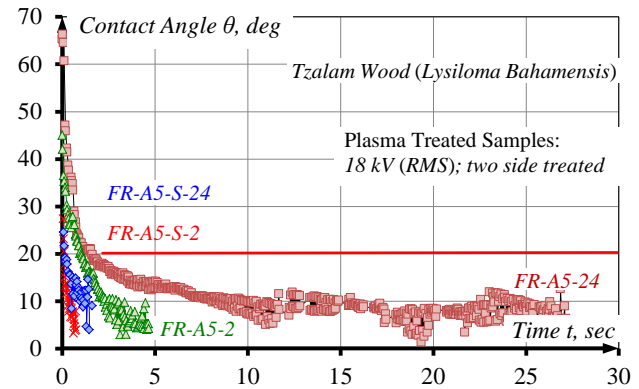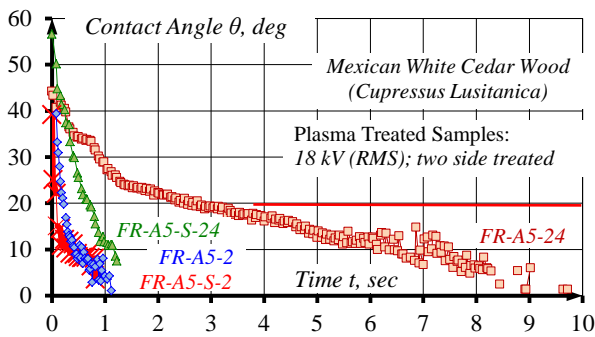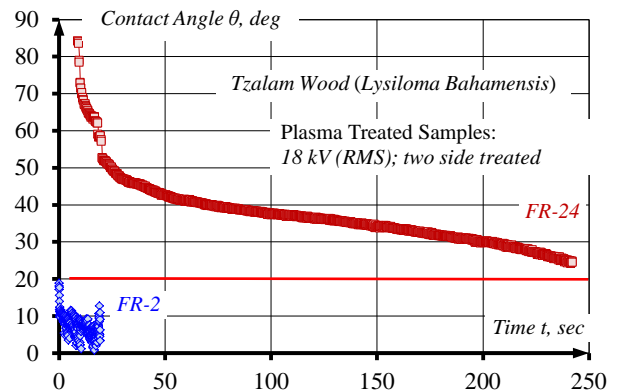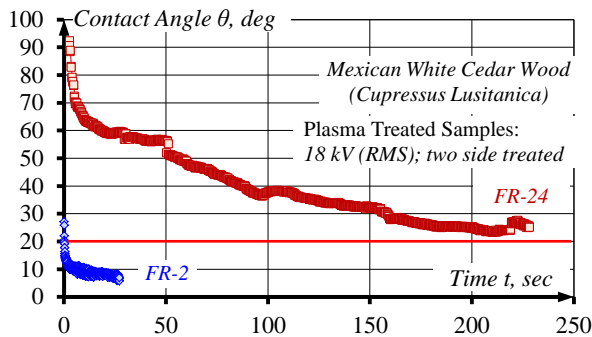
Fig. 4. Time-depending change of contact angle θ of basic (*FR-*) phosphor and nitrogen containing flame retardant water solution, *FR-* solution with 5 vol. % anionic phosphor surfactant (*FR-A5-*), and *FR-A5* solution with 0.1 vol. % siloxane surfactant (*FR-A5-S-*) as they advance slowly over the surface of plasma treated wood samples 2 and 24 hours after plasma surface pre-treatment (-2; -24).

Fig. 6. Time-depending change of contact angle θ of basic (*FR-*) phosphor and nitrogen containing flame retardant water solution, *FR-* solution with 5 vol. % anionic phosphor surfactant (*FR-A5-*), and *FR-A5* solution with 0.1 vol. % siloxane surfactant (*FR-A5-S-*) as they advance slowly over the surface of plasma treated wood samples 2 and 24 hours after plasma surface pre-treatment (-2; -24).
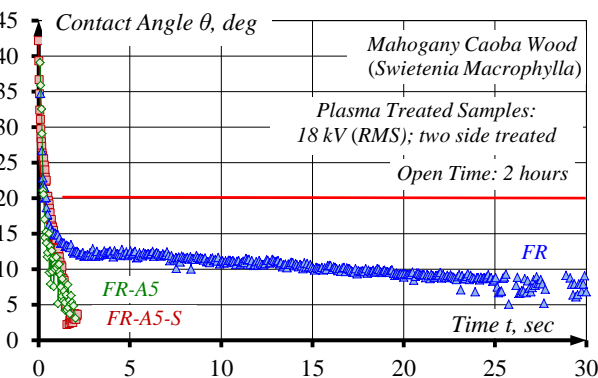
The contact angle remains larger than 20 deg, and for some of the studied wood samples (*Mahogany caoba*) – above 30 deg;

- *Plasma aided flame retardancy* (without surfactants) provides *superhydrophilic* wood surfaces for 2 hours open time at contact angle under 20 deg (even 10 and below 10 deg);

- *Surfactants enhanced* plasma aided flame retardancy enables „open time" up to 24 hours, while in general the contact angle decreases and remains below 10 deg, i.e. these surfaces are still *superhydrophilic* even after 24 hours;

- plasma aided flame retardancy *enhanced with surfactants* permits the implementation of „*in situ*" plasma finishing process.

References

[1] Dineff, P., L. Kostova. *Method for Plasma Chemical Surface Modification*. H05H 1/24, Bulgarian Patent Publication No.: BG 66022 B1; International Patent Publication No.: WO Patent 2006/133524 A2; Priority and Publication Date: 14.06.2005 (BG No. 109189)/21.12. 2006.

[2] Dineff, P., D. Gospodinova, and I. Ivanov. *Plasma-Aided Capillary Impregnation for Flame Retardancy of Wood: I. Surfactant-Assisted Capillary Impregnation*. Proceedings of Technical University of Sofia, Vol.: 64, Issue 4, **2014**, pp. 77÷86; ISSN: 1311-0829. VI-th Scientific Conference "EF 2014", September 15÷17, Sosopol, Bulgaria, **2014**.

[3] Dineff, P., D. Gospodinova, and I. Ivanov. *Plasma-Aided Capillary Impregnation for Flame Retardancy of Wood: II. Silicone Surface-Active Agent Effect*. Proceedings of Technical University of Sofia, Vol.: 64, Issue 4, **2014**, pp. 87÷96; ISSN: 1311-0829. VI-th Scientific Conference "EF 2014", September 15÷17, Sosopol, Bulgaria, **2014**.

[4] Eisby, Jan and Frank. *EASI-Plasma Brochure*. Vetaphone A/S. www.vetaphone.com, www.cpi-plasma.com (June, 2015).

Fig. 5. Time-depending change of contact angle θ of basic water solution (*FR-*), *FR-* solution with 5 vol. % anionic phosphor surfactant (*FR-A5-*), and *FR-A5-* solution with 0.1 vol. % siloxane surfactant (*FR-A5-S-*).

CAPILLARY PENETRATION (SPREADING AND WICKING) MECHANISMS IN PLASMA-AIDED SURFACE FINISHING PROCESSES

Assist.-Prof. Ivanov I., Prof. Dineff P. Ph. D., Assoc.-Prof. Gospodinova D. Ph. D.
Faculty of Electrical Engineering - Technical University of Sofia, Bulgaria
E-mail: igi@tu-sofia.bg

Abstract: *The plasma-aided flame retardation of wood, wooden products and cellulosic fibrous materials has been conceived and developed as a surface finishing process of capillary impregnation with nitrogen- and phosphorous flame retardant containing water solution. The surface pre-treatment in atmospheric pressure dielectric barrier discharge plasma substantially alters its capillary activity – the spreading on the wood surface and the wicking in the depth of wood, thus improving some basic characteristics of the impregnation process. This study has been developed as part of a large investigation on plasma-chemically activated (polarized, functionalized) wood surface and surfactants enhanced plasma aided capillary impregnation with nitrogen- and phosphor flame retardant containing water solution. The experimental studies of capillary activity changes on European white pine (Pinus Sylvestris, Bulgaria) wood surfaces using selected surfactants and spreaders show that they have substantial contribution to the effective plasma-aided capillary activity and impregnation processes.*

Keywords: ATMOSPHERIC DIELECTRIC BARRIER DISCHARGE, CONTACT ANGLE MEASUREMENT, FLAME RETARDANT, PLASMA-AIDED CAPILLARY IMPREGNATION, SESSILE DROP TECHNIQUE, SURFACE ENERGY DETERMINATION.

1. Introduction

The *plasma-aided flame retardancy* of wood and wooden products has been developed as a result of creating new functional coating containing phosphor and nitrogen flame retardant. The flame retarded coating was achieved by using a new *plasma-aided surface finishing process* of capillary impregnation. This *plasma-aided technology* comprises a surface plasma-chemical pre-treatment for alteration of chemical activity of wood surface as well as its electrical (ionic) and *capillary activities*, and in general for improvement of the *capillary impregnation process*, [1].

A technological system of plasma device and applicators has been created to produce cold technological plasma out of technological line or "*in situ*" through *air dielectric barrier discharge* (*DBD*) at atmospheric pressure and room temperature. The cold plasma pre-treatment of wood improves water solution spreading and wicking speed as well as a specific amount of the adsorbed flame retardant trough wood surface. In this way, the plasma pre-treatment of wood and wooden products improves its flame retardation [1, 2 and 6].

The objective of this paper was to study the effect of plasma pre-treatment on *European white* or *Scots pine* (*Pinus Sylvestris*, Bulgaria) wood surface functionalization as well as the effect of wood surface polarity on the wetting phenomena, both aiming to improve the capillary impregnation process. This study has been developed as part of a large research on plasma-chemically activated wood surface and flame retarded constructive wood.

2. Experimental Investigation

Wetting phenomena of wood may be characterized by using thermodynamic wetting parameters, for example contact angles, surface free energy, and work of adhesion, work of spreading or work of wetting, [3].

The wetting phenomena on a real (non-ideal) - *rough, porous, heterogeneous,* or *hygroscopic* wood surface, Fig. 1, can be involved by: *i - spreading* of liquid over a solid surface; *ii - wicking* of a liquid into a porous solid such as wood.
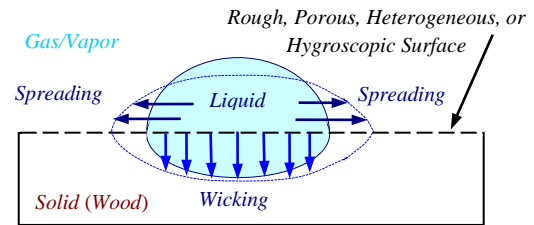
Fig. 1. *Young-Bikerman-Good model of wetting phenomena - the wetting phenomena on a real surface can be involved by: i - spreading of liquid over a solid surface; ii - wicking of a liquid into a porous solid such as wood.*

Wetting does not include dissolution or swelling of the solid by the liquid or any kind of chemical reaction between the materials that changes the system composition, (Berg, 1993).

Basic relations of wetting phenomena

Neumann and *Good* (1979) reviewed the classical techniques for measuring contact angles. Using well defined liquid, if the contact angle can be measured on a solid surface, the work of adhesion can be determined and the solid surface can be revealed. The most widely used technique, also regarding wood, involves digital image analysis of the profile dimensions of a droplet deposited on a horizontal surface from which the contact angle can be calculated - referred to here as the sessile drop method.

A *low contact angle* indicates a high solid surface energy, and a high or sometimes complete degree of wetting. For example, a contact angle of zero degrees will occur when the droplet has turned into a flat puddle: this is called complete wetting.

It must be emphasized that the contact angle of a liquid as it advances slowly over a non-ideal surface (e.g. not chemically homogeneous, porous and not perfectly smooth, as in the case of wood surfaces) changes (decreases) synchronously to droplet change and movement. The droplet was deposited by a syringe pointed vertically down onto the wood surface, and a high

resolution camera captures the image, which can then be analyzed by using image analysis software. By taking pictures incrementally as the droplet advances over the surface, the user can acquire a set of data to get a good time-depending change of the contact angle.

Contact angle measurement

The *Sessile Drop Technique* is a method for the characterization of wood (solid) surface energy. The main premise of the method is that by placing a droplet of probe liquid with a known surface energy on the solid surface. The measured contact angle and the known surface energy of the probe liquids are the parameters which can be used to calculate the surface energy of a solid sample, [5].

The apparatus used for this study was a KRÜSS Drop Shape Analyzer DSA 30. Measurement of the contact angle with three specified test liquids ensures maximum accuracy when determining the wood surface free energy. Precisely controlled tempering and humidity chambers help to provide a realistic modeling of the process conditions. Measuring range (referred to image analysis): contact angle - $1 \div 180$ deg; surface free energy - $0.01 \div 1000$ mN/m. Measurement resolution: contact angle - 0.1 deg; surface free energy - 0.01 mN/m. Test volume of the used sessile drop: 20 μl (20 mm^3). Zoom: 6.5 times and image resolution: 45 pix/mm, [5].

The aim of this study was to verify possibility of determining the contact angle values of the plasma pre-treated wood surface and calculate the surface free energy and its components from the obtained contact angle values using *Zisman*, *Equation of state* (EOS), *Fowkes* and *Wu* theory and calculation method. All methods described there are integrated in the KRÜSS Drop Shape Analysis program DS A1, [5].

The determination of surface energy of *European white pine* (EWP) and its disperse and polar components was performed after contact angle measurement with three probe liquids: *Water* (bifunctional; $\theta = 70.2 \pm 0.1$ deg, total surface energy - 72.8 mN/m; dispersive component - 21.8 mN/m; polar component - 51 mN/m; acid component - 25.5 mN/m, and base component - 25.5 mN/m); *Ethylene glycol* (acidic, $\theta = 41 \pm 0.1$ deg, total surface energy - 47.5 mN/m, dispersive component - 29.3 mN/m; polar component - 18.2 mN/m; and *n-Hexadecane* (neutral, $\theta = 10.3 \pm 0.1$ deg, total surface energy - 27.6 mN/m, dispersive component - 27.6 mN/m; polar component - 0 mN/m).

Contact angle measurement and capillary impregnation

Time-depending change of contact angle θ of a liquid as it advances slowly over a non-ideal wood surface (e.g., not chemically homogeneous, rough or not perfectly smooth, porous and hygroscopic as in the case of most practical wood surfaces) was determined by contact angle measurements 2 and 24 hours after atmospheric *dielectric barrier discharge* (DBD) surface pre-treatment in air.

A possible option to experimentally determine liquid capillary penetration (spreading and wicking) is to look at the contact angle (θ). If $\theta = 0$ deg, the liquid completely wets the substrate; if $0 < \theta < 90$ deg, high wetting occurs; if $90 << \theta < 180$ deg, low wetting occurs; if $\theta = 180$ deg, the liquid does not wet the substrate at all.

Gravimetric study of capillary impregnation by dipping

Fast ongoing processes of penetration (spreading and wicking), Fig. 1, may not always be examined by contact angle measurement technique. In this case the penetration study can be performed gravimetrically by dipping the test sample in impregnating solution. The test sample was immersed for 60 sec, drained for 60 sec and then weighed by laboratory balance (0.001 gr). This sample was dried at room temperature for 24 hours before being weighed again. Thus, the penetration was defined integrally by the weight of the absorbed solution and its corresponding dry matter (*flame retardant substance*).

Plasma-chemical surface pre-treatment

On the basis of prior art, as well as on our own former experience in plasma-aided capillary impregnation of wood, [1, 2], an oxidative (nitrogen oxides, NO_x) surface plasma pre-treatment has been applied on the test samples for 60 sec in a non-equilibrium cold plasma of atmospheric air dielectric barrier discharge (DBD) at industrial frequency (50 Hz) and 15 kV (RMS) or about 21 kV (PV) voltage.

European white pine (Pinus Sylvestris)

Pines are among the most commercially important tree species valued for their timber in general construction work throughout the world. Commercial pines are grown in plantations for timber that is denser, more resinous, and therefore more durable than spruce. Pine wood is widely used in high-value carpentry items such as furniture, window frames, paneling, floors and roofing.

European or Scots white pine (*Pinus Sylvestris*) is a species of pine that is native to Europe and Asia, ranging from Western Europe to eastern Siberia, south to the Caucasus Mountains and Anatolia, and north to well inside the Arctic Circle in Scandinavia.

European white pine properties: *Hard pine wood*: *Subgroup C* (Red Pines): Red Pine (*Pinus resinosa*, US); Austrian or European Black Pine (*Pinus nigra*, Europe); and *Scots* or *European White Pine* (*Pinus Sylvestris*, Europe); *Density* (average dried weight) - 550 kg/m^3; *Moisture content* (MC): $8 \div 12$ %; *Specific gravity* (basic/12 % MC): 0.39/0.55; *Tree size*: $20 \div 35$ m tall, $0.6 \div 1$ m trunk diameter; *Shrinkage*: Radial: 5.2 %, Tangential: 8.3 %, Volumetric: 13.6 %, T/R Ratio: 1.6; *Janka hardness* (12 % MC): 2.420 kN; *Modulus of rupture* (MOR): 83.3 MPa; *Modulus of elasticity* (MOE): 10.08 GPa; *Crushing strength* (compression strength parallel to grain): 41.5 MPa, [

European white pine a major source of timber and lumber intended for building constructions. The behavior of wooden structures during fire gives rise to strong public interest. This is our main motive for undertaking serious and ongoing for years research on flame retardancy of European white pine (pine) by using plasma aided flame retardancy. The method went through a successful industrial approbation in the practice of "*Interiorprotect*" Ltd. (Bulgaria), funded within a project by the *National Science Fund* at the *Ministry of Education and Science* ($2005 \div 2010$). The disclosure of various aspects of the phenomenon of plasma-aided flame retardancy represents a serious scientific interest.

Hard wood penetration or wicking

Capillary liquid penetration (or wicking) in hardwoods, like e.g. *European white pine* is mainly restricted to the filling of vessels and the first cells of rays and very occasionally axial parenchyma and sclerenchyma, [4].

In most of the permeable hardwood species (e.g. beech) vessels will be filled deeper and penetration in axial parenchyma and sclerenchyma would be more noticeable. The filling of a vessel by capillary impregnation is strongly reduced if tyloses are present. Extractives appeared to have none or only a very minor influence on the capillary penetration. Surface preparation can have some influence on impregnation penetration because sanding reduces the number of open cell capillaries in which flame retardant water solution can flow, [4].

Results and discussion

Surface energy of European white pine

Since wood surfaces are porous, rough and not perfectly smooth, sessile drop method requires some type of video capture in order to measure the contact angle which changes as the droplet is absorbed. The *n-hexadecane* completely wets the substrate and $\theta \to 0$. Time-depending change of the contact angle θ of two probe liquids – *water and ethylene glycol* as well as its slowly advance over the non-ideal wood surface are presented in Fig. 1.
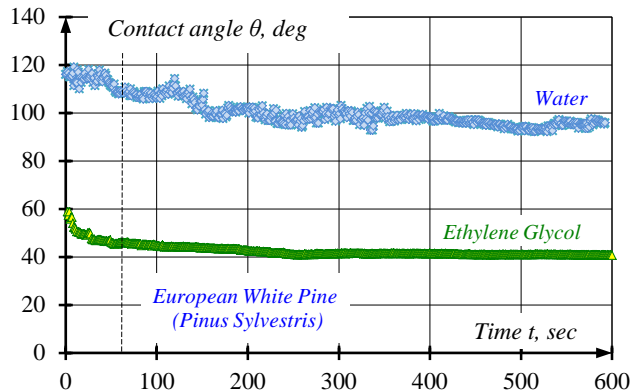
Fig. 2. *Time-depending change of the contact angle θ of probe liquids as well as its slowly advance over the non-ideal European white pine (Pinus Sylvestris) bare (non-plasma treated) wood surface.*

Based on the contact angle data of *EWP*-wood surface, the total surface free energy was obtained by using the *Zisman*, *Equation of state*, *Fowkes* and *Wu* theory and calculation methods, Table 1.

The polar and dispersive (non-polar) fractions are obtained using *Fowkes* and *Wu* theories. They are presented in Table 2.

Table 1. Calculated total surface free energy of *European White Pine* (*Pinus Sylvestris*) samples at about 22 ^{0}C.

Sessile Drop Test			
Total Surface Free Energy, mN/m			
Zisman Theory	Equation of State (EOS) Theory	Fowkes Theory	Wu Theory
28.40	22.71	± 7.95	29.06	29.86

The energy of the bulk part of a wood substrate is determined by the types of interactions that hold the substrate together. High energy substrates are held together by bonds, while low energy substrates are held together by forces. Covalent, ionic and metallic bonds are much stronger than forces such as Van der Waals and hydrogen bonding.

Table 2. Fractions of Total Surface Free Energy of *European White Pine* (*Pinus Sylvestris*) samples at about 22 ^{0}C.

Sessile Drop Test					
Fractions of Total Surface Free Energy					
Fowkes Theory			Wu Theory		
Polar Fraction	Disperse Fraction	Polarity/ Non-Polarity	Polar Fraction	Disperse Fraction	Polarity/ Non-Polarity
mN/m	mN/m	-	mN/m	mN/m	-
0.07	28.98	0.003/ 0.997	1.47	28.39	0.049/ 0.951

Low energy substrates such as *EWP-wood* (surface free energy: 29.6 mN/m) are wet harder than high energy substrates. The dispersive fraction of *EWP* surface energy is much greater than its polar fraction, Table 2, i.e. almost equal to the total surface free energy. In addition, more complete wetting (spreading

and wicking) will occur if the substrate has a much higher surface energy than the liquid.

Wetting and capillary penetration of European white pine

The contact angle of a liquid as it advances slowly over a non-ideal surface decreases synchronously to droplet movement. The high resolution camera of KRÜSS Drop Shape Analyzer DSA 30 captures the image, which was analyzed by using image analysis software. By taking pictures incrementally as the droplet advances over the surface we get a good time-depending change of the contact angle, Fig. 3 and 4.
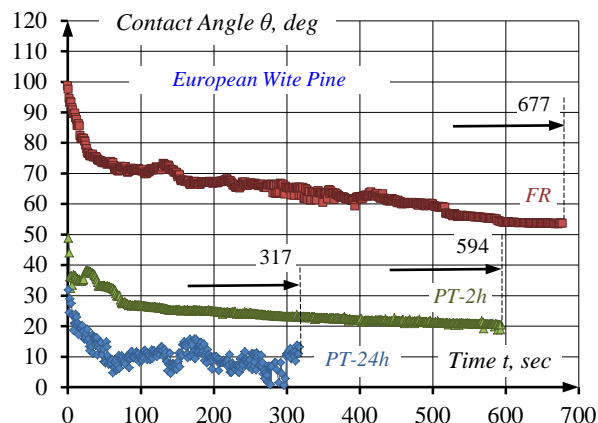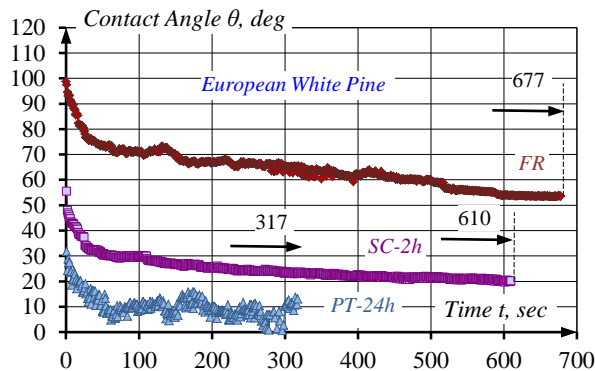

Fig. 3. Time-depending change of the contact angle θ of basic phosphor and nitrogen containing flame retardant as it advances slowly over the *European white pine (Pinus Sylvestris)* bare (non-plasma treated) sample surface (*FR*); 2 hours after plasma surface pre-treatment (*PT-2h*); and 24 hours after plasma surface pre-treatment (*PT-24h*).

This approach, however, is only applicable for slower running processes of wetting and capillary penetration, Fig. 3. In these cases the contact angle is very quickly reduced to zero and the software can not correctly implement image analysis. For rapid processes of capillary penetration only two parameters can be reported - initial contact angle (ICA) and time of penetration, Table 3.

Table 3. Sessile drop measurement with three test flame retardant (*FR-*) liquids for *European white pine* (*Pinus Sylvestris*) sample before and 2 hours/24 hours after plasma pre-treatment.

No	Samples	Age	Initial Contact Angle (*ICA*)	Time of penetration
FR				
		h	deg	sec
1.	Non-plasma treated	-	28.6	677
2.	Plasma treated	2	35.8	594
3.	Plasma treated	24	18.1	317
FR with 5 vol. % phosphor anionic surfactant (FR5)				
No	Samples	Age	Initial Contact Angle (*ICA*)	Time of penetration
		h	deg	sec
1.	Non-plasma treated	-	28.6	40
2.	Plasma treated	2	35.8	3
3.	Plasma treated	24	18.1	3
FR with 5 vol. % phosphor anionic surfactant and 0.1 vol. % siloxane surfactant (spreader) (FR5S)				
No	Samples	Age	Initial Contact Angle (*ICA*)	Time of penetration
		h	deg	sec
1.	Non-plasma treated	-	21.3	7
2.	Plasma treated	2	8.0	2
3.	Plasma treated	24	21.1	7

Fig. 4. Time-depending change of contact angle θ of basic phosphor and nitrogen containing flame retardant as its advance slowly over the *European white pine (Pinus Sylvestris)* bare (non-plasma treated) sample (*FR*); 2 hours active depolarization after plasma surface pre-treatment (*SC-2h*); and 24 hours after plasma surface pre-treatment (*PT-24h*).

The obtained results confirm the possibility to use "*open time*" up to 24 hours for capillary impregnation using flame retardant water solution with surfactants (*FR5* and *FR5S*), Table 3.
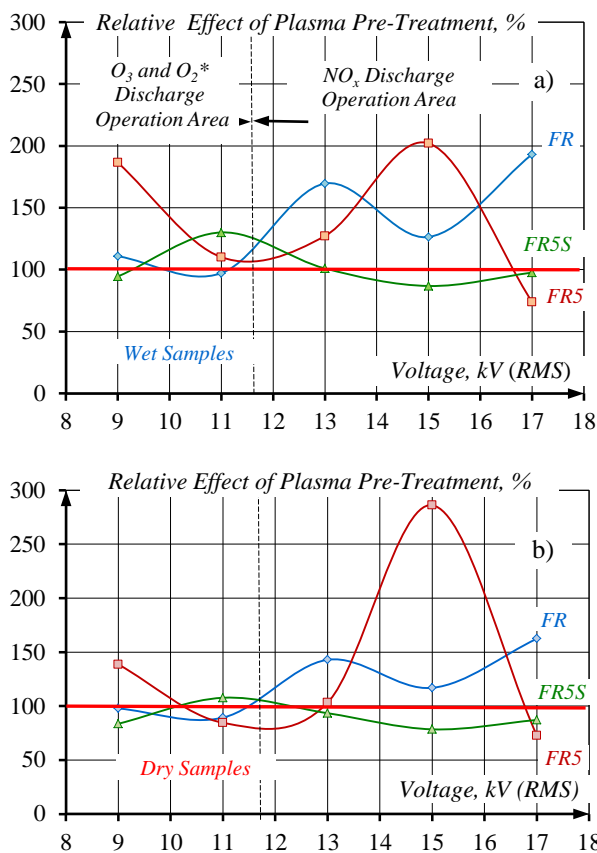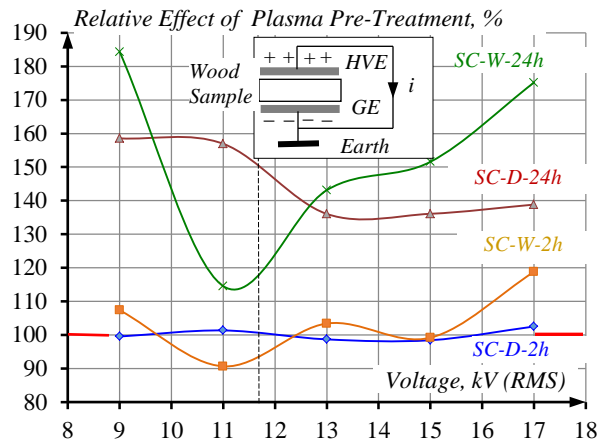

Fig. 5. Voltage-depending change of the relative effect of plasma-aided capillary impregnation – increase compared to the classic capillary impregnation, with three flame retardant water solution (30 mass % dry substances): *FR* – basic phosphor and nitrogen flame retardant containing water solution; *FR5* – *FR*-solution with 5 vol. % phosphor anionic surfactant; *FR5S* – *FR5*-solution with 0.1 vol. % siloxane surfactant (spreader): a – relative effect of penetrated solution (wet sample); b – relative effect of penetrated dry substance (flame retardant). Weight increasing for classic capillary impregnation (100 %): for the *FR*-solution: wet – 9.80 %; dry – 4.01 %; for *FR5*-solution: wet – 10.86 %; dry – 4.02 %; and for the *FR5S*-solution: wet – 14.44 %; dry – 5.24 %.

Besides the registered significantly less time for capillary penetration a hypothesis was experimentally verified for larger quantity of *FR*-solution and active substance when using *FR*-solution with surfactants (FR5 and FR5S).

It is experimentally verified that there are modes of plasma pre-treatment, which provide more absorbed solution, Fig. 5a, and more absorbed dry matter, Fig. 5b.

The hypothesis of electric polarization of wood samples at room temperature during plasma pre-treatment (plasma electret) is also experimentally verified. For this purpose after plasma pre-treatment the wood samples are being placed in depolarization conditions by wrapping them in aluminum foil, Fig. 6.

Fig. 6. Voltage-depending change of the relative effect of plasma-aided capillary impregnation in wet (-*W*-) and dry (-*D*-) state – increase compared to the classic capillary impregnation, with basic flame retardant (*FR*) water solution (30 mass % dry substances). The impregnation was carried out after 2 and 24 hours of effective depolarization. *HVE* – high voltage electrode; *GE* – ground electrode; *i* – short circuit current. Weight increasing for classic capillary impregnation (100 %) with basic *FR*-solution: wet – 9.80 %; dry – 4.01 %.

It is established that after two hours of depolarization at room temperature there is no change in the contact angle, Fig. 4 and 3, the relatively positive (compared to non-plasma treated sample) effect, both in wet and in dry conditions, is preserved. This show that there is no effective depolarization of the plasma pre-treated samples, which may be explained by the preservation of the dipole polarization (hetero-discharge) and the polarization resulting from created on the surface radicals.

References

[1] Dineff, P., L. Kostova. *Method for Plasma Chemical Surface Modification*. H05H 1/24, Bulgarian Patent Publication No.: BG 66022 B1; International Patent Publication No.: WO Patent 2006/133524 A2; Priority and Publication Date: 14.06.2005 (BG No. 109189)/21.12. 2006.

[2] Dineff, P., D. Gospodinova, and I. Ivanov. *Plasma-Aided Capillary Impregnation for Flame Retardancy of Wood: I. Surfactant-Assisted Capillary Impregnation*. VII-th Scientific Conference "EF 2013", September 17÷20, **2013**, Sosopol, Bulgaria.

[3] Ivanov, I., D. Gospodinova, P. Dineff, and L. Veleva. *Wood Surface Energy Determined by Sessile Drop Technique as Quality Parameter of Plasma-Chemical Modified Wood Surfaces*. International virtual journal "Machines, Technologies, Materials", **2014**, Year VIII, Issue 10, pp. 50÷53, ISSN 1313-0226; XI. International Congress "Machines, Technologies, Materials", **2014**, September 17÷20, Varna, Bulgaria: paper 74.

[3] Wålinder, M.. *Wetting Phenomena on Wood: Factors influencing measurements of wood wettability*. - Doctoral Thesis. Stockholm, KTH-Royal Institute of Technology, 2000, ISSN 1104-2117.

[4] De Meijer, M. *A review of interfacial aspects in wood coatings: wetting, surface energy, substrate penetration and adhesion*. Cost E 18, Final seminar: A review of interfacial aspects in wood coatings, p. 16, 2009.

[5] Krűss GmbH. *Contact angle measurement – a theoretical approach*. *Product brochure* (Drop Shape Analyzer–DSA30), www.kruss.de (July, 2015)

EFFECT OF EQUAL-CHANNEL ANGULAR PRESSING ON CRACK RESISTANCE AND CORROSION DAMAGE OF ZIRCONIUM ALLOY Zr-2.5%Nb

ИССЛЕДОВАНИЕ ВЛИЯНИЯ РАВНОКАНАЛЬНОГО УГЛОВОГО ПРЕССОВАНИЯ НА ТРЕЩИНОСТОЙКОСТЬ И КОРРОЗИОННУЮ ПОВРЕЖДАЕМОСТЬ ЦИРКОНИЕВОГО СПЛАВА Zr-2.5%Nb

Ph.D. Belov V.A., Dr.Sci. Nikulin S.A., Ph.D. Rozhnov A.B., Ph.D. Rogachev S.O.
The National University of Science and Technology "MISiS", Leninsky pr. 4, 119049, Moscow, Russia
vbelov@ymail.com

Abstract: *Testing method for static crack resistance has been developed and applied for thin sheet (sample thickness ~ 1mm) samples of zirconium alloy Zr-2.5%Nb. Linear parameter of fracture mechanics - stress intensity factor Kc has been determined. Alloy Zr-2.5%Nb after ECAP was tested for corrosion resistance in the physiological Ringer's solution for two years.*
KEY WORDS: ZIRCONIUM ALLOY, BIOCOMPATIBLE MATERIALS, SEVERE PLASTIC DEFORMATION (SPD), EQUAL CHANNEL ANGULAR PRESSING (ECAP), CRACK RESISTANCE, CORROSION DAMAGE

1. Introduction

Fracture resistance is the important characteristic of any type of metallic implants used in the human body. Along with titanium alloys, zirconium alloys are also promising material for medicine, because they have good biocompatibility [1]. However, strength properties of zirconium alloys are insufficient, and in order to increase the strength with sufficient ductility zirconium alloys are subjected to severe plastic deformation (SPD), by means of equal channel angular pressing (ECAP) [2-5].

Currently, the actual problem is the evaluation of the corrosion damage of biocompatible zirconium material during the exploitation in the human body, as well as determination of critical stresses of biocompatible alloys that may appear in the implant.

2. Experimental procedure

Corrosion test and crack resistance test of flat sheet samples from zirconium alloy Zr-2.5%Nb before and after ECAP were conducted at room temperature.

The size of samples for corrosion test was $10 \times 10 \times 1$ mm. Samples were incubated inside a glass bottle with Ringer's solution (composition per 200 ml of H_2O: NaCl - 8.6 g, KCl - 0.3 g, $CaCl_2$ - 0.25 g) within 730 days. These samples were placed in the glass bottle so that there were not contact between them to avoid a possible occurrence of "electrochemical couples". During the test, the glass battle was hermetically closed to prevent the solution evaporation. Every 30 days, each sample was removed from the glass battle using tweezers and was dried in air for 2 hours, then it was weighed on electronic scales GR-202.

Flat thin samples for static crack resistance test were cut on electrical-discharge machine Chmer GX360L from bars of zirconium alloy Zr-2.5%Nb after ECAP with a different number of passes (1-6). Then, hole with diameter of 1 mm was drilled and two thin transverse notches (2 mm in length) were made in the center of a flat sample (Fig. 1).
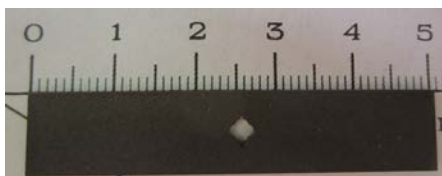

Fig. 1. *Typical view of the sample for crack resistance testing*

Uniaxial tensile tests of flat thin sheet specimens with the stress concentrators were carried on a universal test machine Instron 5569 using the acoustic emission (AE) method. The load of a crack initiation was determined from of the combined strain curves and acoustic emission (Fig. 2).
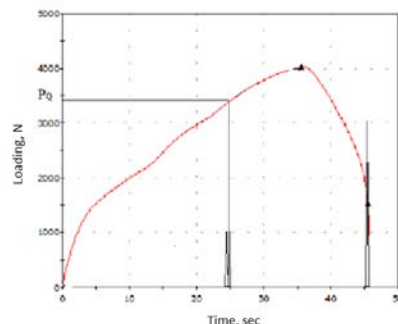

Fig. 2. *Typical view of a combined strain curves and AE*

Fracture surface of samples of zirconium alloy Zr-2.5% Nb in the initial state and after ECAP were investigated after the static crack resistance teste by scanning electron microscope (SEM) Hitachi S-800.

Also microstructure analysis of zirconium alloy Zr-2.5% Nb in the initial state and after ECAP was carried out by a transmission electron microscope (TEM) JEM 1400.

3. Results and discussion

Result of corrosion tests in Ringer's solution of the zirconium alloy Zr-2.5%Nb samples in initial state and after ECAP, showed that it was not revealed oxide film growth or shrinkage of the samples in the initial state and after ECAP.

Figure 3 shows structure of zirconium alloy Zr-2.5% Nb in the initial state and after ECAP.

It's shown that the average grain size in the initial state is 3.3 ± 0.5 µm (12 hours annealing) and 2.5 ± 0.1 µm (6 hours annealing), but the average grain size after ECAP is 300 ± 65 nm (1 pass) and 250 ± 50 nm (6 passes).

The severe plastic deformation by ECAP leads to the formation of partially oriented grain, subgrain and submicrocrystalline structure.
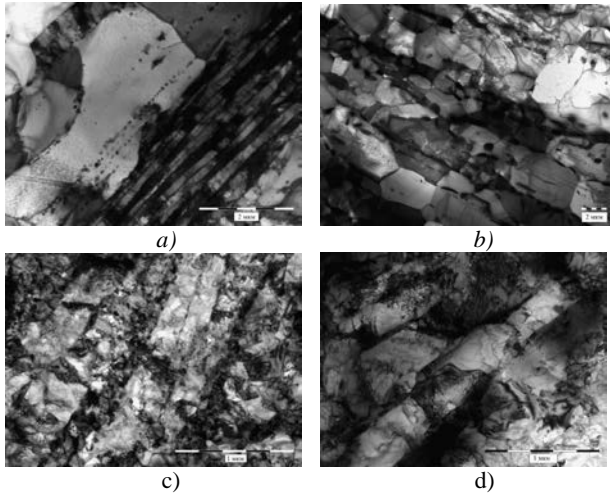
Fig. 3. *The microstructure of zirconium alloy Zr-2.5%Nb in the initial state: a - annealed for 12 hours at 580 °C, b - annealed for 6 hours at 580 °C; and after ECAP: c - single pass, d – 6 passes (TEM)*

The test results of flat thin samples of zirconium alloy Zr-2.5% Nb showed that the highest crack resistance observed in samples in the initial state after annealing for 6 hours at 580 °C ($Kc = 29.4 \pm 1.8$ MPa*m$^{1/2}$) and the lower crack resistance observed in samples after ECAP in a single pass ($Kc = 14.8 \pm 1.5$ MPa*m$^{1/2}$).

The fracture surfaces of zirconium alloy Zr-2.5% Nb samples in the initial state and after ECAP after the static crack resistance tests are shown at Fig. 4.
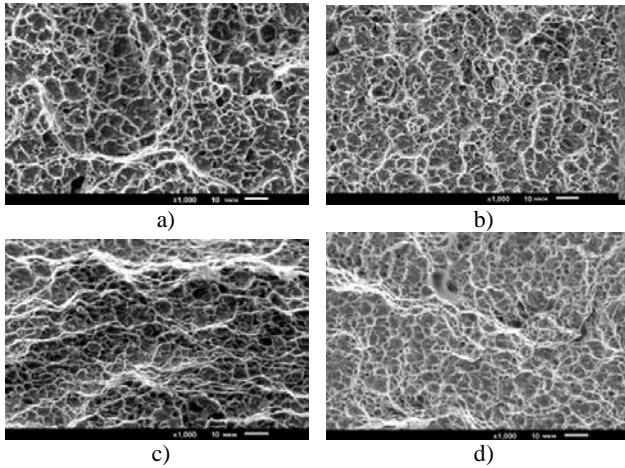
Fig. 4. *The fracture surface of zirconium alloy Zr-2.5% samples in the initial state: a - annealed for 12 hours at 580 °C, b - annealed for 6 hours at 580 °C; and after ECAP: c - single pass, d – 6 passes (SEM)*

Fractography analysis showed that all the samples were fracture by ductile fracture mechanism. The average size of dimples for samples in the initial state amounted 5.3 ± 0.5 µm (annealed for 12 hours at 580 °C) and 4.5 ± 0.5 µm (annealed for 6 hours at 580 °C) but the average size of dimples after ECAP were 2.8 ± 0.3 µm (single pass) and 2.6 ± 0.4 µm (6 passes).

4. Conclusion

Prolonged corrosion tests in Ringer's solution of the samples of zirconium alloy Zr-2.5%Nb in the initial state and after ECAP were performed for two years with a periodic sample weighting. According to the test results no significant gain or loss of the sample weight was revealed in the initial state and after ECAP.

Quantitative comparative values of crack resistance of the Zr-2.5%Nb alloy were measured after ECAP and annealed states (after 6 and 12 hours of annealing at 580 °C). The crack resistance of samples from zirconium alloy Zr-2.5% Nb in the initial state after annealing for 6 hours at 580 °C was in two times higher compared to the samples after ECAP in a single pass.

Metallographic and fractographic analysis showed that the main factor influencing on the crack resistance of zirconium alloy Zr-2.5%Nb after various modes of thermomechanical treatment is the presence of subgrain structure and recrystallized grain size before and after ECAP.

5. Literature

1. N. Stojilovic, E.T. Bender, R.D. Ramsier. Surface chemistry of zirconium // Progress in Surface Science.–2005.–V. 78.–P. 101–184.
2. V.A. Kukareko, V.I. Kopylov, A.G. Kononov, S.O. Rogachev, S.A. Nikulin and S.V. Dobatkin. Structural transformations during heating of a Zr-2.5% Nb alloy subjected to equal-channel angular pressing // Russian Metallurgy (Metally).–2010.–N 7.–P. 642-647.
3. Terent'ev V.F., Dobatkin S.V., Nikulin S.A., Kopylov V.I., Prosvirnin D.V., Rogachev S.O., Bannykh I. Fatigue strength of submicrocrystalline Ti and Zr-2.5%Nb alloy after equal channel angular pressing // Kovove Mater.–2011.–V. 49.–N 1.–P. 65-73.
4. Rogachev S., Nikulin S., Dobatkin S., Terent'ev V., Kopylov V. The structure and properties of ultrafine-grained zirconium alloys // International virtual journal "Machines, technologies, materials".–2011.–N 12.–P. 3-6.
5. S.A. Nikulin, S.O. Rogachev, A.B. Rozhnov, M.V. Gorshenkov, V.I. Kopylov, S.V. Dobatkin. Resistance of alloy Zr – 2.5% Nb with ultrafine-grain structure to stress corrosion cracking // Metal Science and Heat Treatment.–2012.–V. 54.–N 7-8.–P.407-413.

VIRTUAL LABORATORY OF ROBOTICS

Ing. Marcela Bucanyova, PhD[1]; Assoc. Prof. Ing. Peter Kostal, PhD.[2]; Ing. Andrea Mudrikova, PhD.[3]
Slovak University of Technology, Faculty of Material Sciences and Technology, Institute of Production Technology [1,2,3] – Trnava, Slovakia
E-mail: marcela.bucanyova@stuba.sk, peter.kostal@stuba.sk, andrea.mudrikova@stuba.sk

Abstract:

*In frame of the project **KEGA 027STU-4/2014** at our institute, we are building a virtual laboratory of robotics. The main objective is to build a laboratory together with a set of training modules in the field of automation and industrial robotics that will serve to teach the principles of automatic control of manipulation and programming of industrial robots, which are now increasingly implemented in production practice. Built laboratory will develop the knowledge and expertise of students in the field of automated and robotic systems, application of innovative educational program and methodology of using modern technologies, including CA and e-learning.*

KEYWORDS: VIRTUAL LABORATORY, ROBOTICS, TEACHING, PROFESSIONAL COMPETENCIES

1. INTRODUCTION

In these days globalization, social, political and economical situation create special environment in which only the best can survive.

Important requirement of potential employers is a right relationship between professional competences and key competences.

Key competences can be represented as universal complex skills which overreach level of specific professional knowledge and skills. Key competences are skills which inform how will particular person behave accordingly to the situation. While professional

competences are very important for high skilled work, key competences are helping to put better use of professional competences to practice.

- Professional competences ensure good managing of working tasks
- Key competences are widely usable skills such as decide ability, ability of solving problems, team working, communication in foreign language, ability to learn, information working ability, etc

The aim of whole project is creating a virtual laboratory of robotics which would be used to learn designing of creation of robotized workplaces and their simulation.

Creation of such laboratory will lead to the quality increase of teaching process of subjects belonging to our study branch such as manufacturing devices and systems (industrial robots, automation and mechanization, automate theory, and so on…). Students which will go through courses in these kind of laboratory will receive required professional skills and competences.

These competences and skills will strengthen their abilities which are very important for designing processes of such devices. The students will also learn the methodology of creating several types of systems, which will lead to increase of their value at the labour market.

2. VIRTUAL LABORATORY OF ROBOTICS

New created virtual laboratory of robotics will be used for teaching of robotized workstation design principles. Various manufacturing systems can be implemented based on robotized workstation.

In virtual laboratory, the students will create the virtual models of robotized manufacturing systems and they will also be able to simulate the function of such device (Fig. 1). Students will be able to create their own virtual robotized workstation systems as well as to test them. Based on this fact they will be able to verify the proper function of the system by using of the simulation. Students with help of such laboratory will be able to create projects from various kinds of subjects while operating on the robotized system.
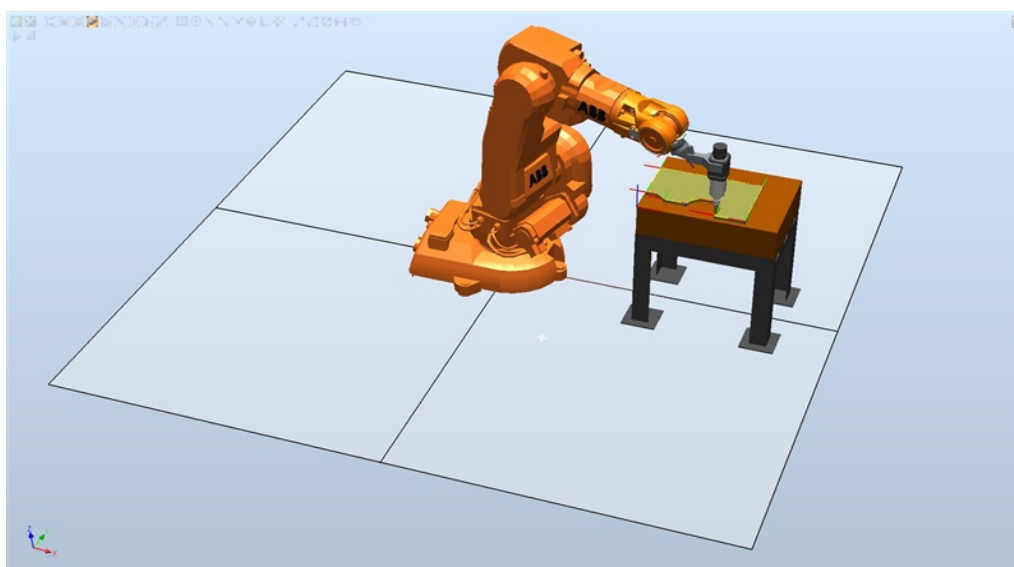
Fig. 1: Simulation of industrial robot working cycle

Virtual laboratory equipment will be composed of 10 PCs, each having a function of single workstation. Then network server will be installed in the laboratory, it's functions will be access to the internet and licensing of program on various PC devices. The environment of laboratory should include high quality data projector with silver screen and interactive board. All this equipment will contribute to the use of modern teaching methods.

Those tasks and exercises, which will be optimized and simulated in the virtual laboratory will be performed in real laboratory of industrial robots situated at our departments. (Fig. 2) That means

the real laboratory will increase the number of tasks and it's teaching effectiveness. The teaching process will be more effective and thanks to the virtual laboratory, there will be less mistakes and possible dangerous collisions between the robot and other devices. Such collisions could lead to the damage of devices installed in the laboratory. Based on fact that time consuming part of laboratory work will be concentrated only to the correct solutions, the students will have more time for realization of their examples.

Expected contribution of realization of this project can be seen in these steps:

- Education process enhancement
- Education process will be more attractive for the students
- Student will improve their technical knowledge and skills

- Before the real realization all practical tasks and examples will be simulated in virtual laboratory and only correct task wills be realized in real laboratory
- Costs reduction in real laboratory, because non correct tasks will not be realized
- More students can work in the same time
- Virtual laboratory will be accessible for the students through internet, which makes the use possible for external students,
- Work in the virtual laboratory will increase professional skills and competences of technicians
- The labour market's price of our graduate will grow

Fig. 2: *Industrial robot at our laboratory of robotics*

3. E-LEARNING AND VIRTUAL LABORATORY

Information and communication technologies present new dimensions in education at all levels. Education becomes the primary factor of national prosperity. New education technologies offer a wide space for further learning and life-long learning; remove barriers and ruin national frontiers, supporting at the same time advisability of learning with the main emphasis on utilization in practice and global way of thinking.

E-learning, as a new didactic method, facilitates distance learning and provides new possibilities for other education forms. Teachers become authors of educational, instructional documents with a specific mission – to transform the quality of all attendance forms of study into rationally configured documents in electronic form.

Computers and other facilities gave rise to world wide communication network – internet. In present time internet represents the most extensive and most massive information and communication technology that enables both general and addressed bidirectional communication.

If we are looking to the e-learning as to the effective using of information technologies in education process, we can say that we are talking about two new possibilities, which can be used in education process.

Classical teaching leaded by a teacher is realized from the beginning of history. This type of teaching in not possible to change, for some kinds of teaching. Educating only with help of a teacher has many disadvantages.

E-learning is created for improvement of these disadvantages and it is an optimal solution for complex education. To create interesting, address, individual and interactive education process which can be integrated in to the everyday life, we have to combine proper

methods of classical and e-learning education style. Also in areas in which is personal contact with teacher necessary, the students can be study before the class through electronic system. Then the students will be coming to the lectures with new amount of information and questions. After such process teacher is able to speak only about interesting or difficult fields of study. Also the time of lectures can be reduced.

A convenient combination of „classical" and electronic education (e-learning) creates new possibilities to implement ideas of the teacher and demands on students. This is a new look on university education method in which proficiency and experience of the teacher unite with advantages of information communication technologies. The result of their bilateral action consists not only in human activity improvement but makes the education process more interesting, effective and more addressed.

E-learning brings many communication ways such as emails, video conferences, which allows teacher to individual access to individual students. Following to the backward information about the lectures, teacher has exact information about the student. Information such as: how good were the students in single lectures, how many points did students reach in single fields of study or how much time does it take to understand for students. Thanks to the number of communication ways, the teacher is able to communicate with his students more intensively than before by typical classes.

Instead of constant repeating of the same information in the lectures, teacher will be able to work more intensively on preparation of new lectures or he can update lectures.

E-learning gives to the teacher new useful tools which can be used for simple and rapid transfer of his/her own knowledge and skills in to the form which will make these information more accessible for everyone who needs them.

E-learning is a solution designated for education process, but is

shows education in other context. E-learning is not restricted only for student education, but it is also a method of information passing and sharing. Such sharing and passing of information is important in field of whole life education process which is very important for technician. Classical information technologies and systems are dealing with information searching and searching in the exact time. E-learning gives emphasis on kind of information passing.

Today not only reaching of the information in exact time is important, but it is also very important to understand the information and give this information in wide coherences. And these accomplishments are coming with e-learning.

E-education as a new progressive way of education and it brings new possibilities. This education form can be used in all degrees of formal education and can be also used in whole life education process.

Content of e-lerning is showed at Fig. 3

Fig. 3: Content of e-learning

3.1. Asynchronous Education

Under the term „asynchronous education" we understand all tools and procedures without „face-to-face" communication between the teacher and the student that means without direct contact in any way. Asynchronous education involves e.g. individual courses, self-study of materials, preparation of specifications, participation in conference and e-mailing.

3.2. Synchronous Education

Under the term „synchronous education" we understand all methods including direct contact of the student with other students and the teacher, e.g. chat, audio/video conference, application sharing, common board.

For instance, students can be electronically „pre-trained" also for areas where the personal contact with the teacher is considered to be inevitable. Such students come then to the teacher with a lot of information and questions and the teacher can deal only with the interesting or difficult parts of education and to shorten so the training time significantly.

E-learning brings along a lot of communication tools starting with e-mails up to video-conferences enabling teachers to work with individual students. Based on feed-back the teacher is exactly informed about student´s progress in individual lessons, the place and number of points achieved and time spent in individual education fields. Thanks to many communication channels the cooperation with the student can be more intensive compared with the classical education lessons.

E-learning standards describe plenty of areas from hardware, via communication interface, up to didactics and meta-data. Standards are created by each organizer individually.

E-learning:

- Is aimed at the student´s needs,

- Takes full advantage of IKT: real time,
- Makes use of several education methods: a virtual classroom, simulations, interactive texts
- Includes also supporting administrative functions: tutoring, evaluation, testing, registration, payments, records

E-learning Structure for Distant Education:

- Basic information about the course (teacher, annotation, syllabus,...)
- Respective education materials (text, pictures, diagrams, graphs, animations, audio-video,..)
- Students´activation (tests, tasks, homeworks,...)
- Communication – synchronous (chat,...) and asynchronous (e-mail,...)
- Feed-back (delivery of solved tasks, questionnaires, inquiry,...)

3.3. Manuals and learning materials

Manuals will be created within the frame of this project and they will be accessible through the internet. Solved tasks will start with simple layouts and will end with more complex tasks. Every task will include detail device function description and standard connection scheme. These descriptions will serve as supplementary study literature for students of internal and also distant study form. Experiences gained by creating of such teaching system will be implemented into the distant study system by help of e-learning.

4. CONCLUSION

Researches of employers' requests and also researches of students' opinions about the university preparation are indicating that there is small connection between university education schedules and practice requirements. There is a number of competences, knowledges and skills which have to be learned by universities. Key competences are very important and integrating category, which influence to the quality student requirements. Such requirements are very important in the price of graduated on the labour marked. Most preferred employers' requirements are for example, solving problem's ability, determine ability, team working, team leading ability, etc.

Amongst the most important requirements influencing the future employees (technical engineers) belongs:

- Creativity
- Foreign language skills
- Independence
- Computer working skill
- Responsibility
- Flexibility
- Knowledge of actual trends in the branch
- Willingness of other education
- Communication

All these competences can be achieved by the students working in virtual and real laboratory of robotics.

Graduates of study gets the needed skills, experiences and they will have knowledges about a methodology of robotized manufacturing systems design. They can simulate the working of designed devices. For simulation realization will be installed specialized software at out intranet. By this software we can supervising every parts of designed manufacturing system. This system include only real industrial parts (PLC, stepper driver, servo driver, sensors and other...).

Systems and their functions which are thought in virtual laboratory can be found in real industrial environment. Knowledge and skills with those systems are highly reputable and are also demanded by wide number or employers, like huge international technical industries and concerns such as PSA, KIA, Volkswagen, and others.

In last phases of laboratory building we would like to create internet access to this laboratory, because we would like to allow work in laboratory also for students of distant forms. We would like to allow the access to laboratory not only during classes so student will be

able to fulfill their tasks not only in reserved time.

Knowledge acquired by process of creating of this kind of virtual laboratory will be also used in other projects and will be also used by creating of new modern kind of teaching process by e-learning.

5. ACKNOWLEDGEMENT

6. REFERENCES

[1]   C. Ume and M. Timmerman, "Mechatronics instruction in the Mechanical Engineering curriculum at Georgia Tech," *Mechatronics*, vol. 5, no. 7, pp. 723 – 741, 1995.

[2]   D. G. Alciatore and M. B. Histand, "Mechatronics at Colorado State University," *Mechatronics*, vol. 5, no. 7, pp. 799 – 810, 1995.

[3]   Danišová, Nina - Zvolenský, Radovan: Automated flexible manufacturing systems. In: KOD 2006 : Zbornik radova / nadát. Simpozijum sa medunarodnim učešćem. 4. Konstruisanje, oblikovanje i dizajn. Palic, 30-31. maj 2006. - Novi Sad : Fakultet tehničkih nauka, 2006. - ISBN 86-85211-92-1. - S. 253-256

[4] HOLUBEK, Radovan - DELGADO SOBRINO, Daynier Rolando - KOŠŤÁL, Peter - RUŽAROVSKÝ, Roman. Offline programming of an ABB robot using imported CAD models in the RobotStudio software environment. In *Applied Mechanics and Materials : Novel Trends in Production Devices and Systems II. Special topic volume with invited peer reviewed papers only*. Vol. 693 (2014), s. 62-67. ISSN 1660-9336.

[5]   *HOLUBEK, Radovan - HORVÁTH, Štefan - VELÍŠEK, Karol. Increased effective education pneumatic and electropneumatic at virtual laboratory. In Annals of DAAAM and Proceedings of DAAAM Symposium 2009 : Vol. 20, No. 1. s.0193-0194. ISSN 1726-9679.*

[6]   I. Matijevics, "Real and Remote Laboratories in Education," *Ann. Fac. Eng. Hunedoara – Int. J. Eng.*, vol. IX, no. 2, 2011.

[7]   J. E. Carryer, "The design of laboratory experiments and projects for mechatronics courses," *Mechatronics*, vol. 5, no. 7, pp. 787 – 797, 1995.

[8]   Košťál, Peter - Mudriková, Andrea - Velíšek, Karol: Virtual laboratory of pneumatic systems. In: Annals of DAAAM and Proceedings of DAAAM Symposium. - ISSN 1726-9679. - Vol. 18, No. 1. Annals of DAAAM for 2007 & Proceedings of the 18th International DAAAM Symposium "Intelligent Manufacturing & Automation: Focus on Creativity, Responsibility, and Ethics of Engineers" : Croatia, Zadar 24-27th October 2007. - Viedeň : DAAAM International Vienna, 2007, s. 389-390

[9]   M. Timmerman, "A hybrid approach for Mechatronics instruction at the University of Tulsa," *Mechatronics*, vol. 5, no. 7, pp. 833 – 843, 1995.

[10] Mudriková, A. (2006) Celoživotné vzdelávanie ako jedna z podmienok profesnej úspešnosti inžiniera – technika. *Proceedings of SCHOLA 2006*. 7. medzinárodná vedecká konferencia KIPP : Kvalita výchovy a vzdelávania. - Bratislava : STU v Bratislave, 2006. - ISBN 80-227-2389-4. - S. 274-279

[11] R. Skapinyecz and B. Illés, "Introduction Of The Virtual Logistics Laboratory Of The University Of Miskolc," *Adv. Logist. Syst.*, vol. 6, no. 1, pp. 111–116, 2012.

[12] RUŽAROVSKÝ, Roman - HOLUBEK, Radovan - KOŠŤÁL, Peter. Novel Trends in Manufacturing Systems with View on Implementation Possibilities of Intelligent Automation. In *World Academy of Science, Engineering and Technology*. Iss. 80 (2013), s.[5] p. ISSN 2010-376X.

[13] S. M. Castillo, E. Hormiga-Pérez, L. Coromina, and J. Valls, "Key competences in new ventures: A model for evaluating," *Ann. Fac. Eng. Hunedoara – Int. J. Eng.*, vol. VIII, no. 2, 2010.

[14] S. R. McNeill and J. D. Helm, "A required mechanical engineering course in microprocessors," *Mechatronics*, vol. 5, no. 7, pp. 763 – 774, 1995.

[15] Velíšek, K.; Košťál, P. & Javorová, A.(2005) Flexible assembly cell. *Proceding of 4th International conference ICAMaT 2005*, Editor: C. Doicin, pp.479-482, ISBN 973-27-1254-6, 3. - 4. november, 2005, Bucharest, Romania, The Publishing House of Romanian Academy

[16] W. K. Durfee, "Designing smart machines: Teaching mechatronics to mechanical engineers through a project-based, creative design course," *Mechatronics*, vol. 5, no. 7, pp. 775 – 785, 1995.